

Organisation and Disruption of the Outer  
Membrane of *Escherichia coli*

Georgina Domville Benn

Thesis submitted for the degree of

Doctor of Philosophy

at

University College London



*August 2021*

I, Georgina Domville Benn, confirm that the work presented in this thesis is my own. Where information has been derived from other sources, I confirm that this has been indicated in the thesis.

# Abstract

As disease-causing pathogens in the Enterobacteriaceae family, *E. coli* are part of the World Health Organisation's critical list of antibiotic resistant bacteria, for which new therapies are urgently required<sup>1</sup>. They are Gram-negative bacteria, so have a complex envelope with an inner and outer membrane, separated by a peptidoglycan-containing periplasm. In particular the outer membrane provides a formidable protection against antibiotics<sup>2</sup>. As well as being clinically relevant, *E. coli* are extensively studied model organisms. But, despite their key role in the clinic and in research, major parts of their cell cycle and organisation are not fully understood, including the supramolecular architecture of the cell envelope, how the outer membrane is constricted as it divides and how our immune system targets the surface.

In this thesis, atomic force microscopy is used to answer some of these questions by imaging the surface of live cells with nanometre resolution as they live, grow, divide, and die. The method is first optimised, to next allow the acquisition of data that reveals supramolecular organisations on the surface of dividing cells, answering questions on how the outer membrane is organised. A new potential role for a much-studied protein, OmpA, is also found, and evidence of phase separation in the outer membrane is revealed. Finally, the mechanism by which our immune system kills *E. coli* via the membrane attack complex is then studied, showing how complement-induced cell-death correlates with a mechanical destabilisation of the cell envelope.

# Impact Statement

The organisation and targeting of the *E. coli* cell envelope are insufficiently understood. The external layer of the envelope, the outer membrane, is particularly challenging to study, primarily due to its complexity, heterogeneity and nanometre scale. In this thesis, *E. coli* are investigated with nanometre resolution by atomic force microscopy (AFM). For this to be possible, sample preparation techniques were first developed. As well as being invaluable for this project, this information is highly transferable for other AFM experiments and so, the results were published for exploitation by other microscopists in the field.

The architecture of the outer membrane is important to understand, since antibiotics must act at or traverse this layer to be effective. This is particularly important as the efficacy of antibiotics against *E. coli* and related strains (other Gram-negative bacteria) are of key concern in the antibiotic resistance crisis that is already causing a substantial clinical burden worldwide.

Although the outer membrane provides a formidable barrier, it can also be the target of antimicrobials. For example, our immune system can perforate the outer membrane by the formation of the membrane attack complex (MAC), which leads to killing of *E. coli* and other Gram-negative bacteria. However, its mechanism of action is not fully understood. Bacterial sensitivity and resistance to MAC formation can define patient outcomes following bacterial infections. Investigating the mechanism of MAC lysis may inform future work to explain resistance mechanisms and find new ways of targeting cells.

The research in this thesis has led to the publication of 3 publications in international journals, with a further 2 in preparation.

# Acknowledgements

I would like to thank my supervisor, Prof Bart Hoogenboom, for giving me this opportunity and providing inspiration, support and guidance throughout the project. Thank you, also, to my industrial supervisor, Dr Maxim Ryadnov of the National Physical laboratory, for his advice and input over the course of my PhD. I am extremely grateful for the time and assistance of Dr Isabel Llorente-Garcia, Dr Brian Ho and Dr Emmanuel Boucrot as members of my thesis committee.

All the Hoogenboom lab, past and present, have been amazing to work with and I am grateful to them all. In particular, I have many thanks for Dr Alice Pyne and Dr Ed Parsons who taught me so much about AFM and gave me more generous support, friendship and advice than I could have wished for. Dr Richard Thorogate's support in all times of technical crises has been vital and this would have been impossible without his help. For their friendship, encouragement and insightful advice, I would especially like to thank Guillermo, Kate and Bernice; I could not have done this without them.

Thanks to all of our collaborators for their enthusiasm, advice and generosity throughout the project. Dr Suzan Rooijackers and Dennis Doorduijn of UMC Utrecht, thank you for your expertise and informative discussion on the MAC. I would also like to acknowledge Prof Tom Silhavy and Dr Irina Mikheyeva of Princeton University, and Prof Colin Kleanthous and Patrick Inns of the University of Oxford for an enjoyable and interesting collaboration on the outer membrane.

Anna, Krysia, Carolina and Zoë, thank you so much for your unbelievable support and friendship. Joel, thank you for your help with all my many physics questions and for being a great friend. Wilf thank you for your coding help, it was essential!

Finally, for always believing in and supporting me, I would like to thank my fabulous parents. And I would like to thank my sister, who knows how profoundly grateful I am for everything.

# List of Publications

1. Benn, G., Pyne, A. L. B., Ryadnov, M. G. & Hoogenboom, B. W. Imaging live bacteria at the nanoscale: comparison of immobilisation strategies. *Analyst* 1–15 (2019). doi:10.1039/c9an01185d
2. Doorduyn, D. J., Bardoel, B. W., Heesterbeek, D. A. C., Ruyken, M., Benn, G., Parsons, E. S., Hoogenboom, B. W. & Suzan, S. H. Bacterial killing by complement requires direct anchoring of membrane attack complex precursor C5b-7. *PLoS Pathog.* 16, (2020).
3. Hammond, K.\*, Benn, G.\*, Bennett, I., Parsons, E. S., Ryadnov, M. G., Hoogenboom, B. W. & Pyne, A. L. B. in *Polypept. Mater. Methods Mol. Biol. vol 2208* (ed. Ryadnov, M. G.) 225–235 (Humana Press, 2020).
4. Benn, G., Mikheyeva, I. V, Inns, P. G., Forster, J. C., Ojkic, N., Bortolini, C., Ryadnov, M. G., Kleanthous, C., Silhavy, T. J. & Hoogenboom, B. W. Phase separation in the outer membrane of Escherichia coli. *Proc. Natl. Acad. Sci.* 118, e2112237118 (2021).
5. Benn, G, *et al.* Nanoscale visualisation of bacterial killing by the membrane attack complex. *In preparation.*

\* co-first authors, equal contribution.

# Contents

Abstract.....	3
Impact Statement.....	4
Acknowledgements.....	5
List of Publications.....	6
List of Abbreviations.....	9
List of Figures.....	10
Chapter 1.....	12
1.1    Gram-Negative Bacteria .....	12
1.1.1    Cellular Organisation.....	13
1.1.2    The <i>E. coli</i> Outer Membrane .....	14
1.1.3    Targeting the Outer Membrane.....	20
1.2    Atomic Force Microscopy .....	26
1.3    Scope of Thesis .....	29
Chapter 2.....	30
2.1    Sample Preparation .....	30
2.1.1    Bacterial Strains and Conditions .....	30
2.1.2    Substrate Preparation .....	32
2.1.3    Sample Deposition .....	33
2.1.4    Protein, Antimicrobial Peptide and Label Addition .....	34
2.2    Atomic Force Microscopy .....	36
2.2.1    Force Spectroscopy Imaging .....	37
2.2.2    Tapping Mode .....	39
2.2.3    Calibration .....	43
2.2.4    Combined Brightfield and Fluorescence Microscopy .....	45
2.3    Data Analysis .....	46
2.3.1    Optical Images.....	46
2.3.2    AFM Processing.....	47
2.3.3    Further Image Analysis.....	48
2.3.4    AFM Force Curve Analysis.....	50
2.3.5    Statistics and Graphing .....	51
2.4    Concluding Remarks .....	51
Chapter 3.....	53
3.1    Introduction.....	53
3.2    Results .....	54
3.2.1    Experimental Set-up.....	54

3.2.2	Cell Death is High in mQ and Gelatin is Ineffective .....	56
3.2.3	PLL is Effective for BL21 E. coli .....	56
3.2.4	Cell-Tak™ Led to Aggregates on Bacteria .....	57
3.2.5	Vectabond® Provides Excellent Adhesion .....	58
3.3	Discussion .....	59
Chapter 4	.....	61
4.1	Introduction.....	61
4.2	Results .....	62
4.2.1	Imaging Whole Cells at Nanometre Resolution.....	62
4.2.2	<i>E. coli</i> Cells are Covered in a Network of Trimeric Porins.....	64
4.2.3	Trimeric Porins are Close to Stationary .....	65
4.2.4	OmpA is Distributed Within the Network.....	67
4.2.5	Removing <i>ompA</i> Perturbs the Trimeric Porin Network.....	68
4.2.6	Removal of <i>ompA</i> Increases Trimer Diffusion .....	70
4.3	Discussion .....	71
Chapter 5	.....	74
5.1	Introduction.....	74
5.2	Results .....	75
5.2.1	Smooth Patches Disrupt the Porin Network.....	75
5.2.2	Patches and Pore Networks Behave as Liquid Phases.....	76
5.2.3	Patches are Depleted of Abundant OMPs .....	77
5.2.4	Patches are LPS-Enriched Islands.....	81
5.2.5	Phospholipids Phase-Separate into New Structures .....	82
5.2.6	The Outer Membrane Ruffles at the Division Site.....	85
5.3	Discussion .....	87
Chapter 6	.....	90
6.1	Introduction.....	90
6.2	Results .....	92
6.2.1	The MAC Can Be Visualised by AFM .....	92
6.2.2	The Pattern of MAC Insertion is Highly Varied .....	92
6.2.3	The Mechanism of Lysis by MAC .....	96
6.3	Discussion .....	100
Chapter 7	.....	103
Bibliography	.....	104

# List of Abbreviations

<b>AFM</b>	Atomic force microscopy
<b>AMP</b>	Antimicrobial peptide
<b>APTES</b>	3-Aminopropyltriethoxysilane
<b>Ara</b>	Arabinose
<b><i>B. subtilis</i></b>	<i>Bacillus subtilis</i>
<b>BAM</b>	$\beta$ -barrel assembly machinery
<b>BSA</b>	Bovine serum albumin
<b>Cryo-EM</b>	Cryo-electron microscopy
<b><i>E. coli</i></b>	<i>Escherichia coli</i>
<b>EDTA</b>	Ethylenediaminetetraacetic acid
<b>EM</b>	Electron microscopy
<b>FRAP</b>	Fluorescence recovery after photobleaching
<b>Fuc</b>	Fucose
<b>GN</b>	Gram-negative
<b>HEPES</b>	4-(2-hydroxyethyl)-1-piperazineethanesulfonic acid
<b>IM</b>	Inner membrane
<b><i>L. lactis</i></b>	<i>Lactococcus lactis</i>
<b>LB</b>	Luria-Bertani broth
<b>LPS</b>	Lipopolysaccharide
<b>Lpt toxin</b>	Long type I toxin
<b><i>M. Smegmatis</i></b>	<i>Mycobacteria smegmatis</i>
<b>MAC</b>	Membrane Attack Complex
<b>Mla pathway</b>	Maintenance of Lipid Asymmetry pathway
<b>MM</b>	1X M9 salts, 2 mM MgSO <sub>4</sub> , 0.1 mM CaCl <sub>2</sub> , 0.36% glucose
<b>MM 0.4%</b>	1X M9 salts, 2 mM MgSO <sub>4</sub> , 0.1 mM CaCl <sub>2</sub> , 0.4% glucose
<b>mQ</b>	milliQ
<b>OM</b>	Outer membrane
<b>OMP</b>	Outer membrane protein
<b>PAMP</b>	Pathogen-associated molecular pattern
<b>PB</b>	10 mM phosphate buffer, pH 7.4
<b>PBS</b>	10 mM phosphate buffer, 137 mM NaCl, 2.7 mM KCl, pH 7.4
<b>PL</b>	Phospholipid
<b>PLL</b>	Poly-L-Lysine
<b>PPI</b>	Protein-protein interactions
<b><i>R. denitrificans</i></b>	<i>Roseobacter denitrificans</i>
<b>RMS</b>	Root mean square deviation
<b><i>S. aureus</i></b>	<i>Staphylococcus aureus</i>
<b>Sec translocon</b>	Secretory translocon
<b>SPT</b>	Single particle tracking
<b>TEM</b>	Transmission electron microscopy
<b>WT</b>	Wild type
<b><i>V. cholerae</i></b>	<i>Vibrio cholerae</i>

# List of Figures and Table

Figure 1.1: Gram-negative bacterial membranes.....	13
Figure 1.2: Schematic of LPS synthesis.....	16
Figure 1.3: Previous research into outer membrane protein organisation.....	18
Figure 1.4: Previously proposed outer membrane organisation.....	19
Figure 1.5: Membrane attack complex assembly and structure.....	24
Figure 1.6: Previous atomic force microscopy of bacterial cells.....	27
Figure 2.1: Schematic of sample preparation.....	32
Figure 2.2: General set-up for atomic force microscopy in liquid.....	36
Figure 2.3: Principles of force spectroscopy imaging.....	37
Figure 2.4: Principles of tapping mode.....	39
Figure 2.5: The effect of tip-sample interactions on a frequency sweep due to damping and effective stiffening.....	41
Figure 2.6: A frequency sweep shows the ‘forest of peaks’ generated when using piezo-actuated tapping mode in liquid.....	43
Figure 2.7: The thermal tune and contact-based calibrations methods.....	45
Figure 2.8: Determining the diffusion constant from mean squared displacement..	49
Figure 3.1: Adhesion of BL21 in milliQ water and survival of both strains in all conditions.....	55
Figure 3.2: Adhesion of BL21 and MG1655 to gelatin.....	56
Figure 3.3: Adhesion of BL21 and MG1655 to PLL.....	57
Figure 3.4: Adhesion of BL21 and MG1655 to Cell-Tak™.....	58
Figure 3.5: Adhesion of BL21 and MG1655 to Vectabond®.....	59
Figure 4.1: <i>E. coli</i> are imaged at nanometre resolution by atomic force microscopy.....	63
Figure 4.2: Characterisation of pore network as trimeric porins.....	65
Figure 4.3: Diffusion of pores in the membrane is slow.....	66
Figure 4.4: Streptavidin labelling of OmpA.....	67
Figure 4.5: Effect of <i>ompA</i> deletion on porin network.....	68
Figure 4.6: Pores are present in the $\Delta ompA$ outer membrane, but they are harder to image.....	69
Figure 4.7: Colicin N <sup>1-185</sup> mCherry labelling of OmpF trimers.....	71
Figure 4.8: OmpF diffusion may be higher in $\Delta ompA$ cells.....	72
Figure 5.1: Distinct pore-free patches can be seen within the trimeric porin network.....	76
Figure 5.2: Patches behave as phase separated regions of the membrane.....	77
Figure 5.3: Colicin N <sup>1-185</sup> mCherry and streptavidin labelling of OmpF and OmpA show the patches are depleted of proteins.....	78
Figure 5.4: The porin network is not required for patches to form.....	79
Figure 5.5: Patch size depends on LPS levels.....	80
Figure 5.6: Patches are LPS-enriched domains.....	82
Figure 5.7: Efficiency of plating assays show sensitivity to SDS-EDTA and bacitracin is high in $\Delta mlaA \Delta pldA$ cells.....	82
Figure 5.8: Effect of outer-leaflet phospholipids on domain formation.....	83

Figure 5.9: LPS-enriched and phospholipid-like patches are distinct features.....	84
Figure 5.10: Force spectroscopy imaging finds no difference between patch and network stiffness.....	85
Figure 5.11: Cells can be imaged for long time periods to track division.....	86
Figure 5.12: The division site often becomes highly ruffled.....	87
Figure 6.1: The MAC may be imaged by AFM on the surface of whole bacteria.....	93
Figure 6.2: MAC distribution was highly variable on different cells.....	93
Figure 6.3: MAC are distributed evenly over the surface of a single cell and appeared to cluster or branch.....	95
Figure 6.4: MAC do not form clusters in the membrane.....	96
Figure 6.5: MAC do not form branches.....	96
Figure 6.6: Bacteria can resist MAC killing for long time periods.....	97
Figure 6.7: Bacteria lysed by the MAC have unstable membranes.....	98
Figure 6.8: MAC induced outer membrane destabilisation appears temporally correlated with inner membrane permeabilization.....	98
Figure 6.9: Outer membrane destabilisation occurs simultaneously with inner membrane permeabilization.....	99
Figure 6.10: Melittin induced cell death does not destabilise the outer membrane.....	100
Table 2.1: Strains and plasmids.....	31

# Chapter 1

## Introduction

### 1.1 Gram-Negative Bacteria

Since the 1940s, a plentiful supply of cheap antibiotics has reduced deaths from infectious disease by 70% and paved the way for medical breakthroughs such as transplants and chemotherapy<sup>3,4</sup>. But their widespread use in medicine and agriculture has led to extensive, global resistance. Since no new antibiotic classes have been found since the 1980s, we are faced with an incoming catastrophe for human health. Without intervention, we could face millions of deaths a year from antibiotic resistant bacteria in a few decades<sup>5</sup>.

The World Health Organisation's list of species with critical levels of resistance, the ESKAPE pathogens (*Enterococcus faecium*, *Staphylococcus aureus*, *Klebsiella pneumoniae*, *Acinetobacter baumannii*, *Pseudomonas aeruginosa* and *Enterobacter* spp.), consists almost entirely of Gram-negative bacteria (GNs), therefore these are of particular concern<sup>1</sup>. GNs present a significant burden to healthcare worldwide and resistance to even last-resort antibiotics is rising globally<sup>1,6</sup>. It is also especially difficult to find new antibiotics against GNs due to the organisation of their cell membranes, reducing their appeal as targets for pharmaceutical companies<sup>7</sup>.

One of the main hurdles for antibiotic discovery is the cost of development. Almost half of this cost relates to the pre-clinical stage, partly due to a very high drop-out rate<sup>3</sup>. To improve the success rate of drug candidates in pre-clinical trials and reduce antibiotic susceptibility to resistance mechanisms, a better understanding of cell penetration is required. This can be achieved by comparing mechanisms of killing used in nature or by studying basic microbiology to understand the structures preventing entry into the cell<sup>7</sup>.

### 1.1.1 Cellular Organisation

To survive, all bacteria must protect themselves from conditions that would be fatal to a cell with a bare membrane. *E. coli* are GN bacteria, which protect themselves with a composite cell envelope. From the inside out, this cell envelope is composed of an inner membrane (IM) that surrounds the cytoplasm, then the periplasm that contains a cell wall and, finally, the outer membrane (OM; Fig. 1.1)<sup>2</sup>.

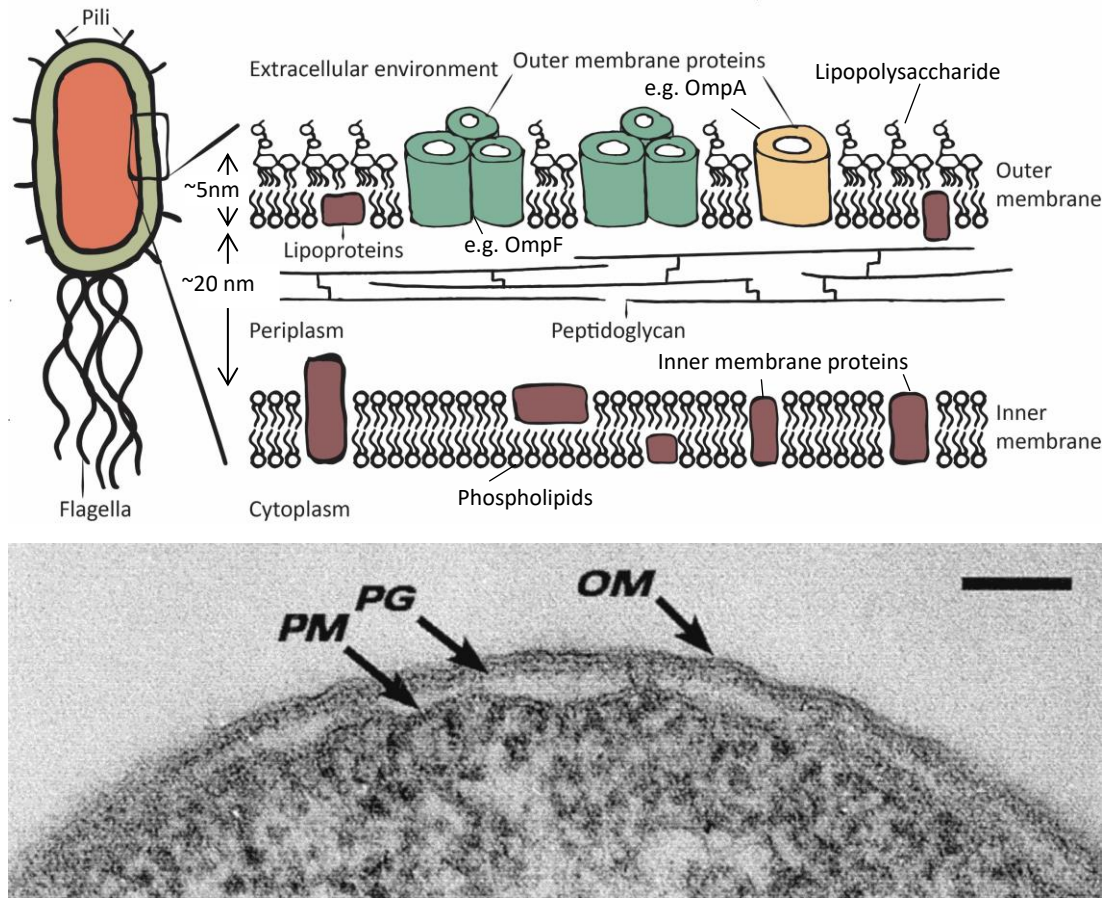


Figure 1.1. (A) GN bacterial cells have an inner membrane surrounding the cytoplasm, a periplasm that contains the cell wall (peptidoglycan) and an outer membrane. They can also have flagella, used for motility, and pili for sensing. The IM is a phospholipid bilayer and the OM is an asymmetric bilayer with a high protein content<sup>2</sup>. (B) Transmission electron microscopy image of an *E. coli* cell envelope from reference 8 shows the layers of membrane peptidoglycan. PM is inner membrane, PG is peptidoglycan and OM is outer membrane. Scale bar is 100 nm.

### 1.1.2 The *E. coli* Outer Membrane

The OM is a formidable barrier to external toxins and to many antibiotics, but allows small molecules to diffuse across freely. It achieves this feat with a unique composition of phospholipids (PLs), lipopolysaccharide (LPS) and proteins<sup>9,10</sup>.

The organisation of these components in the OM is striking in two ways: first, they are arranged as an asymmetric bilayer and second, the OM has a very high protein content (Fig. 1.1). This architecture is made and maintained by many, often redundant pathways that emphasise the importance of the organelle for cellular survival, where it is noteworthy that the OM has no direct access to cellular sources of energy<sup>2,9</sup>.

#### The inner leaflet

The OM is a bilayer, although not a classical PL one. The inner leaflet is made up of PLs, whereas the outer leaflet contains almost none. This was shown when it was observed that only half the mass of the OM is taken up by PLs, followed by the finding that PL labels did not bind intact cells- showing all PLs must be hidden in the inner leaflet. This has since been shown on various GN bacteria to varying degrees, with *E. coli* OM being highly asymmetric<sup>10,11</sup>.

PLs are synthesised on the IM. For many years, it has been controversial how they are translocated from the IM to the OM. In the 1970s, it was proposed that PLs flowed from the inner to outer membrane via fused regions, as lipids were shown to diffuse bidirectionally between the two membranes<sup>12</sup>. Subsequent electron microscopy (EM) found no evidence of membrane fusion and the hypothesis seemed unlikely. However, recent evidence has resurrected the theory. When PLs are pushed into the outer leaflet (via mutation of a key protein) and subsequently blebbed off, there is significant PL movement from the inner to outer membranes. It was also found that PL flow was reversible, concentration dependent and energy independent. The authors therefore suggested transient sites of protein mediated “hemifusion” between the OM inner leaflet and IM outer leaflet, which would explain both the observed PL flow and why no distinct connections of the inner and outer membranes have been seen by EM<sup>13,14</sup>.

The inner leaflet also has abundant lipoproteins. All lipoproteins are transported across the IM via the Sec translocon, then processed and attached to a lipid via an N-terminal cysteine at the IM outer leaflet. Those destined for the OM are transported across the periplasm via the Lipoprotein pathway to the OM inner leaflet where most lipoproteins remain, some at very high densities<sup>2,15</sup>. The most common lipoprotein is Lpp, present at  $\sim 10^6$  copies per cell, making it the most numerous protein in *E. coli*. It covalently anchors the OM to the cell wall in the periplasm, contributes to cell stiffness and its loss compromises membrane integrity<sup>16</sup>.

### The outer leaflet

While the inner leaflet is abundant in PLs, the outer leaflet contains very few. PLs are excluded from the outer leaflet by two main mechanisms: removal by the Mla pathway or breakdown by PldA<sup>17</sup>. The first component of the mla pathway, MlaA, is a ring shaped lipoprotein that allows PLs to diffuse into its lumen from the outer leaflet and towards the periplasm, where the PLs are handed over to periplasmic MlaC and brought to the IM for an unknown fate<sup>18,19</sup>. The mechanism of lipid homeostasis by the phospholipase, PldA, is somewhat clearer, as PLs are directly broken down to fatty acids and transferred to the cytoplasm, where they are recycled and stimulate LPS production<sup>20</sup>.

LPS is the main constituent of the OM outer leaflet. This large molecule consists of three regions: lipid A, a core polysaccharide, and the O-antigen. Lipid A is synthesised via the Raetz pathway, where the first committed reaction is catalysed by LpxC and followed by several enzyme-dependent additions to form a lipid A core. This pathway is shown in more detail in Figure 1.2<sup>21</sup>. Attached to the core is the O-antigen: a polysaccharide of variable lengths. In *E. coli* K-12 strains, the O-antigen is O16 and synthesised by the sequential translocation of sugars to the core LPS in the IM. But, this process is dependent on the WbbL protein, which is absent in most lab strains, so the LPS O-antigen is very short<sup>22</sup>.

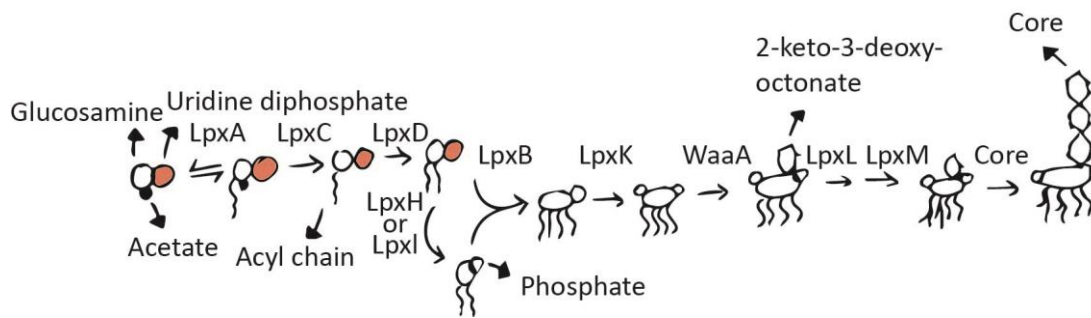


Figure 1.2. Schematic of LPS synthesis by the lipid A core. Synthesis takes place on the inner leaflet of the inner membrane. Figure adapted from reference 21.

Once the LPS is fully synthesised, it must be transferred to the OM. It is not trivial to transport the large, amphipathic molecules across the periplasm to the energy-less OM, at a rate sufficient to maintain cell growth. The process is performed by the LPS transfer (Lpt) pathway. Seven essential Lpt proteins, at various copy numbers, form a bridge between the IM, periplasm and OM so that, once LPS binds at the IM inner leaflet, it is not released until it reaches the outer membrane complex, LptDE. Here it enters the lumen of the LptD  $\beta$ -barrel and likely crosses into the OM outer leaflet via the crenelated top of the barrel<sup>23</sup>.

Interestingly, the only energy to perform the translocation of these large molecules, against a steep concentration gradient, is generated by the hydrolysis of ATP by LptB at the IM inner leaflet. To get LPS into the OM outer leaflet, the energy is thought to be transferred via a PEZ model. Here, the Lpt bridge is saturated by LPS, with every binding site occupied, so that the pushing of another LPS into the system at the bottom, forces an LPS out at the top<sup>23</sup>. Once in the outer leaflet, LPS are bound together by  $\text{Ca}^{2+}$  and  $\text{Mg}^{2+}$  in the polysaccharide core, which strongly bridges their negatively charged phosphate groups. Additionally, when the O-antigen is present, the long hydrophilic chains allow strong, ordered LPS-LPS interactions that provide a robust barrier to hydrophobic molecules<sup>2,24</sup>.

### Outer membrane proteins

Despite the tight barrier provided by LPS, the OM dynamically interacts with the extracellular environment and small hydrophilic molecules may pass freely via outer membrane proteins (OMPs). These are abundant transmembrane proteins making up ~3% of the *E. coli* genome; they have a wide range of functions, an inherent

redundancy and can be present at a range of copy numbers from 100s to ~100,000 per cell<sup>25–28</sup>. The most common types of OMPs are porins which allow molecules up to 600 Da, particularly water and ions, to passively diffuse across the outer membrane, while excluding large or lipophilic molecules. In *E. coli*, the most common porins are the trimeric OmpF and OmpC<sup>2,28,29</sup>.

With few exceptions, all OMPs have an antiparallel  $\beta$ -barrel structure with an even number of strands and all are inserted via the  $\beta$ -barrel assembly machinery (BAM) complex. BAM consists of five proteins: the essential OMP, BamA, and lipoproteins BamB-E. The exact role of each accessory protein is not well characterised and neither is the mechanism of insertion. However, it is thought that OMPs are inserted either by templating the target OMP  $\beta$ -strands to a metastable lateral gate in the BamA  $\beta$ -barrel, or by thinning the surrounding membrane, thus lowering the energy barrier for insertion, or a combination of the two<sup>30,31</sup>.

#### Outer leaflet organisation

Once inserted, OMPs are extremely static over long distances. Fluorescence recovery after photobleaching (FRAP) consistently shows that OMPs have significantly slower motility than IM proteins. In fact, single molecule fluorescence has shown that OMPs are sufficiently corralled that, when bound to OMPs, IM protein mobility is also reduced<sup>25</sup>. On a more local scale, OMPs have restricted diffusions varying from  $10^{-5}$ - $10^1 \mu\text{m}^2 \text{s}^{-1}$ , depending on the protein and technique<sup>32–39</sup>. Individual LPS molecules have also been shown to exhibit very limited diffusion, presumably due to tight LPS-LPS binding<sup>40</sup>.

The reason for OMP immobility is thought to be promiscuous protein-protein interactions (PPIs) that lead to non-homogenous patterning of OMPs across the cell<sup>32</sup>. When investigating the distribution of specific OMPs and LPS, several arrangements have been reported including bipolar segregation, helices, rings, or more commonly, islands<sup>32,40–43</sup>.

Several OMPs have been found to form heterogenous islands in the membrane. The monomeric BtuB and Cir proteins form ~500 nm clusters that initially appear at the midcell and contain BamA<sup>38</sup>. The trimeric porin, LamB, has also been shown to insert

into islands<sup>44</sup>. Specific investigations of BamA have found the formation of ~150 nm islands containing ~10 BamA proteins and, presumably, a heterogeneous mixture of other proteins<sup>27,45</sup>. Islands have also been shown to move toward the poles, potentially explaining how OMP turnover is achieved. If new OMPs are inserted only at midcell, old OMPs will be pushed toward the poles and, after only two divisions, new daughter cells will have an entirely new population of OMPs (Figure 1.3A)<sup>32,38</sup>. Although this neatly explains the turnover of most OMPs, it does not explain how proteins localised to poles, or even those that move inwards, are maintained<sup>30,32</sup>.

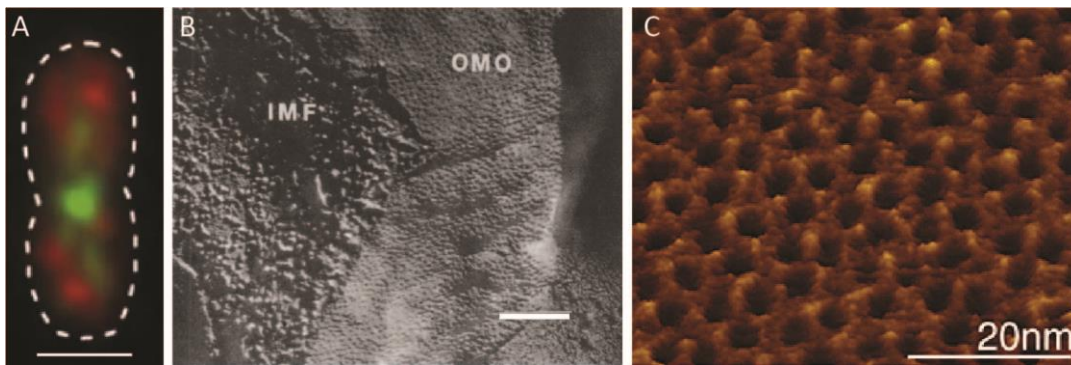


*Figure 1.3. (A) Live cells can be imaged at low resolution by fluorescence microscopy. Differential labelling of old (red) and new (green) OMPs, showing that OMPs are formed in distinct islands that move toward the poles. From reference 38. Scale bar is 1  $\mu$ m. (B) Dead cells may be imaged at high resolution by electron microscopy. Freeze-fracture EM of *E. coli*, shows the outer membrane packed with an imperfect lattice of particles. IMF = inner membrane outer face and OMO = outer membrane outer face. From reference 46. Scale bar is 100 nm. (C) Purified outer membranes may be imaged at high resolution by atomic force microscopy. Image of the inner face of an isolated GN OM shows the surface packed with trimers of porins. From reference 47.*

Although there is some variation, OMP labelling experiments indicate that promiscuous PPIs lead to the formation of distinct islands in the OM (Figure 1.3A). This theory is supported by protein folding experiments, which suggest that a membrane with protein rich islands will allow folding to occur efficiently in the remaining protein poor regions (Figure 1.4)<sup>30</sup>.

However, this appears to contradict freeze-fracture scanning electron microscopy data from the 1970s and 80s. This technique uses bacteria that have been rapidly

frozen, split and coated, allowing the visualisation of nanometre structures at fracture planes<sup>48</sup>. The inner surface of the OM of *E. coli* was found to be covered in ~7.5 nm pits and the outside covered in corresponding particles. These were assumed to be due to proteins (Figure 1.3B)<sup>46,49–51</sup>. Smooth pit- and particle-free regions were also seen on both the inner and outer membranes, the size of which varied depending on growth stage and chemical treatment, but they were always in the minority compared to particles<sup>46,49–51</sup>. At first sight, this apparent abundance of proteins covering most of the membrane is contradictory to the formation of highly heterogeneous OMP islands that are separate from the rest of the membrane.

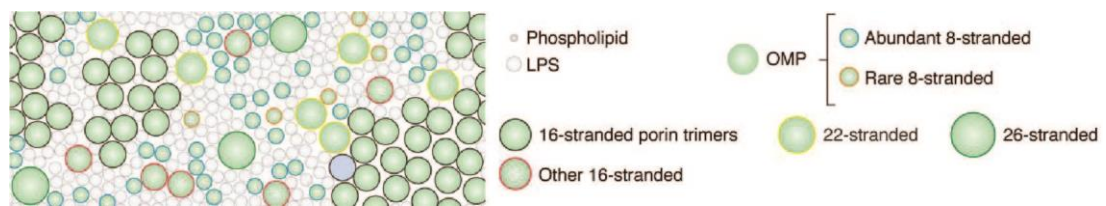


*Figure 1.4. A representation of proposed outer leaflet organisation that would explain current evidence and allow efficient protein folding in low-density regions. From reference 30.*

Furthermore, transmission electron microscopy (TEM) of purified outer membranes from *E. coli* confirm a dense packing of the abundant OmpF in a hexagonal lattice with a periodicity of ~7.5 nm<sup>9</sup>. OM fragments isolated from bacteria and imaged by atomic force microscopy (AFM) also found ~70% of the OM of *R. denitrificans* was packed with trimeric porins (Figure 1.3C)<sup>47</sup>. Similar arrangements have also been found by AFM on small regions of live GN bacteria<sup>37,52–54</sup>.

The apparent contradiction between conclusions from labelled and unlabelled experiments highlights the difficulty in determining OM organisation. The total OM area is small, such that any intramembrane organisation is likely to be at the resolution limit of even super resolution fluorescence microscopy. Furthermore, the enormous diversity of OMPs makes the labelling any of a significant proportion of proteins highly problematic. Nevertheless, the organisation of the OM is vital to our understanding of how antibiotics enter the cell and may provide a rich source of new targets<sup>55</sup>.

### 1.1.3 Targeting the Outer Membrane

It is well established that we urgently need new antibiotics to target GN bacteria. However, most small-molecule screens fail to find potential candidates due to the intrinsic inability of molecules in screening collections to cross the OM<sup>7,56</sup>. Even if a molecule is found, once in the cell, drugs must overcome extensive removal by efflux pumps<sup>10</sup>.

An obvious way to avoid the problem of entry and efflux is to target the OM itself. In nature, antimicrobial peptides and the complement system achieve this task and there have been significant recent breakthroughs for drug candidates targeting the OM.

#### OMP targeting antibiotics

Two essential OMPs are LptD, for LPS insertion, and BamA, for OMP insertion. Some attempts to target LptD have been made and a promising candidate, murepavidin, showed good efficacy but was withdrawn from phase III trials due to nephrotoxicity<sup>55,57</sup>. Yet structural insights into the LptD mechanism of action has found two essential cysteine residues in the  $\beta$ -barrel that may prove successful targets<sup>55</sup>.

Targeting of BamA has been more successful. Darobactin, a large, naturally occurring drug that is too large to pass through porins, has proved effective at killing GN bacteria by stabilising the closed lateral gate of BamA, preventing OMP folding<sup>58</sup>. Similarly, a chimeric peptide derived from natural scaffolds permeabilises the OM; and a small-molecule inhibits OMP biogenesis, both via BamA binding<sup>6,59</sup>. Finally, nitazoxanide reduces virulence by targeting Bam folding of specific OMPs, reflecting a shift in drug design to narrow spectrum agents<sup>55,56</sup>.

#### Membrane-disrupting antimicrobial peptides

Conversely, a promising source of broad-spectrum antibiotics is that of membrane targeting antimicrobial peptides (AMPs). Discovered in the 1980s in animals and insects, AMPs have been extensively studied and designed as therapies for bacterial infections. New and existing structures have been investigated using functional

studies of naturally occurring peptides, antimicrobial fragments of proteins and *de novo* design<sup>60</sup>.

Generally, AMPs are positively charged, such that they are attracted to negatively charged bacterial membranes<sup>61</sup>. They tend to have cationic and hydrophobic regions that are unstructured in solution, becoming amphipathic in a membrane. AMPs can be predominantly  $\alpha$ -helical ( $\alpha$ -AMPs) or contain  $\beta$ -hairpins ( $\beta$ -AMPs).  $\alpha$ -AMPs, like melittin from bee venom<sup>62</sup>, are the more extensively studied class of peptide. The less characterised  $\beta$ -AMPs mainly consist of  $\beta$ -hairpins, often stabilised by conserved disulphide bridges<sup>60</sup>.

Some AMPs act via disruption of DNA, protein or cell wall synthesis; interference with enzymes; or induction of protein misfolding<sup>60</sup>. But they mostly act directly on the membrane, causing extensive permeabilization. Traditionally, the most common mechanisms proposed for AMP action on membranes are the toroidal pore and the carpet model. In the toroidal pore model, peptides are arranged in a loose pore with lipid headgroups in between each monomer; molecular dynamics studies suggest that the peptides in the pore are highly disordered<sup>60</sup>, consistent with lack of clear structure in AFM experiments<sup>63</sup>. The carpet model is a more general description of AMPs covering a lipid bilayer by lying parallel to the surface<sup>64</sup>. However, simple mechanisms do not always reflect the complexity of AMP action. For example, melittin was found to kill *E. coli* via 7 sequential membrane events including outer membrane permeabilization, inner membrane permeabilization and membrane resealing<sup>62</sup>. The complexity of AMP action shows the need for extensive characterisation of how the OM can be lethally targeted.

The use of AMPs is particularly promising as their lack of specificity allows a breadth of activity leading to low resistance. However, the same properties often lead to high toxicity by permeabilization of host cells<sup>61</sup>. This vital problem is one that has not been overcome. By contrast, our immune system has extensive mechanisms for specific lysis of GN bacteria, in particular via the membrane attack complex.

### The innate immune system

The human immune system can be divided into two parts, adaptive and innate. The adaptive immune system provides a highly specific response to pathogens that is remembered for subsequent infections<sup>65</sup>. However, its mechanism of activating and cloning specific immune cells is slow, allowing rapidly dividing bacteria time to proliferate and cause disease<sup>66</sup>. Therefore, the innate immune system is required to provide the fast, generic response that contains disease in the first few days of infection<sup>66</sup>.

Innate immunity consists, broadly, of physical barriers, phagocytic cells and the complement system. If bacteria bypass the physical barriers, they can be targeted by phagocytes or the complement system. Both of these mechanisms require the recognition of common molecules generated by and on the surface of pathogens. Pathogen-associated molecular patterns (PAMPs) are molecules found predominantly or exclusively in microorganisms, which are recognised by pattern recognition receptors. PAMPs can be soluble or membrane-bound<sup>67</sup>, for example, LPS<sup>66</sup>. Once recognised by macrophages or neutrophils, pathogens may be engulfed or destroyed<sup>66</sup>. However, the complement system provides an effective alternative method to directly kill cells, particularly GN bacteria.

### Complement

The complement system consists of approximately 50 soluble proteins, constantly circulating in the blood in high concentrations ranging from 1-1000  $\mu\text{g ml}^{-1}$  <sup>65,68,69</sup>. Once activated, complement can stimulate the adaptive immune system, induce inflammatory responses or directly kill pathogens. Complement activation requires one of three pathways; the classical, lectin and alternative pathways. These are proteolytic cascades, locally amplifying the response to PAMPs via the cleavage of proenzymes. The classical pathway is initiated by the binding of the protein C1q to two or more IgG antibodies or to a pentameric IgM antibody bound at the pathogen surface. This is followed by the binding and cleavage of several other proteins to activate C3. C3 can also be activated by the lectin and alternative pathways. The lectin does this via the binding of mannan-binding lectin to mannose and fucose in the LPS. The alternative pathway is an important positive feedback loop or is

activated spontaneously on the surface of all cells, but the inhibition of complement by host cells ensures only foreign cells are targeted<sup>66</sup>.

#### Assembly of the membrane attack complex

Once the complement component C3 has been activated by its cleavage into C3a and C3b, C3b is covalently bound to the pathogen membrane. This association of C3b with the target surfaces helps reduce killing of bystander cells<sup>66</sup>. As well as being a signal for the destruction of a cell by phagocytes, C3b makes up part of a membrane bound protein complex termed the C5 convertase<sup>68</sup>. This is the first stage of the terminal pathway of the complement system, ultimately leading to the lysis of bacterial cells by the assembly of 5 proteins (C5b, C6, C7, C8 and C9) into a large pore (~10 nm inner diameter) called the membrane attack complex (MAC).

The purpose of the C5 convertase is to cleave C5 to C5a and C5b<sup>70</sup> (Figure 1.5A, causing large conformational changes to the C5b structure<sup>71</sup>. C5b then forms a complex with C6 which lowers the membrane bending modulus<sup>72</sup>. C7 is then recruited and must form a covalently bound C5b67 complex on the OM for the rest of assembly to proceed<sup>73</sup>. Once C5b67 is anchored, C8 joins the nascent MAC assembly for an 'initiator complex' which can produce small holes in the cell membrane<sup>70</sup>. Complete MAC pores are then formed by the sequential addition of 18 copies of C9<sup>74</sup>.

The MAC has been shown to assemble on the surface of parasites, Gram-positive bacteria and red blood cells<sup>75,76</sup>. However, it predominantly targets GN bacteria. The specificity of MAC induced killing of pathogens is defined by its pathogen-specific initiation in the lectin and classical pathways, and via the inhibition of MAC formation on host cells by proteins in the blood or on the surface of host cells<sup>66</sup>. Defects in these regulatory mechanisms can lead to self-destructive, inflammatory diseases<sup>68</sup>. Membrane bound MAC inhibitors can be found on the surface of most host cells, for example, CD59 is a glycoprotein that potently inhibits MAC formation by binding C8 and blocking the addition of C9 molecules<sup>68</sup>. Without membrane bound MAC inhibitors, pores can readily accumulate in phospholipid membranes, although experiments on model membranes indicate specificity for negatively charged (e.g., bacterial) membranes<sup>77</sup>. Phospholipid membranes can also be more sensitive to

MAC than the bacterial OM, since lytic MACs can form on phospholipid membranes regardless of how C5b6 is formed, whereas C5b6 needs to be locally formed and presumably inserted by surface bound C5 convertases to yield bactericidal MAC assemblies<sup>53</sup>.

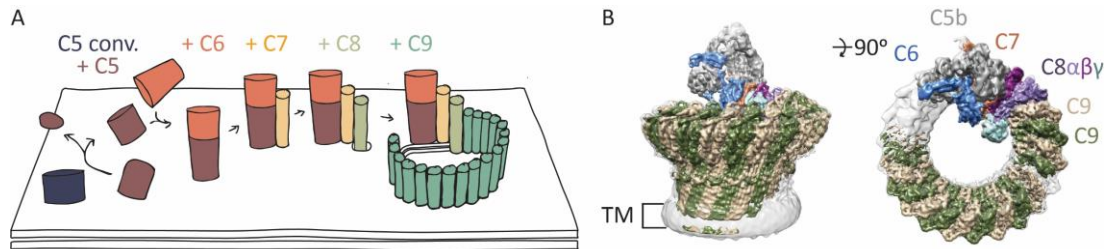


*Figure 1.5. (A) MACs form large pores in the surface of GN bacteria. C5 convertases are covalently bound to the OM. These convertases can then cleave C5 into C5a and C5b. C5a is a soluble anaphylatoxin that performs inflammatory roles elsewhere in the innate immune system. C5b stays at the surface to bind C6 and this complex loosely binds the OM. C7 joins and the complex is tightly bound to the surface. C8 binds and the complex can form small pores. Finally, ~18 copies of C9 sequentially bind to form a large pore. (B) Cryo-EM structure of the MAC from reference <sup>72</sup>. The transmembrane region makes up a very small portion of the barrel and the entire pore forms a flexible, split washer conformation. TM = Transmembrane region.*

### MAC structure

The Cryo-EM structure of the MAC (Figure 1.5B) reveals a giant  $\beta$ -barrel with an internal and external diameter of approximately 10 and 20 nm respectively<sup>74,78</sup>, large enough for ions and small proteins to freely diffuse across the membrane<sup>79</sup>. The ring itself is not complete: it forms a flexible split washer conformation with the final C9 monomer at one end and a stalk region consisting of C5b, C6, C7 and C8 at the other<sup>74</sup>. This stalk protrudes approximately 10nm from the rest of the ring, which itself extends approximately 10nm from the membrane (Figure 1.5B)<sup>74</sup>. The height of the MAC is striking. Only a small portion of the barrel crosses the membrane and the complex is not long enough to reach the IM. The rest of the barrel is stabilised by glycans bracing the strands approximately half-way up<sup>72</sup>.

### Mechanism of MAC-mediated lysis

Once inserted, the MAC quickly kills cells. Our understanding of how accumulation of MAC pores lyse GNs is mostly informed by work on red blood cells and synthetic lipid membranes subjected to MAC. Additionally, while there is evidence that the formation of only one MAC pore is sufficient for the lysis of red blood cells<sup>80</sup>, the number of pores required to kill a bacterial cell is not known.

Further information gained from red blood cell studies suggest the mechanism of MAC killing is by the disruption of ion gradients. However, these studies are flawed in two key ways. Firstly, they assume the presence of incomplete MAC pores, i.e., MACs may exist without 18 copies of C9<sup>80</sup>. This assumption is contrary to recent evidence that the rate limiting step in MAC pore formation is the addition of the first C9 and that incomplete MAC pores are not seen on live bacteria or synthetic membranes<sup>53,77</sup>.

Secondly, they assume an ionic gradient is disrupted by MAC on GN cells. While there is an ionic gradient across the IM, the highly permeable OM has no such gradient. So, to directly disrupt an ionic gradient, MACs would have to form on the IM. Yet it is unclear how that would occur: the MAC structure and dimensions demonstrate it can only span one membrane, efficient MAC insertion requires close association with the C5 convertase on the OM<sup>53,81</sup> and bacterial killing has been found to be independent of C5b6-8 entering the periplasmic space<sup>53</sup>. C9 may polymerise in solution but has not yielded lytic pores without C5b6-8<sup>77</sup>, leaving the mechanism of IM permeabilization unknown.

A possible killing mechanism would be that the formation of pores in the OM would allow the passage of the serum component lysozyme through bacterial membranes, where it can break down cell walls<sup>82</sup>. Accordingly, it has been shown that MACs sensitise GN bacteria to antibiotics and serum proteins, particularly lysozyme<sup>83</sup>. However, it has also been shown that lysozyme is not essential for MAC to kill bacteria<sup>53</sup>.

In brief, molecular biology has answered many questions around the antibacterial action of the MAC; however, the mechanism of MAC lysis is not answered. To better

understand the deposition of MACs onto live bacteria and track MAC progress as cells are lysed, nanometre information must be acquired on the surface of whole cells.

## 1.2 Atomic Force Microscopy

Atomic force microscopy (AFM) has been used for nearly 35 years to resolve nanometre topographic images of hard, flat samples<sup>84</sup>. Technological improvements meant the study of biological surfaces and molecules was feasible in the 1990s and added the possibility of force measurements to imaging. This was followed by whole cell imaging in the 2000s at low resolutions, which have been substantially improved since then, such that nanometre resolution is now achievable<sup>85</sup>.

Since AFM involves physical interactions with a surface (described in Chapter 2), the relatively stiff microbial cells lend themselves relatively well to high-resolution AFM imaging. Likewise, AFM is well suited to studying bacteria as they are usually  $\sim 1 \mu\text{m}$  in size so, to resolve any intracellular details, nanometre information is required. Furthermore, bacteria are single cell organisms, so their outermost layer or membrane is often a key, dynamic organelle. Outer surfaces of bacteria can be studied by AFM at higher resolution than super resolution fluorescence microscopy, on unlabelled samples and on live cells over time.

Unlike Gram-negative bacteria, the outer layer of Gram-positive bacteria is a thick cell wall, primarily made up of peptidoglycan. Cells can also be surrounded by a protective S-layer and AFM has revealed different arrangements depending on the distance from the underlying cell membrane<sup>86</sup>. Utilising time-lapse imaging, multiple rounds of cell division can also be seen<sup>87</sup>. This has shown the arrangement of peptidoglycan on *S. aureus* varies depending on the age of the cell wall<sup>88</sup> and that the stiffness is higher at division sites<sup>89</sup>. Arrangements of peptidoglycan have also been characterised in *L. lactis*, showing it is laid down perpendicular to the long axis of the cell<sup>90</sup>.

Another advantage of AFM is that it can be performed in liquid. By altering buffer conditions, the net like arrangement of PG in *S. aureus* has been shown to stretch

when turgor pressure is high<sup>91</sup>. On live, hydrated cells, the peptidoglycan of *S. aureus* was also shown to be more disordered and porous than previously thought, due to the action of hydrolytic enzymes. This was particularly true in older parts of the cell wall, while new peptidoglycan is formed in rings at the leading edge of dividing cells (Figure 1.6A)<sup>92</sup>. The abilities to control buffer composition and to image over time also showed the dynamic process of sporulation by adding germinant molecules to a dormant bacterial spore, uncovering new structural reorganisations of the spore coat<sup>93</sup>.

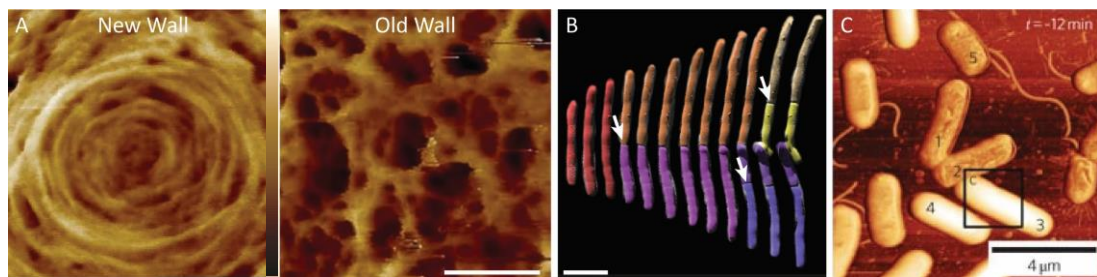


*Figure 1.6. (A) S. aureus peptidoglycan is laid down in concentric rings and, as the cell wall ages, hydrolytic enzymes convert the structure into a highly porous network. From reference 92. Scale bar is 100 nm. Colour bar is, left, 22 nm and, right, 58 nm. (B) Mycobacteria division can be tracked over time to show which poles are growing, revealing new mechanisms of growth. New poles (white arrows) stay in contact for the subsequent division. From reference 94. Scale bar is 4  $\mu\text{m}$ . (C) Cells within the same population are affected by AMPs at different rates. Cells 1, 2 and 5 have roughened due to AMP action, but cells 3 and 4 remain tall and smooth. From reference 95.*

Dividing *Mycobacteria* have also been studied extensively by AFM. The technique is ideal for studying *Mycobacteria* as they have very long generation times, so require long-term imaging<sup>96</sup>. Indeed, by tracking nanometre features on the surfaces of *M. smegmatis* over many generations, the division site of daughter cells was shown to be determined by a cleft in the grandmother cell<sup>97</sup>. Further investigation of division has shown that stress gradually builds in the cell wall at the division site until it triggers division<sup>98</sup>. Additionally, a combination of fluorescence and AFM has revealed a new mode of cell growth in *Mycobacteria*, previously seen only in yeast (Figure

1.6B). This mechanism, known as “new end take off”, involves the old pole of a cell providing much of cell growth, until the new pole rapidly elongates and the cell divides<sup>94</sup>.

The surfaces of GN bacteria have been studied by AFM to show densely packed porins in small regions of the cell surface<sup>52</sup>. High-speed AFM has also found diffusion constants of unlabelled porins in live bacteria are very low, suggesting porins form a stable net over the cell<sup>37</sup>. At a lower resolution, GN cells have also been seen with larger pores in their OM<sup>99</sup>. By combining AFM and genetics, the lipoprotein Lpp has been shown to determine cell stiffness by controlling the width of the periplasm and tethering the OM to the peptidoglycan<sup>16</sup>. The use of traditional molecular biology with AFM on whole cells has proved a powerful, but still underused, combination.

The effects of antimicrobials are extensively investigated using AFM on lipid bilayers<sup>63</sup>, but rarely on whole cells. One of the first such studies looked at dried cells after EDTA treatment, showing that the bacterial surface becomes highly corrugated<sup>100</sup>. This effect is often seen after treatment with AMPs as well<sup>101</sup>. Live cell imaging has also revealed new mechanisms of peptide action. For example, the stiffness of cells has been shown to decrease without pore formation for two membrane-active AMPs<sup>102,103</sup>, suggesting unknown lysis mechanisms. Further evidence of secondary mechanisms was seen for the Lpt toxin as cell death by known nucleoid condensation was enhanced by unexpected membrane poration<sup>104</sup>.

The action of AMPs can also be tracked in real-time. This has revealed heterogeneity in the population as cells are roughened by the peptide, CM15, at different timepoints (Figure 1.6C)<sup>95</sup>. The importance of media was later shown for this peptide as the roughening of cells seen in water does not occur in LB media, suggesting the activity of envelope repair machinery when cells are metabolically active<sup>105</sup>.

The scope for AFM to provide new perspectives on bacterial morphology and the action of antimicrobials at nanoscale resolution is evident. However, the use of this technique in microbiology is not extensive, particularly on Gram-negative bacteria.

## 1.3 Scope of Thesis

The aim of this thesis was to contribute to the understanding of bacterial outer membrane organisation and cell lysis using AFM. AFM is already an ideal technique for imaging microbial cells, but here, its combination with microbiology, labelling by globular proteins, immobilisation strategies, fluorescence microscopy and protein application has provided novel perspectives on long-standing biological questions.

After introducing the relevant experimental methods (Chapter 2), this thesis first describes the development of protocols for immobilisation of bacteria onto glass coverslips (Chapter 3). Establishment of this sample preparation was vital for the rest of the thesis and will be a valuable tool for future atomic force microscopists.

Once the general set-up of experiments is established, the study of native OMs is described, finding how OMPs are arranged over the entire cell and unexpected roles of specific proteins to the maintenance of OMP order (Chapter 4). The architecture of the OM is further investigated to find phase separation of the remaining OM components, LPS and PLs, and unanticipated, large-scale membrane reorganisation during cell division (Chapter 5).

Deposition of the MAC is then reported for experiments that demonstrate surprising bacterial resilience to MAC pores and suggest a previously unconsidered mechanism of cell lysis by MAC (Chapter 6). Finally, Chapter 7, summarises the results, provides an outlook based on the presented results, and concludes the thesis.

# Chapter 2

## Materials and Methods

In the following chapter, the preparation of bacteria for AFM is described, followed by the use of labels, protein application, peptide deposition and image analysis. A detailed description of the modes of AFM used, their set-up and operations are also provided.

### 2.1 Sample Preparation

#### 2.1.1 Bacterial Strains and Conditions

Bacterial strains and plasmids used are shown in Table 2.1. All strains and plasmids were provided by collaborators as specified in the table. A summary of the preparation of bacteria for AFM is shown in Figure 2.1. Unless otherwise specified, mid-log phase *E. coli* were prepared by incubating a culture overnight in 3 ml LB broth (Lennox) at 37°C in a shaking incubator. 30 µl of overnight culture was then diluted into fresh LB and grown for a further 2.5 to 3 hours. Where appropriate, LB was supplemented with 100 µg/ml ampicillin, 50 µg/ml kanamycin, 10 µg/ml tetracycline, 0.5% arabinose, 0.5% glucose or 0.1% fucose. For example, arabinose was used to induce expression of OmpR, or kanamycin was used to select for  $\Delta ompF$  cells.

0.5 to 1 ml of fresh culture was spun at 5,000 rpm for 2 minutes, the supernatant was removed and bacteria resuspended in HEPES buffer (20 mM HEPES, 120 mM NaCl, pH 7.4), PBS (10 mM phosphate buffer, 137 mM NaCl, 2.7 mM KCl, pH 7.4), PB (10 mM phosphate buffer, pH 7.4), milliQ water (mQ) or minimal media (MM: 1X M9 salts (A1374401, ThermoFisher), 2 mM MgSO<sub>4</sub>, 0.1 mM CaCl<sub>2</sub>, 0.36% glucose). Spinning and resuspension was repeated 3 more times to remove all LB which may contain debris or salts that could interfere with further processes.

Table 2.1. Strains and plasmids used, with the principal investigators of the labs that provided the cells

Strain	Genotype	Reference	Provided by
MG1655	K-12 F <sup>-</sup> λ <sup>-</sup> <i>rph-1</i>	106	Silhavy and Rooijackers
IMB312	MG1655 Δ <i>pldA</i>	107	Silhavy
IMB367	MG1655 Δ <i>mIaA</i>	107	Silhavy
IMB376	MG1655 Δ <i>mIaA</i> Δ <i>pldA</i>	107	Silhavy
IMB538	MG1655 Δ <i>ompR</i>	107	Silhavy
IMB551	MG1655 Δ <i>ompR</i> pBAD18:: <i>ompR</i>	107	Silhavy
IMB628	MG1655 Δ <i>ompR</i> pBAD18:: <i>ompR</i>	107	Silhavy
IMB589	MG1655 <i>leuB::tn10</i>	107	Silhavy
IMB531	MG1655 <i>lpxC101 leuB::tn10</i>	<sup>108</sup> and <sup>107</sup>	Silhavy
IMB587	MG1655 <i>lpxC<sub>R230L</sub> leuB::tn10</i>	<sup>109</sup> and <sup>107</sup>	Silhavy
IMB889	MG1655 + <i>wbbl</i>	107	Silhavy
JW0912-1	Δ( <i>araD-araB</i> )567 Δ <i>lacZ4787</i> :: <i>rrnB-3</i> λ <sup>-</sup> <i>rph-1</i> Δ <i>ompF756::kan</i> Δ( <i>rhaD-rhaB</i> )568 <i>hsdR514</i>	110	Kleanthous
JW2203-1	Δ( <i>araD-araB</i> )567 Δ <i>lacZ4787</i> :: <i>rrnB-3</i> λ <sup>-</sup> <i>rph-1</i> Δ <i>ompC768::kan</i> Δ( <i>rhaD-rhaB</i> )568 <i>hsdR514</i>	110	Kleanthous
BZB1107	<i>E. coli</i> B <sup>e</sup> , <i>ompF::Tn5</i> , Km <sup>R</sup> , Str <sup>R</sup>	111	Kleanthous
BL21(DE3)	<i>fhuA2 [lon] ompT gal</i> (λ DE3) [ <i>dcm</i> ] Δ <i>hsdS</i> λ DE3 = λ <i>sBamHlo</i> Δ <i>EcoRI-B int::(lacI::PlacUV5::T7 gene1) i21 Δnin5</i>	New England Biolabs	Kleanthous and Rooijackers
Plasmid	Description	Reference	
pCP20	Temperature sensitive FLP recombinase expressing vector	112	Silhavy
pBAD18	Expression vector containing the arabinose inducible araBAD promoter	113	Silhavy
pBAD18:: <i>ompR</i>	Arabinose inducible <i>ompR</i> overexpression vector	107	Silhavy
pGV28	IPTG inducible <i>ompA</i> with a streptavidin binding peptide in loop 1	114	Den Blaauwen

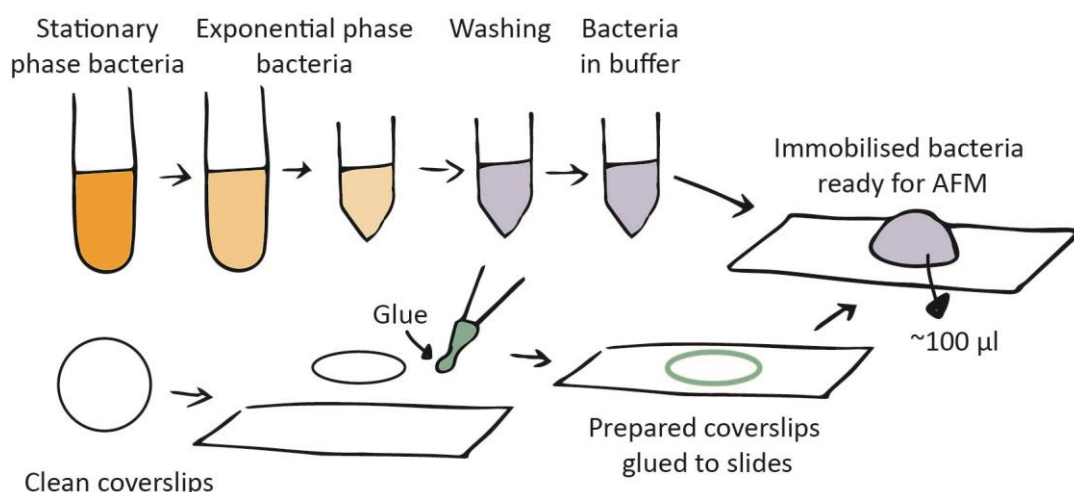


*Figure 2.1. Schematic of sample preparation. Bacteria were grown to stationary phase, diluted, allowed to reach the exponential growth phase and then washed in buffer. Clean glass coverslips were treated and glued to a glass slide. Bacteria were immobilised and unadhered cells washed off. The sample was then ready for AFM or further treatment. Cells remain adhered for the duration of experiments and imaging. Imaging took 1-3 hours, depending on the protocol.*

## 2.1.2 Substrate Preparation

### Glass cleaning

Glass is used as a substrate to facilitate combined optical and atomic force microscopy. 13 mm glass coverslips (VWR) were rinsed in a stream of mQ. They were then sonicated in 1-2% SDS at 37 kHz and 100% power in a Fisherbrand™ bath sonicator (Fisher Scientific) for 10 minutes. Next, they were rinsed in mQ, then ethanol and dried with nitrogen. They were then plasma cleaned at 70% power for 2 minutes in a plasma cleaner in air (Zepto, Diener Electronic). This procedure was performed twice to ensure coverslips were clean. They were then functionalised as described below.

### Glass functionalisation

Vectabond® and Poly-L-Lysine were used most commonly to functionalise glass, but gelatin and Cell-Tak™ were also tested.

For gelatin, a solution was prepared by adding 0.5 g of gelatin (G6144, Sigma) to 100 ml of mQ water just off the boil. The mixture was then swirled until all gelatin

dissolved and the temperature was 60-70°C <sup>115</sup>. Freshly cleaned coverslips were dipped into the warm gelatin solution, they were then removed and balanced on their edges until dry. Once dry, coverslips were glued to clean glass slides using biocompatible glue (Reprorubber thin pour, Flexbar, NY).

For Cell-Tak™ coating, clean coverslips were first glued to glass slides using biocompatible glue. A Cell-Tak™ solution was then prepared by mixing 1 ml 0.1 M sodium bicarbonate, pH 8.0 with 40 µl Cell-Tak™ (BD Diagnostics, USA) and 20 µl 1M NaOH. 100 µl of this solution was applied to a coverslip and incubated for 30 minutes at room temperature. Coverslips were then rinsed with a stream of mQ and nitrogen dried.

Poly-L-lysine (PLL) functionalisation was achieved by placing clean glass coverslips on a slide and applying a 100 µl droplet of 0.01% poly-L-lysine (P4832, Sigma). After 5 minutes at room temperature, the coverslips were rinsed in a stream of mQ, dried in nitrogen and glued to clean glass slides using biocompatible glue.

For Vectabond® coating, clean coverslips were submerged in a 50:1 solution of Acetone:Vectabond® (Vector Laboratories, USA) for 5 minutes, rinsed in mQ, nitrogen dried and glued to glass slides using biocompatible glue.

### 2.1.3 Sample Deposition

#### Immobilisation of bacteria

When testing immobilisation strategies and using PLL, 100 µl of bacteria in clean buffer was added to each fully prepared coverslip and incubated at room temperature. Incubation times were 15 minutes on gelatin, 5 minutes on PLL and 30 minutes on Cell-Tak™ or Vectabond®. Unadhered bacteria were washed away by rinsing in 1 ml of an appropriate buffer 3 times. When using MM on Vectabond®, cells were washed into 20 mM HEPES, applied to the coverslip for 5 minutes and washed with MM. If using MAC proteins, bacteria are washed into HEPES/BSA (20mM HEPES, 120mM NaCl, 2.5mM MgCl<sub>2</sub>, 0.1% BSA, pH 7.4) and incubated for 30 minutes at room temperature, before MAC protein addition, to reduce sequestering of proteins or peptides to the functionalised surface.

## 2.1.4 Protein, Antimicrobial Peptide and Label Addition

### Application of colicin labels

Colicin N<sup>1-185</sup>mCherry was provided by the Kleantous group and prepared as described in reference <sup>116</sup>. Colicin N<sup>1-185</sup>mCherry labelling was performed on bacteria before immobilisation. Exponentially growing cells were washed 3 times by spinning for 1 minute at 7,000 g and resuspending in minimal media 0.4% (MM 0.4%: 1X M9 salts (A1374401, ThermoFisher), 2 mM MgSO<sub>4</sub>, 0.1 mM CaCl<sub>2</sub>, 0.4% glucose). Cells were resuspended at an optical density of 0.5 at 600 nm, measured using a NanoDrop™ spectrophotometer (ThermoFisher). 250 µl bacteria were then spun, resuspended in MM 0.4% with 0.1 µM Colicin N<sup>1-185</sup>mCherry (unlabelled controls were resuspended in MM 0.4%) and incubated at room temperature on a rotary shaker for 5 minutes. Labelled cells were then washed with MM 0.4% 3 times by spinning and resuspending. Finally, cells were resuspended in 100 µl 20 mM HEPES, applied to a Vectabond® coated coverslip for 5 minutes, then washed 3 times with 1 ml MM 0.4%.

### Application of streptavidin labels

For streptavidin labelling, MG1655 pGV28 OmpA-SA1 cells were induced with 2.2 mg/ml IPTG for the final hour of their 2.5-hour growth. They were then washed 3 times in PBS and 100 µl was applied to a Vectabond® coated coverslip for 30 minutes. The bacteria were washed 3 times with PBS on the coverslip and then SYTOX™ was added. Cells were first imaged by AFM without labels. When adding streptavidin (SA101, Merck), 10 µg/ml was added to the sample on the slide, mixed vigorously with 50-100 µl volume and incubated on the microscope for 30 minutes. SYTOX™ was then reapplied and cells imaged.

### Application of the Membrane Attack Complex

The membrane attack complex (MAC) is the terminal pathway of an enzymatic cascade of the complement system, a complex protein network consisting of around 50 soluble proteins<sup>69</sup>. Rather than reconstituting the complement pathway, the MAC was added in a semi-purified manner by allowing the complement pathway to proceed up to the first stage of the terminal complement pathway, the surface

binding of C5 convertase. This was achieved by adding human serum that was deficient in C5, to generate C5 convertases covalently bound to the surface of bacteria. The cells could then be vigorously washed without dislodging these active proteases. MAC components were then added sequentially with more flexibility over concentrations and conditions.

Depending on the experiment, bacteria were exposed to serum when in solution, or after immobilisation onto glass. In solution, the serum stage was performed by pelleting bacteria in HEPES buffer at 5,000 rpm for 2 minutes. The supernatant was then removed and cells resuspended in HEPES/BSA buffer (20mM HEPES, 120mM NaCl, 2.5mM MgCl<sub>2</sub>, 0.1% BSA, pH 7.4) with 10% C5 deficient human serum (Complement Technology, Texas, USA). The bacteria were then incubated at 37°C in a shaking incubator. After 20 minutes, the serum was washed off by spinning and resuspending in fresh HEPES buffer 3 times. Bacteria were then immobilised on PLL coated coverslips.

If applying serum after immobilisation, as much of the liquid droplet was removed from the sample as possible (without drying the surface) and replaced by 100 µl HEPES/BSA buffer with 10% C5 deficient human serum. The sample was incubated at 37°C for 20 minutes, followed by 3 washes in 1 ml of HEPES buffer.

For the application of C5-9, serum coated, immobilised bacteria were washed once with 1 ml of HEPES/BSA buffer, the droplet was removed and replaced by 100 µl HEPES/BSA with purified complement components (Complement Technology, Texas, USA). Components were added in different concentrations or combinations depending on the experiment. For example, C5, 6, 7, 8 and 9 may be added together, or in two parts as C5, 6 and 7 followed by C8 and C9.

#### Application of melittin

For AFM on cells while targeted by the AMP melittin, exponential phase BL21 *E. coli* in HEPES buffer were immobilised onto PLL coated coverslips. Before imaging by AFM, the droplet was made up to 150 µl. When ready for the application of melittin, 50 µl of the droplet was removed and replaced with HEPES buffer containing melittin

for a final concentration of 5  $\mu\text{M}$  and SYTOX™ (see section 2.2.4). The droplet was then vigorously pipette mixed.

## 2.2 Atomic Force Microscopy

AFM probes surfaces by using a physical interaction between a needle and sample, to gain topographic images with ideally atomic resolution. A cantilever with a sharp tip is scanned across a surface, line-by-line. The tip and sample interact and forces are exerted on the cantilever, making it bend. A laser pointed at the back of the cantilever and reflected to a position-sensitive detector translates the bending to a signal. How the cantilever bending is used to generate topographic images depends on the mode of AFM operation.

In this thesis, all AFM was performed in liquid using tapping mode or force spectroscopy imaging. These modes are used because they generate low lateral forces which could deform soft biological samples. The set-up is summarised in Figure 2.2 and, in the following sections, the principles, parameters and optimisation of tapping mode and force spectroscopy for imaging are discussed.

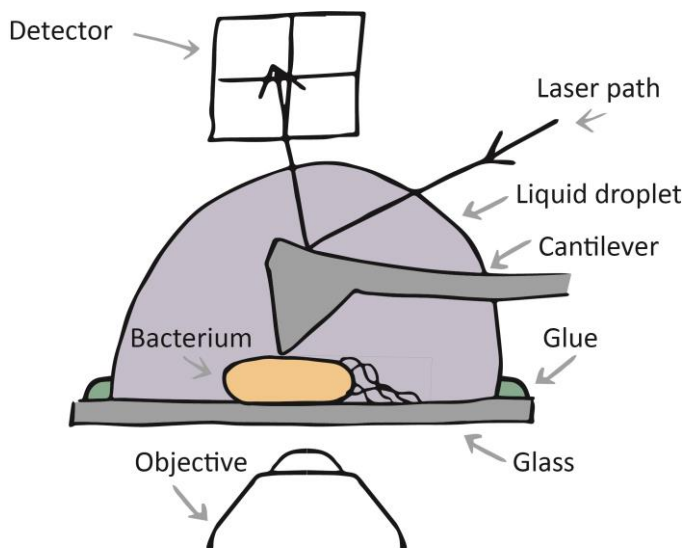


*Figure 2.2. General set-up for AFM in liquid. Bacteria are immobilised onto a glass coverslip for simultaneous brightfield and fluorescence microscopy. Glue around the edge of the coverslip maintains a liquid droplet.*

## 2.2.1 Force Spectroscopy Imaging

### Principles

Force spectroscopy is often used to get mechanical measurements that are calculated from a force curve generated by indenting a surface with the tip. However, force curves may also be performed at each pixel of an image to gain maps of the topography and mechanical properties of a surface. Figure 2.3 shows a typical force curve with corresponding cantilever positions: (1) the cantilever is free in solution, (2) as the oscillation moves the cantilever closer to the sample an attractive force pulls the cantilever to the surface, (3) the cantilever continues to move down until a pre-determined maximum force is exerted on the sample, (4) the cantilever is retracted, experiencing attractive forces that hold the cantilever to the surface, (5) the cantilever overcomes the attractive forces and is pulled off the sample, (6) the cantilever is returned to its original position.

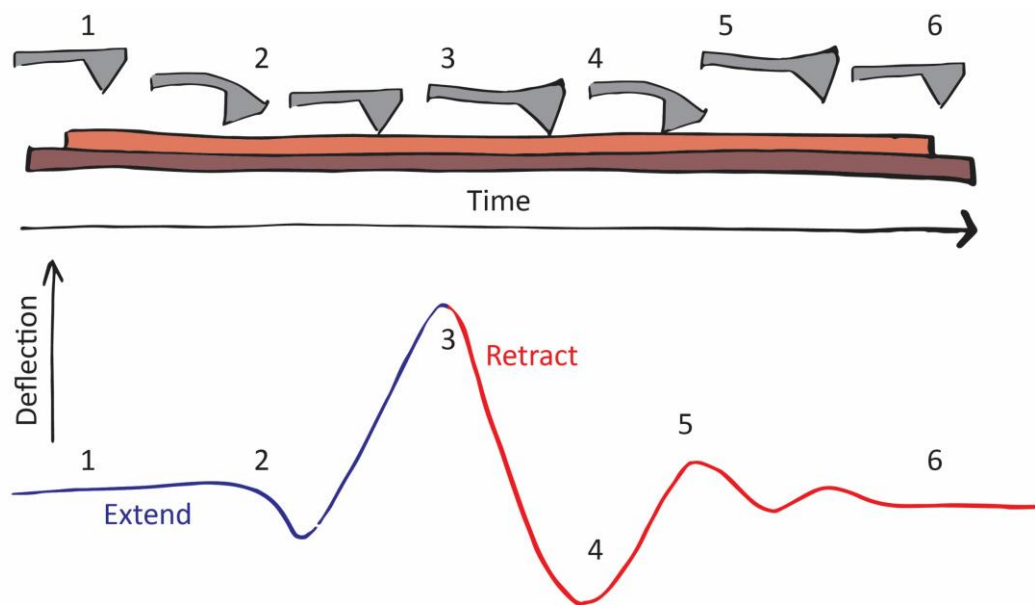


*Figure 2.3. Principles of force spectroscopy imaging. A force curve is performed at each pixel. The movement of the cantilever as the force curve is performed is represented above, each cantilever stage is at the same pixel but different time-points.*

With a force curve taken at each pixel, the height is taken as the change in Z position between the baseline (when the cantilever was free in solution) to the position when the maximum force is reached. Other properties can also be calculated. For example,

at stage 4 when the cantilever is being pulled from the sample, the force required to overcome the attractive forces is used to calculate the adhesion. Another property accessible via a force curve is the stiffness.

The stiffness of a sample can be determined by how steeply the cantilever deflection increases as it is pushed onto the sample. This gradient can be used to find the Young's modulus via the Hertz model (see section 2.3.4). The Young's modulus is a measure of the stiffness of a material; the stiffer the sample, the higher the Young's modulus. The Hertz model makes various assumptions about the properties of the material which are important when using AFM to assess stiffness: the materials should be homogenous, purely elastic and infinitely thick<sup>117</sup>. Obviously, a cantilever and a bacterium are not infinitely thick, however, the indentation made is small (~10 nm) compared to the overall size of the bacterium and cantilever (>1  $\mu\text{m}$ ). Regarding the assumption that the material is purely elastic, the absence of plastic effects may be verified by a lack of permanent deformations and, as long as the force curve is applied slowly enough, viscoelastic effects may be ignored.

However, bacteria are not homogenous samples. Therefore, the calculated Young's modulus cannot be taken as an absolute value, rather as an effective Young's modulus. This allows the comparison of the stiffness of regions within the same sample and between similar samples, but not between very different samples. A final assumption when using the Hertz model is the Poisson ratio. Since this often cannot be determined experimentally, it is assumed to be 0.5<sup>118</sup>.

### Microscope and cantilevers

Force spectroscopy is performed in JPK's QI™ mode (JPK, Germany; now Bruker AXS, CA, USA). QI™ mode was performed on the Nanowizard III AFM with an UltraSpeed head (Bruker AXS, CA, USA) with a FastScanD (Bruker AXS, CA, USA) cantilever (0.25  $\text{N m}^{-1}$  spring constant and 110 kHz resonant frequency).

### Parameters and optimisation

To get accurate and reliable force curves, and to acquire images based on such force curves over larger areas, there are several parameters that must be optimised. The maximum force (referred to as the setpoint) is the most important of these: the

higher the maximum force, the more defined the force curve and the more reliable the calculated height will be. However, a high force can alter or damage the sample<sup>119</sup>, this is particularly true for biological samples which are often softer and more fragile than typical AFM samples. For this thesis, a setpoint of 0.1 nN was used. Also, in QI™ mode, the tip velocity is constant (i.e., it does not slow down as it approaches the surface) which can often lead to ‘overshooting’ of the intended peak force. Therefore, the Z speed was kept to 30  $\mu\text{m s}^{-1}$ .

A further parameter is the Z length, which can be quantified as the Z distance over which the cantilever (or sample) is ramped. By making it as low as possible, the tip will spend a larger proportion of the time in contact with the sample surface, where image contrast is determined. A priori, this benefits high-resolution imaging. However, when it is too low, the cantilever may not be released from the attractive forces of the sample upon the retraction of the cantilever before initiating the next ramp; this results in errors in the calculated baseline. Furthermore, when a sample has very high surface features, the Z range must be sufficiently high for the peak of oscillation to exceed an oncoming feature, thus avoiding a lateral collision between the tip and protruding sample features. QI™ mode images were recorded at 500x500 nm (and 128x128 pixel) on the surface of bacteria, therefore surface features were relatively small, so a Z range of 90 nm was used.

## 2.2.2 Tapping Mode

### Principles

In tapping mode, a cantilever is oscillated above the sample surface. The cantilever is then moved down towards the surface until a drop in the amplitude of oscillation is detected. This drop is due to two types of tip-surface interactions: firstly, the proximity of the sample allows a dissipation of energy from the cantilever into the sample surface, damping the oscillation; secondly, any repulsive forces between the tip and the sample lead to an effective stiffening of the cantilever, as these forces push the tip back towards the equilibrium position of the oscillation. When the amplitude drops below a pre-set magnitude (the setpoint), the feedback moves the cantilever away from the sample until the amplitude returns to the setpoint (Figure

2.4). The tip is then scanned across the sample, maintaining the setpoint. The distances required to move the cantilever to return the amplitude to its pre-set value is taken as the height. Similarly, when the amplitude rises above the setpoint, the feedback will approach the cantilever to the sample.

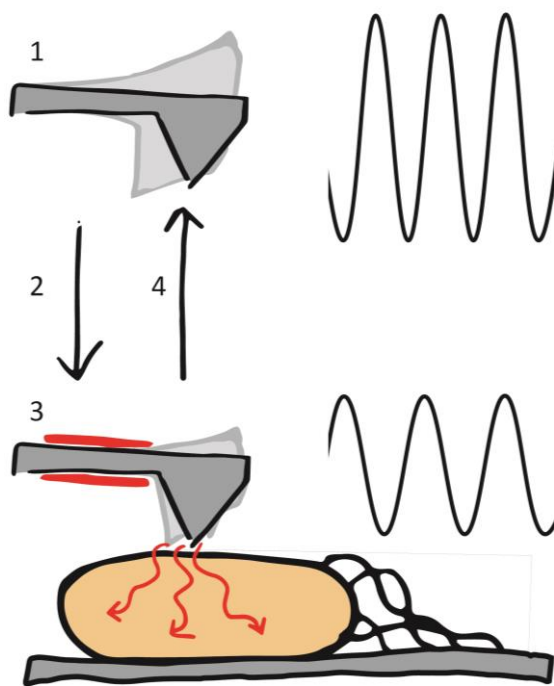


*Figure 2.4. In tapping mode AFM, the cantilever is oscillated close to the resonant frequency and uses changes in the amplitude to detect the sample surface. (1) The cantilever is free in solution and oscillated just below its resonance. (2) Moving the cantilever down leads to (3) a change in the phase of oscillation and a drop in amplitude due to effective stiffening of the cantilever and energy dissipation into the sample (shown in red). (4) Moving the cantilever up increases the amplitude again.*

The frequency the cantilever is driven at is an important factor in tapping mode: a frequency lower than the resonance is always chosen. This is so that damping and stiffening of the cantilever both lead to a reduction in the detected amplitude and these effects do not cancel each other out, as follows. Damping will always lead to a reduction in amplitude (Figure 2.5). However, as the effective stiffness increases, the resonance frequency of the cantilever increases. This means that, if the cantilever is being driven at a frequency higher than its free resonance, stiffening will lead to an increase in amplitude, countering the decrease due to damping. By contrast, if the cantilever is being driven at a frequency lower than its free resonance, the stiffness still increases the resonance, but the amplitude decreases because the resonance is moved further from the drive frequency, such that both effects (damping and stiffening) lead to a reduction in amplitude (Figure 2.5).

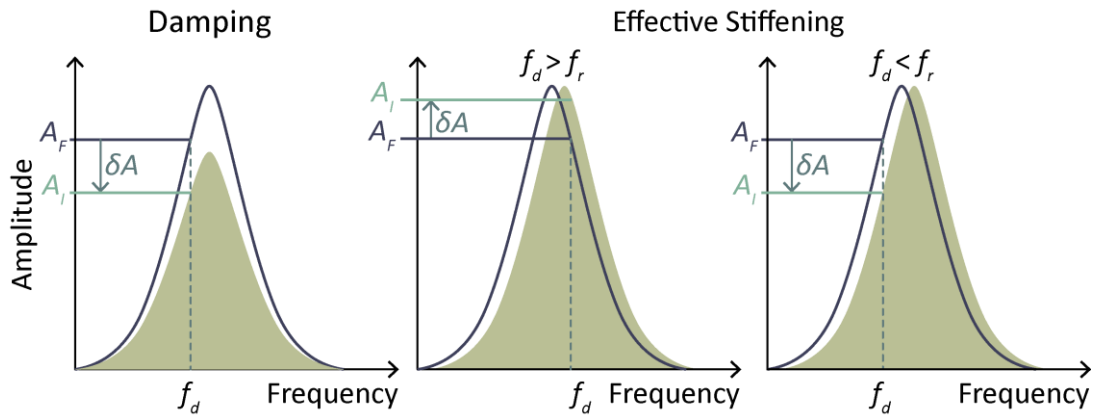


Figure 2.5. The effect of tip-sample interactions on a frequency sweep due to damping and effective stiffening. Damping reduces the overall amplitude of oscillation, which always leads to a drop in measured amplitude. Effective stiffening shifts the resonance to the right. This means that when the cantilever is driven above the resonance, the measured amplitude increases. Instead, the cantilever is driven below the resonance so that the measured amplitude drops. This works constructively with the damping effect in reducing the amplitude, thus yielding a less ambiguous measure of tip-sample proximity.  $A_F$  = Free amplitude,  $A_I$  = Interacting amplitude,  $f_d$  = Drive frequency,  $f_r$  = Free resonance frequency. Dark green line represents the frequency when the cantilever is free in solution. Light green peak represents the shifted frequency with tip-sample interactions.

Another key parameter to be optimised is related to the gains of the feedback control loops that is used to continuously adapt the tip-sample distance to maintain the setpoint while tracing the surface. There are two types of feedback control used in AFM: proportional and integral, but they are generally controlled by one parameter. In proportional control, the difference between the setpoint and signal is defined as the error, and the tip Z position is then adjusted by a response that is proportional to this error. The downside is that the tip Z position will always revert to the same zero reference value when the error is zero, resulting in an oscillation around the setpoint, like an on-off control loop<sup>120</sup>. To overcome this problem, integral control is also used. Integral control is the most important feedback; it pushes the signal back to the setpoint by defining the tip position via an integration of the error over time, such that the tip position can stabilise at whichever value required for the tip-sample interaction to match a given setpoint. Increasing these gains will lead to a faster

response, but too high and the correction signal will be too fast for the piezo to respond and the signal will start to oscillate (“ringing”)<sup>120,121</sup>. Gains were generally optimised by increasing to the point of ringing, then decreasing to 50-60% of this value.

As well as height, a further data type that can be gained from tapping mode is the phase of the cantilever oscillation. This is the difference in phase of the measured oscillation compared to the phase of the drive oscillation. Such differences in phase changes depend on tip-sample interactions and on a combination of surface properties including elasticity, adhesion and height<sup>122</sup>. This makes the phase particularly useful for distinguishing features with different mechanical properties. This can, for example, apply to a protein inserted into a membrane. It should be emphasised that AFM phase images represent a contrast due to material properties, which does not necessarily correlate with the sample topography as represented in the AFM height images.

#### Microscope and cantilever

Tapping mode was used to image bacteria whenever possible because it is faster than the QI™ mode also available on the used microscope. It was also used in combination with brightfield microscopy. Tapping mode was used on the Nanowizard III AFM with an UltraSpeed head (Bruker AXS, CA, USA) with a FastScanD (Bruker AXS, CA, USA) cantilever (0.25 N m<sup>-1</sup> spring constant and 110 kHz resonant frequency).

#### Parameters and optimisation

Before imaging by tapping mode, the resonant frequency of the cantilever was found using the thermal tune methods described in section 2.2.3. The drive frequency was then chosen by driving the cantilever at a set range of frequencies (a frequency sweep) to find how the system responds to such actuation. In theory, this would produce a curve similar to the thermal tune, but with a greater magnitude. However, in practice the frequency sweep is often a ‘forest of peaks’ with resonance contributions from the sample, sample holder and cantilever holder that are all affected by the actuation piezo (Figure 2.6). Since the resonance peak was often hidden in the frequency sweep; a smooth, tall peak was chosen as close to (but lower than) the resonance as possible. An amplitude slightly less than measured in the

sweep was then chosen as the setpoint (Figure 2.6), this reduced false engages but ensured the tip did not crash during engagement. As in force spectroscopy, the setpoint in tapping mode was kept as gentle as possible to avoid sample deformation, but strong enough to keep the tip engaged with the surface.

Evaporation of the sample liquid, an inevitable consequence of an open sample in fluid and exacerbated by heat from the lamp used for brightfield imaging, meant the 'forest of peaks' shifted and changed in magnitude as damping was reduced and the liquid droplet changed shape<sup>123</sup>. Therefore, the drive frequency and setpoint were checked and altered regularly, throughout imaging.

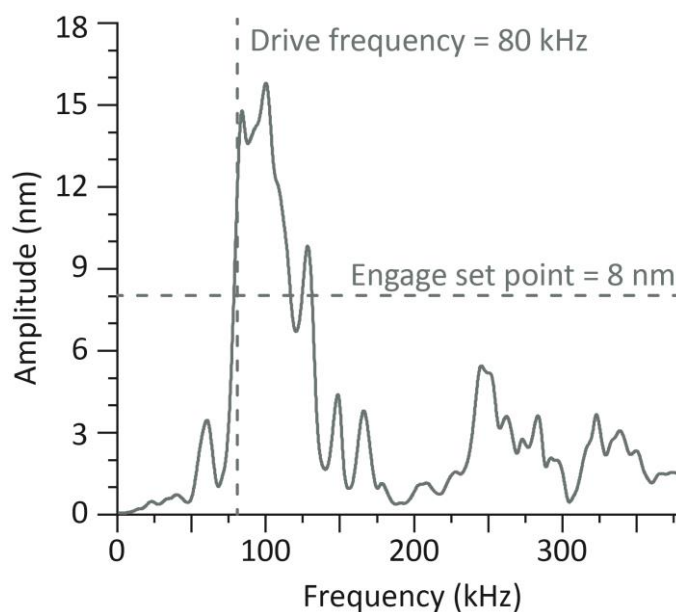


*Figure 2.6. A frequency sweep shows the 'forest of peaks' generated when using piezo-actuated tapping mode in liquid. The left side of the peak closest to, but lower than, the resonant frequency is chosen as the drive frequency.*

### 2.2.3 Calibration

Before imaging bacteria by AFM, the cantilever was calibrated to find the spring constant, the sensitivity at which cantilever deflections were detected and, for tapping mode, the resonant frequency. This was so that imaging parameters were comparable between cantilevers and so that they could be controlled in terms of nanometres or picoNewtons, rather than the voltage detected by the photodiode. In tapping mode, this is important because it allows the amplitude of oscillation to be set depending on the height of protrusions at the surface. In force spectroscopy, it is important to know the force applied to the sample to avoid damage. For accurate calibration, the cantilever was put in contact with the sample, thus calibrating the cantilever detection against the (calibrated) Z movement of the tip scanner.

However, a less accurate, less invasive and faster method of calibration is by measuring the thermal noise of the cantilever (“thermal tune method”).

### The Thermal Tune Method

A thermal tune measures the natural vibrations of the cantilever due to the Brownian motion of molecules in the liquid droplet. Several properties may be determined from a thermal tune including the resonant frequency, Q-factor and sensitivity. A typical thermal tune is shown in Figure 2.7A. The resonant frequency is the frequency that has the highest recorded amplitude. The sensitivity is estimated from the relationship between the total amplitude due to thermal fluctuations and the spring constant. The spring constant,  $k$ , may be calculated by  $k = \frac{k_B T}{P}$ , where  $k_B$  is Boltzmann’s constant,  $T$  is the temperature and  $P$  is the area under the peak fitted on the thermal tune (Figure 2.7A)<sup>124,125</sup>. For higher accuracy, the spring constant can be calculated using a contact-based method (see below). However, this could blunt the tip: making it unusable for high-resolution AFM. Therefore, the spring constant quoted by the manufacturer was assumed to be correct when using tapping mode.

### The Contact-based Method

Since QI™ mode is used to acquire mechanical properties, it requires an accurate calibration. However, contact calibration risks blunting the tip, therefore a thermal tune was used before imaging for an approximate spring constant and sensitivity. To get a more accurate sensitivity (and thereby allowing calibration of the spring constant by measuring the thermal noise), a contact-based method must be employed. In this mode of calibration, a force curve is generated by pushing the cantilever into a clean, hard surface. Once the tip is in contact with the surface, the cantilever continues to be lowered and the deflection of the cantilever increases linearly with the Z motion of the scanner, until a predefined deflection is reached, the cantilever is then retracted. The gradient of the linear response is used to calculate the sensitivity of the cantilever i.e., how much the deflection of the laser (as measured in V) changes with respect to movement of the cantilever (as measured in nm; Figure 2.7B). Here, a peak force of approximately 0.2 nN and a Z length of 1 μm were used. A thermal tune was then performed. The relationship used to

estimate the sensitivity from the manufacturer's spring constant can be reversed to calculate an accurate spring constant.

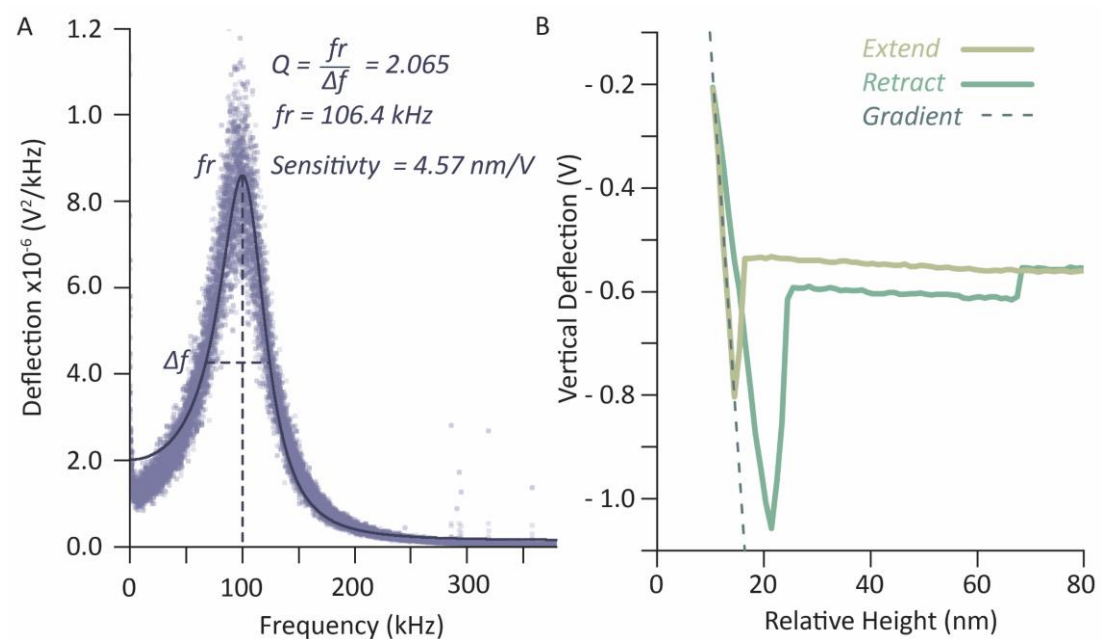


Figure 2.7. (A) A typical thermal tune of a cantilever in liquid, here fitted with a simple harmonic oscillator mode (continued line). The resonant frequency ( $f_r$ ) is at the highest deflection. A typical sensitivity value is also shown. (B) A force curve generated for contact-based calibration. The gradient of the region of the extend curve in contact with the surface is then used to determine an accurate sensitivity, this is then used to calculate an accurate spring constant,  $k$ , via  $k = \frac{k_B T}{P}$ , where  $k_B$  is Boltzmann's constant,  $T$  is the temperature and  $P$  is the area under the peak fitted on the thermal tune<sup>125</sup>.

## 2.2.4 Combined Brightfield and Fluorescence Microscopy

An Andor Zyla 5.5 USB3 fluorescence camera on an Olympus IX 73 inverted optical microscope was used. Bacterial cell death was assessed using SYTOX™ green nucleic acid stain (S7020, Sigma). 0.3-1  $\mu$ l of 5 mM stain was added to the sample and images acquired. If the stain bleached, more SYTOX™ was added. SYTOX™ stains dead cells as it can only enter the cytoplasm, where it fluoresces upon nucleic acid binding, once both the outer and inner membranes are permeated.

## 2.3 Data Analysis

During data analysis, several custom scripts were written (in MATLAB, Python and ImageJ macros) and can all be found in the Hoogenboom-Lab (<https://github.com/hoogenboom-lab/image-analysis>) and AFM-SPM (<https://github.com/AFM-SPM/TopoStats>) repositories on GitHub.

### 2.3.1 Optical Images

Brightfield and fluorescence images were analysed using FIJI-ImageJ<sup>126</sup>. Generally, the contrast of images was set by adjusting the limits of the display range and images converted to 8-bit. If required for image representation, the fluorescence and brightfield channels were merged with cell death shown in the red channel and brightfield in grey.

For counting immobilised bacteria, custom ImageJ macros were used with settings and parameters as follows. First, each image was cropped to 360 x 240  $\mu\text{m}^2$  to ensure the field of view was all in focus, bacteria were then counted by converting images to binary and using the “Analyze Particles” function. Converting an image to binary required different image processing depending on the quality of image and number of bacteria in each field of view. The effectiveness of image processing was assessed by comparison with original images.

Generally, brightfield images were smoothed, converted to binary and noise removed using the ‘despeckle’ function in FIJI-ImageJ. To remove large background features, bacteria were identified using the ‘find edges’ function, or a background subtraction (rolling ball radius of 25 pixels, pixel size 0.32  $\mu\text{m pixel}^{-1}$ ) was applied. For fluorescence images, a threshold was applied (by the Otsu or Default method) and the image despeckled. When the density of bacteria was high, a watershed algorithm was used to separate individual cells; and when no bacteria were present, the image was not processed. The number of cells was counted as the number of particles with an area between 2 and 300 pixels, corresponding to approximately 0.6 to 100  $\mu\text{m}^2$ . This range was large to account for bacteria that are elongated or rounded due to stress.

### 2.3.2 AFM Processing

Processing of bacterial AFM images is complicated by large height changes and different requirements for analysis, so several methods were used. For MAC data, a Python script using Pygwy (from Gwyddion 2.52; <http://gwyddion.net/>)<sup>127</sup> and originally adapted from AFM-SPM/TopoStats<sup>128</sup> was used. The script involved different operations depending on the data type, a summary of the order of operations is shown below:

#### Height image

- a. When the pixel range was large the bottom 50% of the data was masked to be ignored from subsequent flattening.
- b. The flatten base function was applied. This is an automated function that uses a combination of facet, plane and polynomial levelling to reduce variation in images with large features on a relatively flat background<sup>127</sup>.
- c. Scan-lines were aligned by fitting a 2<sup>nd</sup> order polynomial to each line, then subtracting this from the data. This removes the curved background of the bacterial cell.
- d. The mask was removed.
- e. A 1-pixel gaussian filter (typically 1.024 pixels nm<sup>-1</sup>) was applied to remove high frequency noise.
- f. The lowest pixel was set to zero to normalise data.

#### Phase image

- a. Scan-lines were aligned by fitting a 2<sup>nd</sup> order polynomial to each line, then subtracting this from the data. This removes the curved background of the bacterial cell.
- b. A 1-pixel gaussian filter (typically 1.024 pixels nm<sup>-1</sup>) was applied to remove high frequency noise.
- c. The lowest pixel was set to zero to normalise data.

For AFM of native membranes, large tapping mode images were not post-processed but the colour scale was set in Gwyddion. Small images were first processed with another Python script using Pygwy (from Gwyddion<sup>127</sup>) and originally adapted from AFM-SPM/TopoStats<sup>128</sup>. The script took Height and Phase channels of each image,

applied a first order polynomial fit to align rows and exported the file as a text image. A custom FIJI-ImageJ<sup>126</sup> macro imported the text image, applied a Bandpass filter (1-50 pixels) and a 1 pixel gaussian blur (1.024 pixels nm<sup>-1</sup>), then normalised the mean pixel value to zero. Gwyddion was used for image representation and height profiles. Further analysis was performed as described below.

### 2.3.3 Further Image Analysis

#### Localisation of labels

To localise colicin N<sup>1-185</sup>mCherry and streptavidin labels on bacteria, masks of network and patch regions were marked manually in FIJI-ImageJ using the phase channel. Labels were poorly visible in the phase, so potential bias was reduced. The labels were then found by applying a 0-20 pixel bandpass filter and a 2-pixel gaussian blur to the height channel, next peaks with a prominence of 0.5 nm were then found using the Find Maxima function in FIJI-ImageJ. The number of labels per  $\mu\text{m}^2$  in patch and network areas was calculated in MATLAB (Mathworks).

#### Pore and patch finding

For pore and patch analysis, high-resolution whole-cell images were required. Therefore, 500 nm scans were performed across the bacterial surface. The approximate location of each scan was recorded in the jpk files and accessed in the JPK data processing software. Individual phase scans were then accurately overlaid in FIJI-ImageJ by comparing surface features in each image. Once overlays covering the accessible cell surface were complete, a mask of patches was generated by manually marking patch edges in FIJI-ImageJ. Any patch less than  $\sim 400 \text{ nm}^2$  was ignored as they were often ambiguous. To calculate the relative patch area, the area of bacterial surface imaged was outlined manually and the percentage imaged area taken up by patches was calculated in MATLAB (Mathworks). The FIJI-ImageJ shape descriptors function was used to find patch aspect ratios and individual patch areas.

For pore locations, the Find Maxima function in FIJI-ImageJ was first used to find potential pores. Any points that fell outside the imaged area were ignored and the remaining points were exported as coordinates. The Enhance Local Contrast (CLAHE) function was then used to normalise contrast across the surface since contrast is

usually higher at the edges of cells. Uncorrected, this led to central pores being missed in subsequent analysis.

The corrected image and potential pore coordinates were then imported into a machine learning model. The model was trained on manually picked pores, made by Joel Forster\* and described in detail in reference <sup>107</sup>. Briefly, it took each potential coordinate in turn and raster scanned an 11x11 pixel region centred on the coordinate. If a pixel looked like a pore it was classified as such. Once all coordinates had been checked, those that were in the same pore were merged and the centre was recorded as a true pore location.

Diffusion constants<sup>†</sup> were determined from positions of pores manually tracked in subsequent images, next measuring the mean square displacement as a function of time  $t$  lapsed between different positions  $r$ , after which the 2D diffusion coefficient  $D$  was determined from the slope of the linear fit from  $\langle r^2 \rangle$  vs  $t$ , via  $\langle r^2 \rangle = 4 D t$ .

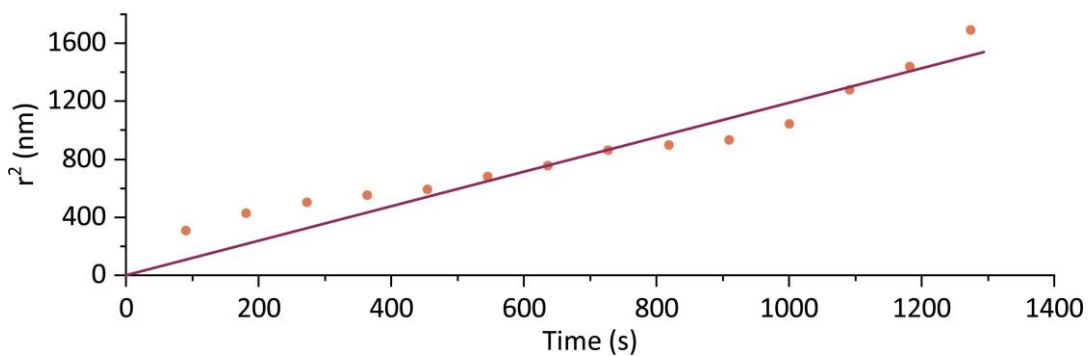


Figure 2.8. The diffusion coefficient is calculated from the gradient of a linear line (purple) fitted to  $\langle r^2 \rangle$  vs  $t$  (orange).

### MACs on bacteria

By AFM, MACs on bacteria appeared highly varied, in contrast and in roundness. Within the same scan, pores had high or low contrast from the background depending on the surface properties. They also appear more or less round depending on their position on the bacteria: since bacteria are curved the pores on the edges of bacteria were angled away from the  $x$ - $y$  plane, making them less circular in the image.

---

\* Department of Physics and Astronomy, University College London, WC1E 6BT London, UK

† Calculated by Dr Nikola Ojkic (Department of Physics and Astronomy, University College London, WC1E 6BT London, UK)

Therefore, automated picking was not feasible and pores were manually identified using the multipoint selection tool in FIJI-ImageJ. Usable regions of each scan were also marked and the area calculated. This data was then used to normalise the number of MACs per unit area.

### Packing analysis

To characterise networks of pores and MACs, several analyses were used. Most simply, nearest neighbour distances were used to find the density of features. This was performed using coordinates imported into MATLAB to calculate distances between every pore and rank them. To gain insight into packing arrangement, pore coordinates were also used in the calculation of the angular distribution, with coordinates within a 15 nm radius used to find the angle between each pore and its neighbours. MATLAB was also used to find the radial distributions of MACs to determine whether long distance clustering exists. All calculations used custom MATLAB scripts.

Finally, an analysis of whether MACs form in branches was performed in MATLAB and FIJI-ImageJ<sup>126</sup>. The process was as follows: (1) MAC locations were plotted in MATLAB, (2) Each MAC was plotted as a filled circle and dilated to let close circles touch, (3) the resulting shape was skeletonised, (4) skeletons from single MACs were removed, (5) the FIJI-ImageJ 'Analyze Skeleton (2D/3D)' function was applied and the resulting images analysed to find the longest branch of each skeleton.

When determining if MAC distribution and branching was random, random distributions of MAC were simulated for areas that corresponded to the actual scan sizes (such that boundary conditions were matched between experimental data and simulated data), with calculations repeated on 5 sets of random coordinates in the same regions using MATLAB. A final analysis was to split the cell surface into regions and determine whether they were more likely to fall in different regions of the cell, this was also done with a custom script in MATLAB.

### 2.3.4 AFM Force Curve Analysis

AFM force curves were analysed using JPK data processing software. A QI-Data file was opened and the force curves batch processed using the following operations:

recalibration, vertical tip position, baseline subtraction and elasticity fit. Recalibration was done to use the more accurate values of the contact-based calibration performed post-imaging. This was followed by a correction of the vertical deflection to the vertical tip position; this removes the displacement measured as the cantilever is moved toward the sample, such that only the deflection of the cantilever by the sample is used. A baseline subtraction was then used to remove any offset due to the vertical deflection being non-zero when the tip was not interacting with the sample. This may have occurred due to inaccurate positioning of the laser on the photodiode, or drift. This operation was performed by subtracting the mean value of the first 50% of the extend curve from the entire force curve, or (if the offset was not constant) by subtracting a linear tilt<sup>117</sup>.

Finally, the effective Young's modulus,  $E$ , is calculated using the Hertz model,  $F = \frac{E}{1-\nu^2} \frac{4\sqrt{R_C}}{3} \delta^{3/2}$ , where  $F$  is the force applied,  $\nu$  is Poisson's ratio (see section 2.2.1),  $R_C$  the radius of tip curvature and  $\delta$  is the vertical tip position. The entire extend curve was used and the tip shape was assumed to be a paraboloid with tip radius of 1 nm. The quality of fit was assessed by visually inspecting the force curve analysis. The effective Young's modulus of each pixel was represented as a 'stiffness map'. This was done using Gwyddion 2.52. No post-processing was performed except choosing a height scale to best show the range of values.

### 2.3.5 Statistics and Graphing

Statistics were performed either in MATLAB (Mathworks) or Origin (OriginLab, MA, USA) and graphs were plotted in Origin (OriginLab, MA, USA). Statistics are from a paired two-sided Student's  $t$ -tests, a one-way ANOVAs with a Tukey's  $t$ -test or a  $\chi^2$  test. All error bars are standard deviations and centre lines are means.

## 2.4 Concluding Remarks

This chapter describes the implementation of AFM for imaging of bacteria. The substrate preparation and bacterial immobilisation are also described, further established and validated in Chapter 3, and essential for all subsequent chapters. The

here described methods also include a description of labelling methods that, to my knowledge, have not previously been employed for AFM, and extensive image processing that provide the basis for Chapters 4 and 5. Finally, it has been described how bacteria are exposed to complement proteins, and how the spatial distribution of these proteins is analysed, of particular relevance for Chapter 6.

# Chapter 3

## Immobilising Bacteria for AFM

Arguably, AFM is the technique of choice for accurate and label-free molecular measurements on the surface of live cells<sup>53,81,129–132</sup>. AFM performed in water or physiological buffers, including cell culture media, allows the acquisition of nanometre resolution images with no ensemble averaging, under physiological conditions<sup>133</sup>. However, AFM requires the reliable immobilisation of cells onto an appropriate surface. In the following chapter, the establishment of two effective and reliable immobilisation techniques is described.

### 3.1 Introduction

During AFM, cells must be accessible to the tip. Therefore, it is not an option to sandwich bacteria between agar pads, as for fluorescence microscopy. Furthermore, the cells must be adhered robustly enough for them not to be dislodged by the forces exerted by the AFM probe. Many substrates have been used for immobilisation with varied success. Microwells can physically trap bacteria<sup>87</sup>. This can be achieved in a range of buffers including growth media and requires no chemical interactions between substrate and bacteria, thus leaving cell viability unaffected. However, the trapping of cells requires appropriately sized holes, which itself depends on the species of bacteria. *E. coli* and *B. subtilis* have been immobilised using a microfluidic device that also allowed simultaneous fluorescence imaging, although the fabrication of these devices is time consuming<sup>87,105</sup>. Furthermore, the efficiency of capture by microwells is unreliable: some have reported low efficiency<sup>134</sup>, while others succeed in tracking cells over long time periods with high resolution<sup>87,92</sup>. To immobilise round, mechanically strong cells, polycarbonate filters may be used<sup>86</sup>. But this approach is not feasible for most species due to their size and the mechanical stress exerted on cells by passing suspensions through the membrane is a disadvantage<sup>134</sup>.

Generally, mica is the most common substrate for AFM as it can be cleaved to provide a clean, atomically flat surface<sup>135</sup>. However, for cell imaging, it is more convenient to have the option of combining with brightfield and fluorescence microscopy for several reasons: a visual check before AFM can quickly determine how well cells are adhered, brightfield microscopy can be used to position the cantilever and fluorescence can be used to ensure cells are alive. Thus, glass coverslips or slides are commonly used in AFM of cells<sup>96,136</sup> and are used throughout this thesis.

Ensuring the adherence of cells onto glass is a prerequisite for AFM sample preparation but a covalent attachment of bacteria to the glass could affect cell viability and should be avoided<sup>87</sup>. An ultimately reliable immobilisation method would be compatible with physiological buffers and have no effect on cell viability or morphology. Furthermore, such a method should meet time considerations of AFM imaging, particularly when visualising cellular or cell-related processes over prolonged periods. Thus, the choice of immobilisation methods for accurate and reliable AFM imaging is limited to those that can satisfy the fairly stringent suitability requirements for sample preparation. Here, four adhesion methods are compared for *E. coli* in multiple buffers, to find the most reliable and efficient protocol.

## 3.2 Results

### 3.2.1 Experimental Set-up

For any immobilisation method to work reliably, extensive cleaning of glass coverslips was essential. Detailed methods can be found in Chapter 2. But briefly, coverslips were sonicated in SDS for 10 minutes, rinsed in mQ, then ethanol and dried in nitrogen, they were then plasma cleaned and the process repeated. Glass was then coated with one of the four treatments tested and exponential phase cells immobilised in various buffers. Adhesion of two strains of *E. coli* (MG1655 and BL21) was quantified by counting the total number of bacteria per unit area (360 x 240  $\mu\text{m}^2$ ) using brightfield microscopy. Dead cells were identified using epifluorescence with the nucleic-acid dye SYTOX™.

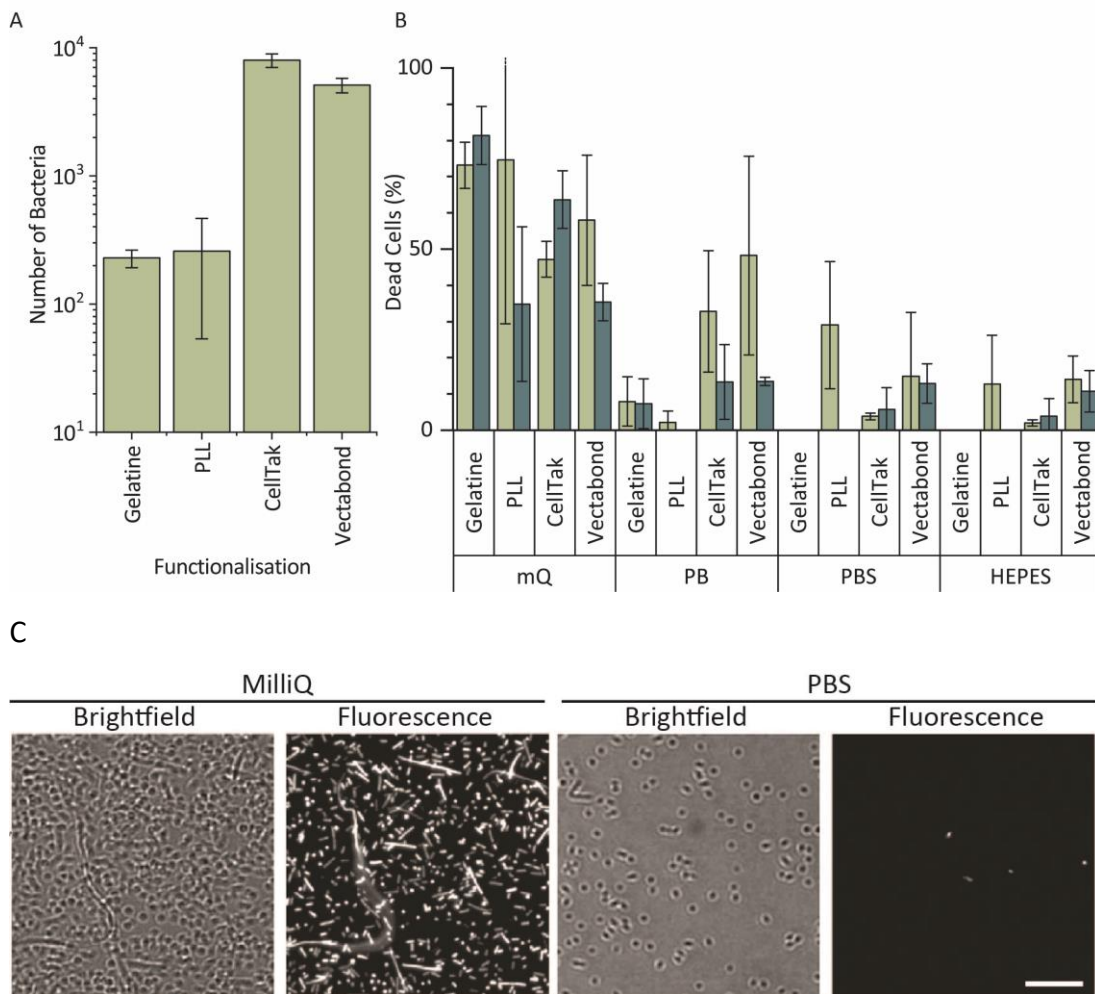


Figure 3.1. (A) Adhesion of BL21 *E. coli* in mQ water was high on all surfaces tested.  $N=3$ , where  $N$  is the number of independent experiments. (B) Percentage of dead cells immobilised onto glass shows mQ led to high levels of death in both strains. Death was lower when buffers were used, particularly HEPES buffer. Light green is BL21 and dark green is MG1655.  $N=3$ . (C) Representative brightfield and SYTOX™ stain images used for calculations of cell number and death in A-B. These emphasise that cells adhere more, but survive less, in mQ water compared to high salt buffers. Images are of BL21 cells on Vectabond®. Scale bar is 20  $\mu\text{m}$ .  $N=3$ , where  $N$  is the number of independent experiments.

Different immobilisation techniques and buffer conditions yield different levels of adhesion, so four methods were investigated. Gelatin and PLL were tested as they are the most common immobilisation methods<sup>134,136</sup>. These are cationic protein coatings that promote the attachment of negatively charged bacteria via

electrostatic interactions. Cell-Tak™ is an acidic solution of polyphenolic proteins purified from marine mussels. When neutralised with sodium bicarbonate, the proteins absorb onto a surface, coating a glass coverslip for bacteria to adhere<sup>137</sup>. Finally, Vectabond® is a solution predominantly made up of 3-Aminopropyltriethoxysilane (APTES)<sup>138</sup> which coats coverslips with amine groups and is believed to adhere bacteria via electrostatic and hydrophobic interactions<sup>134,139</sup>.

### 3.2.2 Cell Death is High in mQ and Gelatin is Ineffective

In mQ, all methods gave high adhesion (Figure 3.1A). However, cell death was also high on all surfaces. The use of buffers greatly reduced cell death and salts tended to improve survival further (Figure 3.1B-C). But, the effectiveness of coatings was greatly reduced in high salt buffers due to masking by monovalent ions<sup>134</sup>. For example, although gelatin worked well for both strains in PB, it was poor in HEPES and PBS (Figure 3.2). The effectiveness of immobilisation on gelatin is known to be affected by buffer composition<sup>115,134,136</sup>, which limits its scope for experiments carried out in solutions that better mimic physiological conditions. Preparation was also time consuming as air drying of coverslips took hours. This complicates the planning and design of AFM experiments, in particular those that require prolonged scanning. For these reasons, gelatin was not further considered.

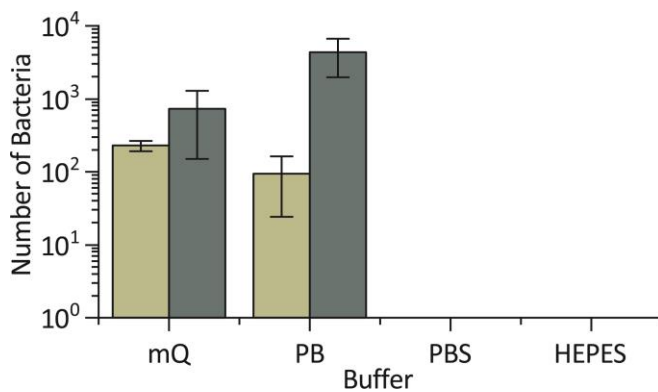


*Figure 3.2. Bacteria adhered to gelatin well when there was little salt. However, adhesion was abolished in physiological buffers for BL21 and MG1655 E. coli. Light green is BL21 and dark green is MG1655. N=3.*

### 3.2.3 PLL is Effective for BL21 E. coli

Surprisingly, adhesion was also greatly affected by bacterial strain. In particular, PLL only immobilised MG1655 bacteria in mQ, but worked effectively for BL21 *E. coli* in all conditions tested (Figure 3.3A). Although the reason for this was not investigated,

it was likely due to differences between the outer membrane structures of the two strains<sup>140</sup> and that MG1655 cells are more motile<sup>141</sup>. By AFM, BL21 cells in HEPES buffer were smooth and the stability of adhesion good enough to resolve nanoscale features (Figure 3.3B-C). PLL was also quick to prepare, making it suitable for the adhesion of BL21, particularly in complex experimental set ups.

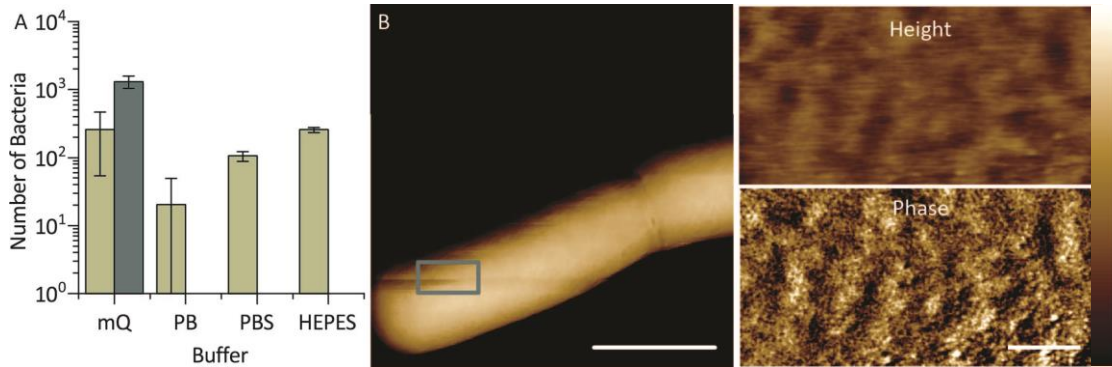


*Figure 3.3. (A) BL21 adhered well to PLL coated glass in all conditions tested, but MG1655 adhered only in mQ. Light green is BL21 and dark green is MG1655. (B) Phase image of a BL21 cell immobilised onto PLL in HEPES buffer. Cells are smooth and stably adhered. Green box gives location of smaller images on the right. Smaller, higher resolution height and phase images show nanoscale undulations and features on the surface. Colour bars are 10 deg, 5nm and 0.07 deg. Scale bars are 1 μm and 100 nm. N=3.*

### 3.2.4 Cell-Tak™ Led to Aggregates on Bacteria

On Cell-Tak™, adhesion was high in all conditions, supporting previous work showing good adhesion for a range of bacteria, even in nutrient broth<sup>134</sup> (Figure 3.4A). However, by AFM, unidentified aggregates ~15 nm high and ~75 nm wide were observed on both strains, making the samples unusable for high resolution studies (Figure 3.4B-C). It is worth noting that Cell-Tak™ has been used in previous studies<sup>53,134</sup>, without this problem of aggregates. Meyer et al. investigated several techniques to immobilise a variety of bacteria and recommend using Cell-Tak™ for immobilisation, achieving excellent adhesion of Gram-positive and -negative cells for several hours, even in nutrient broth<sup>134</sup>. However, the persistent appearance of contaminants in these experiments made the method less successful in our hands.

### 3.2.5 Vectabond® Provides Excellent Adhesion

Finally, adhesion of bacteria onto Vectabond®-coated coverslips was efficient in all conditions. Although Vectabond® predominantly consists of APTES, it has a proprietary composition. This may explain the contradictions between our results to previous data showing adhesion to APTES coated glass could only occur in deionised water<sup>134</sup>. The success of Vectabond® was of particular interest as the coating supported high levels of MG1655 adhesion in buffers (Figure 3.5A). AFM results show, cells were stably adhered, appeared smooth and had higher resolution (Figure 3.5C). Following the high adhesion of MG1655, the technique was tested further.

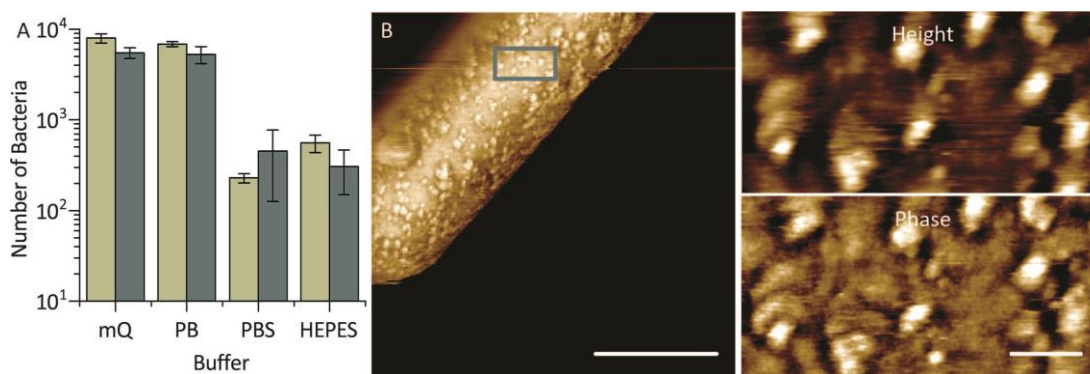


*Figure 3.4. (A) BL21 and MG1655 E. coli adhered well to Cell-Tak™ coated glass in all conditions tested. Light green is BL21 and dark green is MG1655. However, AFM shows large contaminants on the surface of bacteria. (B) Phase image of MG1655 cell immobilised onto Cell-Tak™ in HEPES buffer showing contaminants clearly. Green box gives location of right hand, higher resolution phase and height images. Colour bars are 6 deg, 10 nm and 1 deg. Scale bars are 1 μm and 100 nm. N=3.*

Since AFM can be time consuming, it is desirable to use conditions that keep cells as healthy as possible, preferably they will be metabolically active and dividing. Therefore, cells were immobilised in minimal media (MM) for 30 minutes. But this gave very poor adhesion. Nevertheless, it has previously been shown that cells immobilised in a low salt buffer and washed into media survived well<sup>136</sup>. So, a version of this method was tested as cells were immobilised in 20 mM HEPES for 5 minutes, then washed into MM. Cells adhered well (Figure 3.5A), and importantly, showed very low death (Figure 3.5B).

Under these conditions, cells remained adhered for long time periods and nanoscale features were easily imaged. Furthermore, the presence of glucose allowed cells to divide on the coverslip, proving the physiological relevance of these conditions (Figure 3.5D-E). The speed, efficiency and versatility of Vectabond® are perfect for AFM experiments, so this technique is highly recommended for AFM of live bacteria.

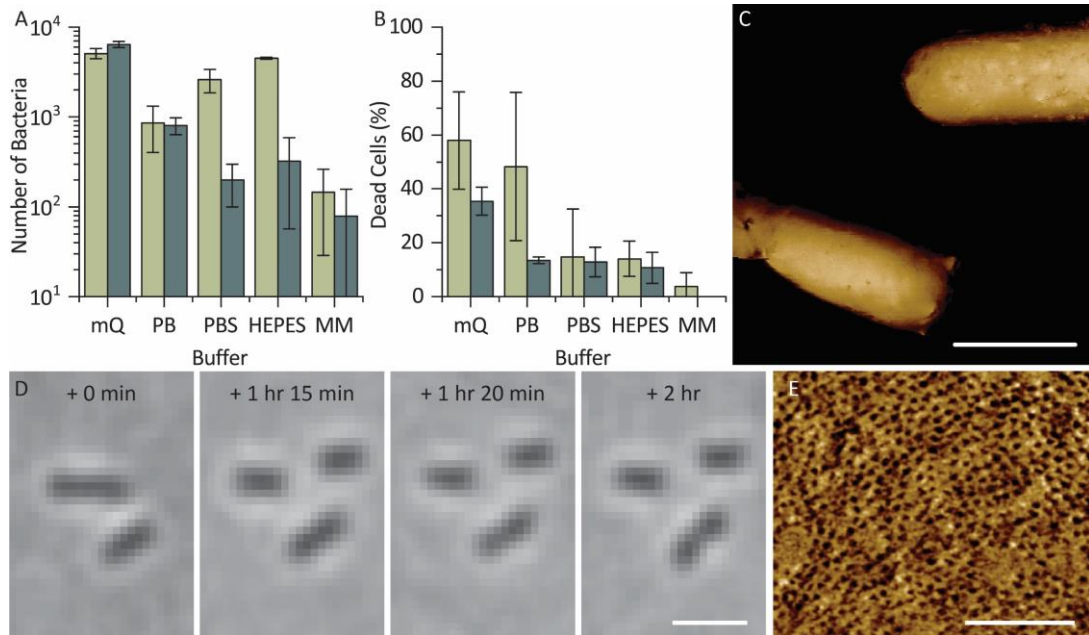


Figure 3.5. Vectabond® immobilisation (A) Both strains of *E. coli* adhere well to Vectabond® in all buffers, including MM. N=3. (B) Cell death is very low in MM, particularly for MG1655. Light green is BL21 and dark green is MG1655. N=3. (C) AFM shows MG1655 immobilised on Vectabond® in HEPES buffer are stably adhered. (D) Brightfield images over time show cells are dividing on coverslips in MM. (E) Phase image shows nanoscale features on the surface of MG1655 in MM. Colour bar is (C) 10 deg and (E) 1 deg. Scale bars are (C) 1  $\mu$ m (D) 3  $\mu$ m and (E) 100 nm.

### 3.3 Discussion

The immobilisation of living cells and organisms is vital for physiological AFM experiments; therefore, others have also tried to optimise protocols, but similar techniques are not always reproducible in different studies. Meyer et al. investigated several techniques to immobilise a variety of bacteria. They primarily recommended using Cell-Tak™ for immobilisation of Gram-positive and -negative cells<sup>134</sup>. However,

they did find lower adhesion of long rod shaped bacteria<sup>134</sup> and in our hands, it was unreliable and prone to contamination.

Meyer et al. also investigated covalently attaching cells to a substrate and achieved excellent adhesion, however, they pointed out that chemically modifying bacterial surfaces may affect validity of subsequent experiments<sup>134</sup>. They also tried physical entrapment of cells in microwells but find capture inefficient<sup>134</sup>. This is contrary to a study by Kailas et al. which uses star-shaped wells to trap *Staphylococcus aureus* with very high efficiency. The lack of chemical interactions required for immobilisation meant that experiments could be performed in complex growth media to track cell division<sup>87</sup>.

One of the most popular methods for immobilisation, gelatin, has the most reproducible pattern of adhesion: Meyer et al., Lonergan et al. and Allison et al. all find good adhesion in water or low salt buffers for a range of bacteria<sup>115,134,136</sup>. But, cell viability assays consistently find bacteria in these conditions have a high level of staining by dyes for cell death<sup>136</sup> and adhesion cannot be maintained in high salt buffers<sup>134,136</sup>.

As with gelatin, PLL coated glass adheres negatively charged bacteria via physisorption to the positively charged surface. Immobilisation of *E. coli* to PLL coated glass was extensively studied by Lonergan et al. They found that bacteria immobilised in minimal media were unsuitable for AFM imaging as cells detached. However, they found that immobilisation in dilute PBS supplemented with glucose and divalent cations led to efficient coverage of bacteria, cells could then be washed into nutrient media and maintain their adhesion. With this method they were able to track cell division by AFM.

This chapter adds to the body of existing literature on immobilisation strategies and investigates the differences in adhesion and cell viability as a function of buffer composition and bacterial strain. The outcome was two reliable methods (PLL for BL21 *E. coli* and Vectabond® for any *E. coli*) that were invaluable to the completion of this thesis and could be beneficial for future use of AFM in microbiology.

# Chapter 4

## OMP Organisation in the Outer Membrane

The OM protects Gram-negative bacteria against harsh environments and antimicrobials, including many antibiotics. It has a highly asymmetric structure, with an inner leaflet of phospholipids, an outer leaflet of lipopolysaccharide (LPS) and both leaflets are spanned by abundant proteins<sup>9,10</sup>. In this chapter, the organisation of outer membrane proteins (OMPs) is determined for live *E. coli* and the impact of specific proteins on this arrangement is investigated. The results reported here redefine the current view of the OM as containing specific protein islands<sup>27,38,142</sup>, finding the organisation is dominated by a mostly static network of trimeric porins. Preliminary results also show that porin network may be made more mobile by removing the abundant OmpA protein<sup>2</sup>.

### 4.1 Introduction

The exclusion of antibiotics from Gram-negative bacteria by the OM makes them more prone to resistance than Gram-positive bacteria<sup>10</sup>. As well as protection, the OM provides mechanical integrity<sup>143</sup> and allows selective diffusion of small molecules into the cell. It achieves these functions with an outer leaflet rich in LPS and outer membrane proteins (OMPs)<sup>2</sup>, which are relatively static<sup>32</sup>. This is thought to be due to promiscuous protein-protein interactions that lead to non-homogenous patterning of OMPs across the cell, predominantly into large islands<sup>27,32,38,44,45</sup>. OMP arrangement has been studied for specific, labelled proteins. However, OMPs are hugely diverse and can be present at 100,000s copies per cell<sup>28</sup>.

One of the most abundant of these is OmpA which has a small  $\beta$ -barrel in the OM and a periplasmic C-terminal domain capable of non-covalently binding the peptidoglycan<sup>26</sup>. There is also a second, more controversial conformation of OmpA where the periplasmic domain joins the N-terminus to form a larger OM  $\beta$ -barrel. In

model membranes, the formation of this larger barrel is irreversible and temperature dependent, mostly forming at physiological conditions<sup>144</sup>.

As well as an unclear structure, the exact function of OmpA is not understood, partly due to apparently multiple roles, including acting as an adhesin for host invasion, neutralising host defences and enhancing biofilm formation<sup>144</sup>. OmpA is also a slow porin, allowing diffusion of specific small molecules when in certain conformations<sup>145</sup>. At a cellular level, loss of *ompA* leads to some disruption of membrane integrity and increases sensitivity to further gene deletions. However, the single deletion of *ompA* does not affect cell growth<sup>146</sup>.

Although OmpA might have some role as a porin, the major porins of *E. coli* are trimeric. There are two predominant trimeric porins in *E. coli*: OmpF and OmpC. Others, such as LamB or PhoE, may be induced by the presence of their substrate, but are generally expressed at low levels<sup>2</sup>. OmpF and OmpC are 16-stranded  $\beta$ -barrels that form as homotrimers and allow the non-selective diffusion of small, polar molecules across the membrane<sup>2,147</sup>.

Despite the abundance of OmpA and trimeric porins, only low copy-number OMPs have been shown to form islands<sup>27,32,38,44,45</sup>. The arrangement of the most abundant OMPs is not known. In the following chapter, the organisation and diffusion of trimeric OMPs and a potential new role of OmpA are described. This is achieved by imaging live bacteria with AFM over large length scales and over time, with novel labelling strategies.

## 4.2 Results

### 4.2.1 Imaging Whole Cells at Nanometre Resolution

To resolve the supramolecular organisation of the unlabelled OM of live bacteria, exponential phase *E. coli* were immobilised onto Vectabond<sup>®</sup> coated glass coverslips and imaged by AFM in minimal media<sup>54</sup>. By AFM, cells had a smooth appearance at low magnification (Figure 4.1A). To obtain cell-wide, molecular-scale maps of the accessible OM, multiple higher-magnification scans were recorded and overlaid.

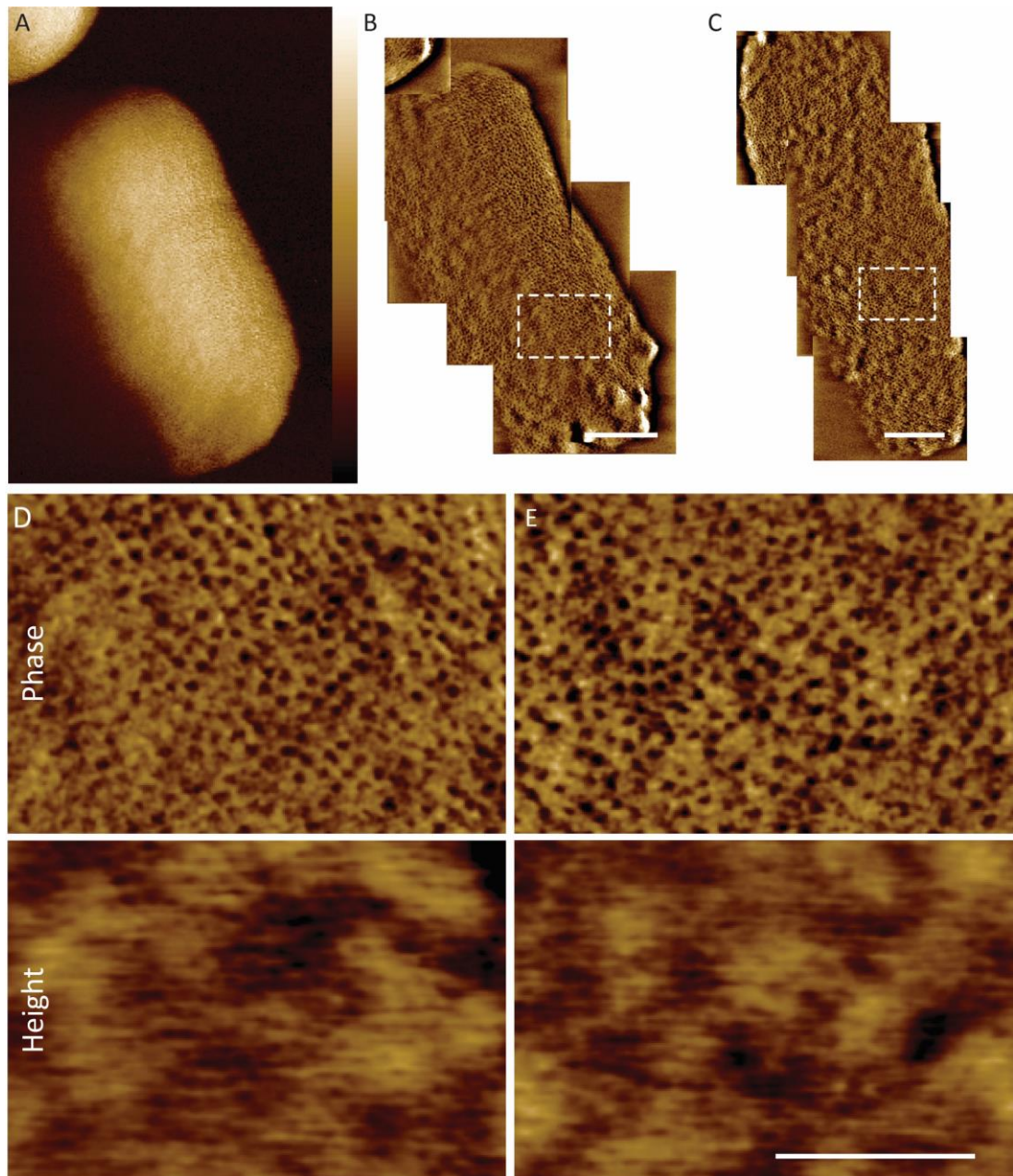


*Figure 4.1. E. coli are imaged at nanometre resolution by AFM. (A) Large AFM phase scan shows an entire MG1655 cell at low resolution. (B-C) Images of the nanoscale architecture of the entire OM can then be produced by superimposing small, high-resolution phase images. Once imaging is optimised, the entire surface may be mapped in 5-10 minutes. (B) MG1655 and (C) BW25113 E. coli both have membranes packed by pore-like structures. (D and E) Enlarged phase and height images, of the regions marked by the dashed boxes in B and C respectively, show  $\sim 8$  nm wide pores fill the membrane. Scale bars are (A-C) 500 nm and (D-E) 100 nm. Colour bars are (A) 7 deg, (B-C) 1.5 deg, (D-E) 1.5 deg and 5 nm.*

In these images, MG1655 *E. coli* surfaces were shown to contain a dense packing of pore-like structures, superposed to a background with 2-5 nm height variations over ~50 nm (Figure 4.1B and D). This was also confirmed in a second strain of *E. coli* (Figure 4.1C and E). On a small scale, the observed pore-like structures are consistent with AFM experiments on various Gram-negative bacteria<sup>37,52–54</sup> and, at cellular length scales, with electron microscopy data on freeze-fractured bacteria<sup>46,49–51,148</sup>. They also resemble arrangements of packed trimeric porins observed by AFM on isolated OMs<sup>47</sup>.

#### 4.2.2 *E. coli* Cells are Covered in a Network of Trimeric Porins

To identify the pore-like structures, each pore was localised. This was done on overlaid images of whole cells (Figure 4.1B-C) using a machine learning model trained on manually found pores, built by Joel Forster<sup>‡</sup> and described in Chapter 2. The resulting pore coordinates were used to quantify pore packing. On both strains, the nearest-neighbour distance (~9 nm) and the angular distribution of near neighbours (peaked just below 60°; Figure 4.2A-B) was consistent with the hexagonal lattices of porin trimers reconstituted in lipid membranes<sup>9,149–153</sup>, with one pore-like structure for each trimer. The ~8 nm diameter of observed pore-like structures also fits well with the dimensions of crystal structures of trimeric porins<sup>154</sup>. These data suggest the pore network may be attributed to trimeric porins.

This interpretation was confirmed by modulation of the expression of the most abundant trimeric porins, OmpF and OmpC, via the removal and reintroduction of their transcriptional activator, OmpR<sup>155</sup>, into MG1655<sup>§</sup>. By AFM, the number of pores per  $\mu\text{m}^2$  correlated with the expression of OmpF and OmpC (Figure 4.2D-E). Similar results were obtained for a second strain, in which deletion of trimeric porins OmpF, OmpC and LamB led to the absence of all pore features in the AFM images (Figure 4.2F), confirming that each pore corresponds to a trimer of porins.

---

<sup>‡</sup> Department of Physics and Astronomy, University College London, WC1E 6BT London, UK

<sup>§</sup> Construction of strains and validation of expression levels was performed by Dr Irina Mikheyeva-Bridges (Department of Molecular Biology, Princeton University, Princeton, New Jersey, USA)

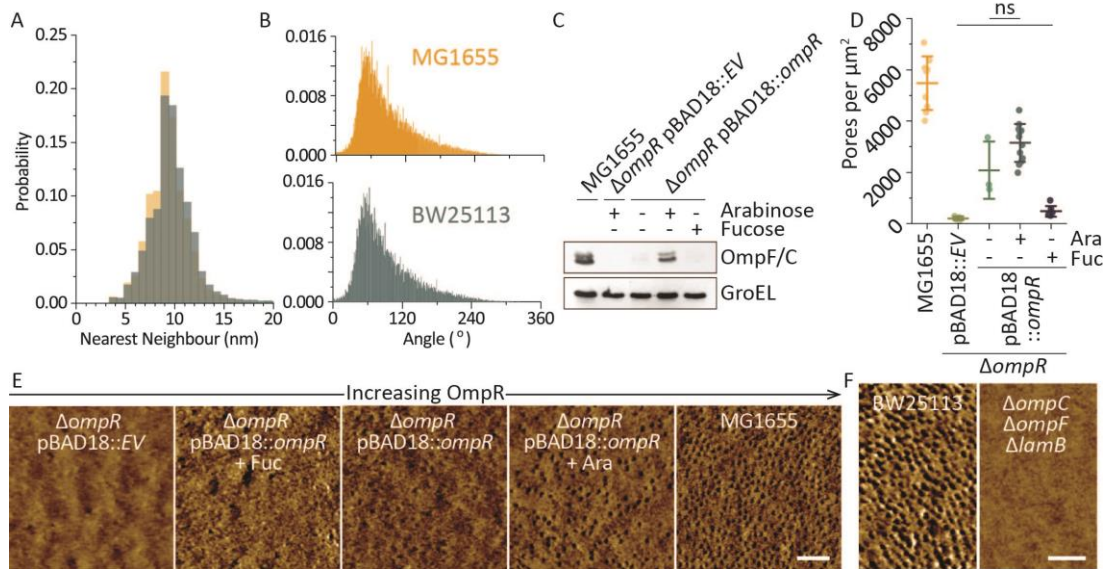


**Figure 4.2.** (A) Nearest neighbour and (B) angular distributions for pores in MG1655 and BW25113 showing that, in both strains, the pores are separated from their nearest neighbour by  $\sim 9$  nm; and that the angular distribution of near neighbours (up to a distance of 15 nm) peaks at just below  $60^\circ$ , indicative of a hexagonal lattice. MG1655 data is from 32,669 pores across 9 cells and BW25113 data is from 10,536 across 4 cells. (C) Western blot showing variation in the levels of expression of OmpF and OmpC by the removal of OmpR and its reintroduction on an inducible plasmid to MG1655\*\*. (D) Number of pore-like structures per  $\mu\text{m}^2$  detected in AFM images showing a variation consistent with the OmpF and OmpC expression in C. Each data point corresponds to one cell with at least three independent experiments for each condition (E) Typical phase images used for quantification in D. (F) Removal of three major trimeric porins (OmpC, OmpF, LamB) also abolishes pore-like structures. BW25113 pores are shown for comparison. Scale bars are 50 nm. Colour bars are (E) 2 deg, 1 deg, 1 deg, 2 deg and 2 deg and (F) 0.75 deg. ns =  $p > 0.05$ , all other pairs have  $p < 0.05$ .

### 4.2.3 Trimeric Porins are Close to Stationary

The slow diffusion of proteins in the OM has been shown for various OMPs. Here, and in line with previous AFM analyses<sup>37</sup>, the diffusion coefficients of trimers was

\*\* Data provided by Dr Irina Mikheyeva-Bridges (Department of Molecular Biology, Princeton University, Princeton, New Jersey, USA)

low, with a median of  $2 \times 10^{-7} \mu\text{m}^2 \text{s}^{-1}$  (Figure 4.3A). Single-molecule fluorescence analysis of labelled OMPs consistently yields higher diffusion coefficients on live cells, likely because the actual diffusion is below the noise-floor of fluorescence microscopy<sup>25,36,38</sup>.

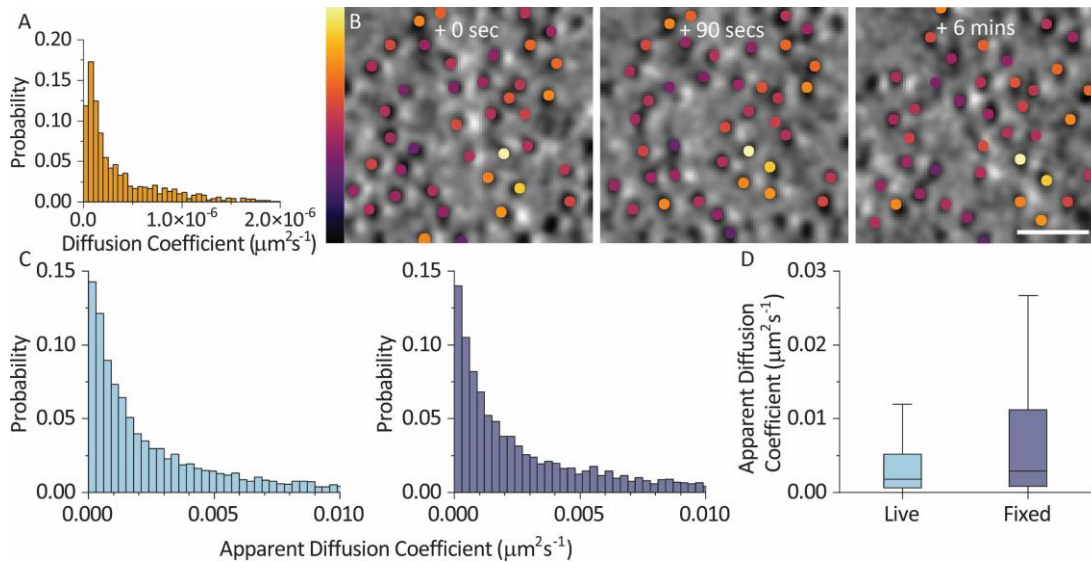


*Figure 4.3. Diffusion of pores in the membrane is slow. (A) Distribution of diffusion coefficients, showing that pores are diffusing with a median of  $2 \times 10^{-7} \mu\text{m}^2 \text{s}^{-1}$  ( $n = 90$ ). Diffusion was measured by manually labelling pores in subsequent images<sup>††</sup>. (B) Grayscale phase images with porin locations as a function of time, shown in colours corresponding to the overall diffusion of each pore. After 90 seconds and after 6 minutes, the pores maintain their approximate layout. Colour scale is 0 to  $0.00008 \mu\text{m}^2 \text{s}^{-1}$ . Scale bar is 25 nm. (C) Live and fixed MG1655 single particle tracking of ColN<sup>1-185</sup>PAmCherry labelled OmpF. Left: Diffusion coefficient histograms of OmpF in live MG1655 (blue;  $n = 6,829$ ) and 4% formaldehyde fixed MG1655 (purple;  $n = 5,956$ ). Histograms have been cropped after  $0.01 \mu\text{m}^2 \text{s}^{-1}$ . (D) Box plots of apparent diffusion coefficients from single particle tracking of OmpF in live MG1655 (blue) and fixed MG1655 (purple)<sup>††</sup>.*

<sup>††</sup> Calculated by Dr Nikola Ojic (Department of Physics and Astronomy, University College London, WC1E 6BT London, UK).

<sup>††</sup> Experiments and analysis were performed by Patrick Inns (Department of Biochemistry, South Parks Road, University of Oxford, Oxford OX1 3QU, UK).

However, single particle tracking<sup>§§</sup> (SPT) showed that the measured diffusion of OmpF in live cells is not significantly higher than on fixed cells, indicating that within the resolution of SPT, OMPs are essentially static (Figure 4.3C-D). Indeed, the approximate position of trimers, measured by AFM, was comparable over minutes (Figure 4.3B). The stability of porins in a liquid crystal-like state is striking and brings together *in vivo* and *in vitro* evidence of protein networks<sup>36,38,39,49,156</sup>. However, the ubiquity of the lattice over the entire cell is surprising, particularly given previous evidence that areas of the OM can be enriched in various proteins<sup>32,40–43</sup>.

#### 4.2.4 OmpA is Distributed Within the Network

Since trimeric porins were found to fill most of the OM, the location of another abundant protein, OmpA, was considered. As a monomeric OMP, OmpA is below the resolution of these images. Therefore, to localise the protein, *E. coli* MG1655 cells expressing *ompA* with a streptavidin-binding peptide in an outer loop, were used<sup>114</sup>. Streptavidin was added to immobilised cells and height images used to find the ~5 nm diameter labels (Figure 4.4A). This showed that, like trimeric porins, OmpA was found throughout the OM with no obvious clustering (Figure 4.4B).

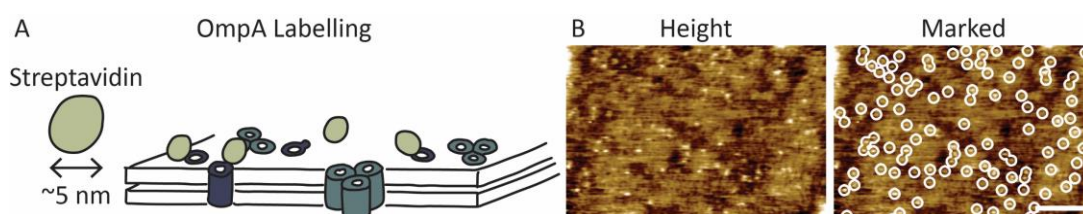


Figure 4.4. (A) OmpA is labelled by expressing *ompA* with a streptavidin binding peptide in an outer loop and adding streptavidin. (B) Streptavidin is clearly visible in height images, qualitatively showing no clustering of OmpA or localisation to distinct regions of the cell. Scale bar is 100 nm. Colour bar is 5 nm.

The lack of clustering of OmpA is, again, contrary to previously observed protein islands. Furthermore, the presence of OmpA within the trimeric lattice suggests some interaction between OmpA and trimers is unavoidable. This is supported by evidence of non-specific protein-protein interactions between OMPs<sup>32,36,38,142</sup>.

---

<sup>§§</sup> From Patrick Inns (Department of Biochemistry, South Parks Road, University of Oxford, Oxford OX1 3QU, UK).

#### 4.2.5 Removing *ompA* Perturbs the Trimeric Porin Network

So far, the distribution of OmpA and trimeric porins across cells has been established. Since OmpA is embedded in the protein network, the impact of OmpA on the trimeric lattice was assessed by removing *ompA* from MG1655. This, preliminary, data is presented in the following sections.

Removal of *ompA* perturbed the OM in two ways: the lattice appeared to be abolished and large plateaus were seen on some cells (Figure 4.5A-D). The plateaus were not always present, but could cover much of the surface (Figure 4.5C). They also protruded by approximately  $\sim 1$  nm and closely resembled those seen by freeze-fracture electron microscopy after *E. coli* were treated by EDTA<sup>46</sup>, suggesting they may be due to a stress response from an unstable membrane.

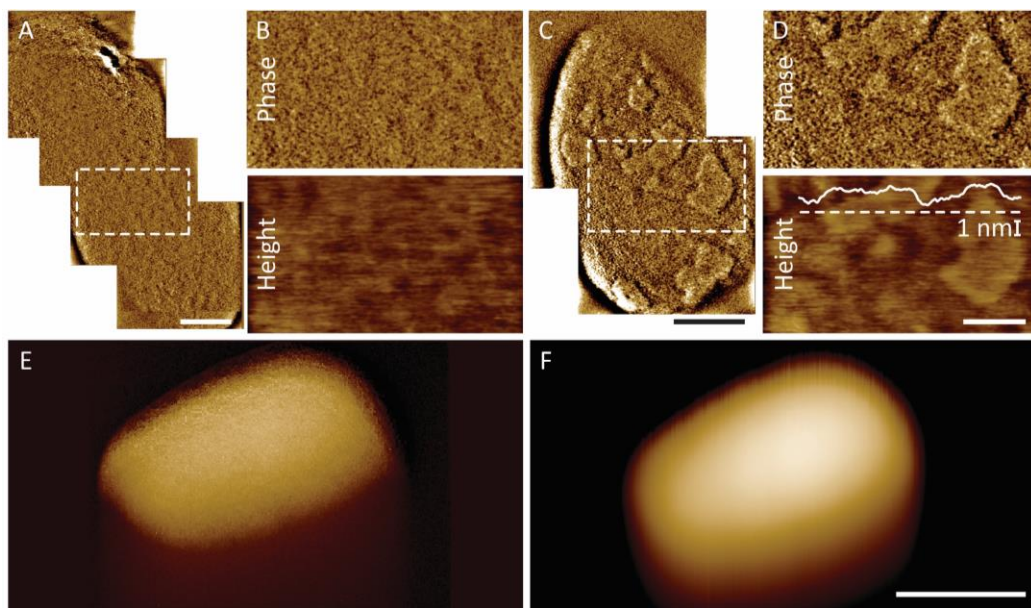
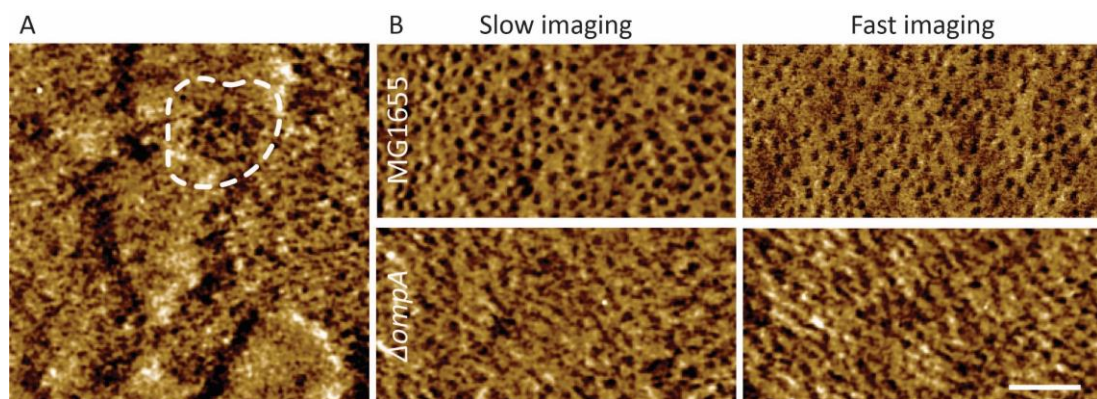


Figure 4.5. Without *ompA*, OM morphology is disrupted. (A) The porin lattice is indistinct over the entire surface of the cell. Dashed box shows the location of B. (B) Neither the phase or height show clear pores. (C)  $\Delta ompA$  cell OMs can have large plateaus. The dashed box shows the location of D. (D) Phase and height images, with a height profile along the dashed line, show plateaus protrude by  $\sim 1$  nm. (E) Phase and (F) height images of an  $\Delta ompA$  cell show the membrane is stable at the whole cell level. Scale bars are (A and C) 200 nm, (B and D) 100 nm and (F) 1  $\mu$ m. Colour bars are (A-D) 0.5 deg and 5 nm, (E) 10 deg and (F) 300 nm.

The most surprising feature of  $\Delta ompA$  cells was the apparent absence or only vague presence of pore-like structures in the AFM imaging (Figure 4.5A-B). The removal of *ompA* has not previously been reported to reduce trimeric porin expression, so it seemed unlikely that this was the reason for a lack of trimers by AFM. Since AFM is a surface scanning technique that physically interacts with the surface, the apparent absence of pore-like structures may have been due to changes in the properties of the membrane.

Of the many reasons for a lack of contrast in AFM, a soft or unstable surface seemed most likely. Indeed, the stiffness of  $\Delta ompA$  cells has previously been shown to be much lower than wild type<sup>143</sup>. This could lead to an undulating membrane as has been seen in AFM of cells with decreasing stiffness<sup>16</sup>. However, the lack of contrast does not seem to act at a cellular level; images of whole cells at low resolution look no different to wild type (Figure 4.5E-F). Therefore, the softness of  $\Delta ompA$  cells also seemed an unlikely reason for the absence of pore-like structures.



*Figure 4.6. Pore-like structures are present in the  $\Delta ompA$  OM, but they are harder to image, presumably due to instability in the membrane. (A) Close to plateaus, pores appear more clearly (highlighted by dashed line). Potentially, pore movement is restricted by the membrane defects. (B) A typical tip velocity of  $5 \mu\text{m s}^{-1}$  (left) and a faster,  $12 \mu\text{m s}^{-1}$ , tip velocity (right) shows little difference in wild type (MG1655) cells. But, when the same region of  $\Delta ompA$  cells is images at faster, some improvement in contrast occurs. Scale bar is 50 nm. Colour bar is (A) 0.8 deg and (B) top panel, 1 deg, 2 deg and bottom panel, 0.8 deg.*

Another explanation for the lower resolution of AFM images could be that, rather than a cell-wide instability, features were rapidly diffusing or more loosely packed, leading to local instability of individual pores<sup>157</sup>. With this in mind and by closer inspection of AFM images, pore-like structures were sometimes seen, particularly next to plateaus, albeit less clearly than on wild type (WT) cells (Figure 4.6A). This proved that pores were present in the membrane, but were much harder to image. To investigate whether this was because pores were less stable in the membrane, smaller scans were performed at higher scan rates. Higher scan rates give two advantages for imaging rapidly diffusing particles. The faster the tip moves to the next line, the more likely it is to catch the particle; and the higher the tip velocity, the lower the force exerted on the sample, so the less likely an unstable particle is to be knocked out of the way<sup>77</sup>. Increasing tip velocity led to slightly better contrast in phase images (Figure 4.6B).

#### 4.2.6 Removal of *ompA* Increases Trimer Diffusion

Imaging quality pointed towards an increase in trimer diffusion in  $\Delta ompA$  cells. The long-range diffusion of OmpA when the periplasmic domain is missing has previously been measured as the same as WT using fluorescence recovery after photobleaching (FRAP)<sup>34</sup>. This technique has also been used to show OmpF is very static<sup>116</sup>. However, FRAP does not have the single nanometre resolution of AFM, nor can it be performed for long time periods due to restrictions from photobleaching. With this in mind, the diffusion of OmpF was assessed by AFM.

With individual pores difficult to make out, tracking all single trimers of  $\Delta ompA$  cells was impossible. Therefore, to reduce the number of particles for tracking and to improve visualisation, OmpF was labelled. This was done using colicin N<sup>1-185</sup>mCherry (Figure 4.7A)<sup>\*\*\*</sup>. Colicin N is a naturally occurring antimicrobial peptide that translocates through OmpF and forms pores in the inner membrane. By replacing the pore forming domain with mCherry, Colicin N still binds to and partly translocates

---

<sup>\*\*\*</sup> Labels were developed for fluorescence microscopy by the Kleanthous group and provided by Patrick Inns (Department of Biochemistry, South Parks Road, University of Oxford, Oxford OX1 3QU, UK).

through OmpF, and remains stably bound within the porin with mCherry remaining on the outside of the OM<sup>116</sup>. Since mCherry is a globular protein with a diameter of  $\sim 3.5$  nm<sup>158</sup>, like streptavidin, it is readily detectable via protrusions in AFM height images (Figure 4.7B).

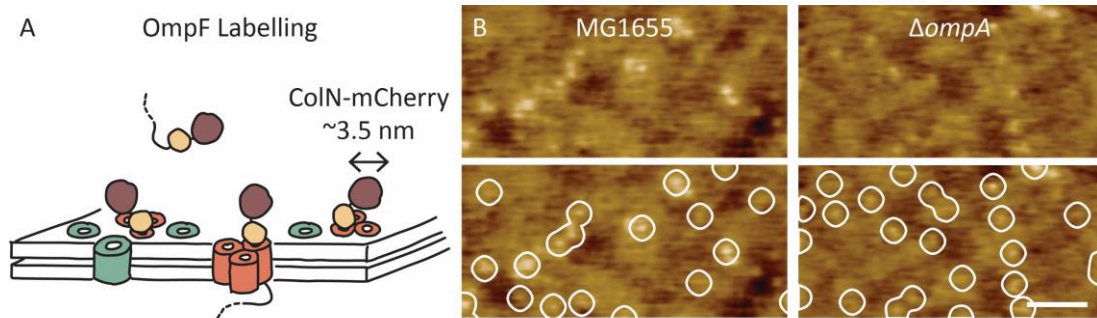


Figure 4.7. Colicin  $N^{1-185}$ mCherry is used to label OmpF trimers. (A) Schematic of OmpF labelling by colicin  $N^{1-185}$ mCherry. (B) Height images show labels clearly in WT and  $\Delta ompA$  cells. Bottom panel shows the height image with labels marked by white circles and detected by 0.5 nm maxima. Scale bar is 50 nm. Colour bar is 4 nm.

The low throughput nature of AFM meant that calculation of accurate diffusion coefficients was beyond the scope of this thesis. But qualitative analysis was still informative. In WT cells, OmpF labels were found to be static for tens of minutes (Figure 4.8A). However, OmpF appeared to diffuse faster without OmpA: time-lapse imaging at 25 seconds per frame found stable labels in WT whereas, qualitatively, in  $\Delta ompA$  cells, labels diffused tens of nanometres in minutes (Figure 4.8B-C).

## 4.3 Discussion

The observed crowded and static nature of this trimeric porin network is remarkable in the context of previously observed mesoscale rearrangements of protein islands that are enriched in particular OMPs during growth and division<sup>25,27,36,38</sup>. That the diffusion of OMPs should be low is expected as previous work has shown very low long-range diffusions and unusually low diffusion constants<sup>32</sup>. However, the measured diffusions of trimers here is orders of magnitude lower than previously recorded fluorescence measurements. This difference may be explained by the limits of SPT for small differences in diffusions: reflected by the observation that diffusion

constants from SPT<sup>25,36,38</sup> are consistently higher than by AFM<sup>37</sup>, suggesting OMP diffusion is at the limit of SPT resolutions. Further evidence of this is shown by fixation of *E. coli* in formaldehyde. Here, there would be no expectation of OMP diffusion due to cross-linking, but diffusion constants measured by SPT were, in fact, higher than on live cells.

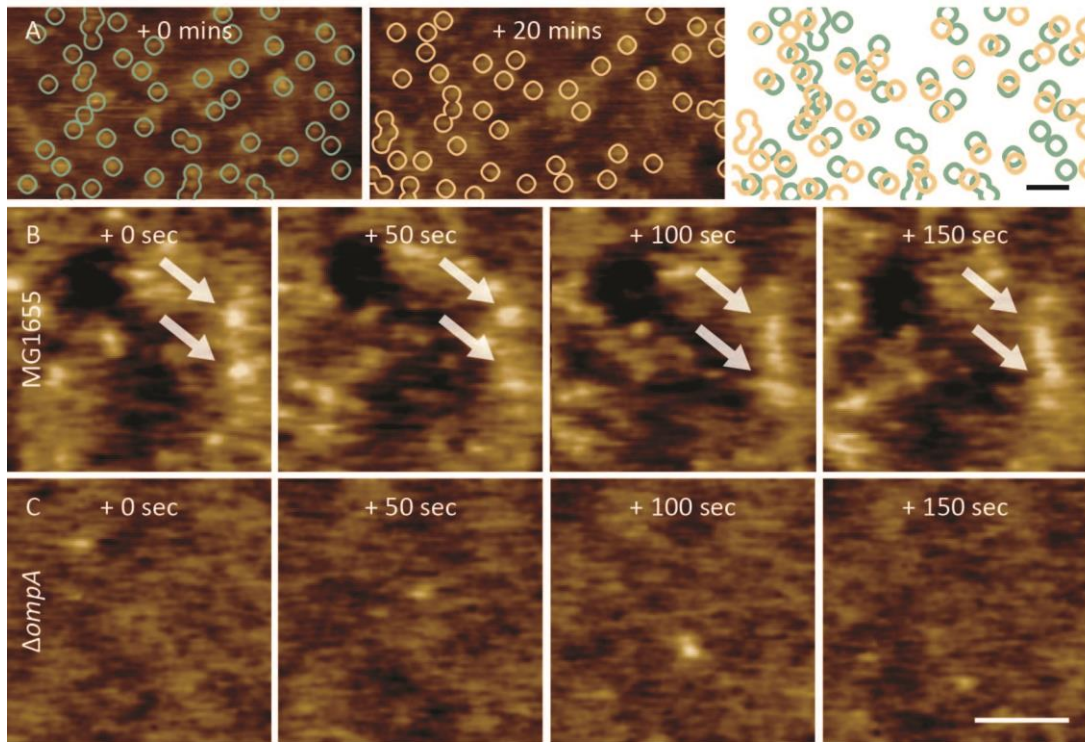


*Figure 4.8. (A) OmpF labelled BW25113 cells with labels marked by 0.5 nm maxima and shown by circles. The images in A are taken 20 minutes apart and the approximate location of labels is remarkably stable, highlighted by the overlay, right. Green circles are from 0 minutes and yellow from 20 minutes. (B-C) Height images from time-lapse imaging of OmpF labelled WT MG1655 and  $\Delta ompA$  cells. In WT, OmpF can locally move but maintains approximate locations over minutes, two examples are highlighted by white arrows. Without OmpA, OmpF diffuses over tens of nanometres in minutes. Scale bars are 50 nm. Colour bars are (A) 5 nm and (B-C) 2.5 nm.*

This high sensitivity to diffusion by AFM allowed the potential distinction of a previously unobserved effect of *ompA* deletions, in preliminary experiments. Pending validation by quantification and further experiments, the diffusion of OmpF in  $\Delta ompA$  cells would be a striking departure from the usually very stable pore

network. But the increase in diffusion, compared to OmpF in wild type cells, is still within the error of SPT and FRAP, thus AFM is essential for the measurement of OMP diffusions. The potential role of OmpA in the control of order in the OM is surprising and opens many questions. Whether this role is due to its ability to bind the peptidoglycan, due to its abundance, or extensive PPIs, is yet to be determined. But, if the latter is the case, it would also be interesting to test if other abundant OMPs have similar effects and whether the upregulation of low copy number OMPs rescues this phenotype.

The combination of mutations with novel labelling techniques, for AFM, has produced evidence for a new role of OmpA. Additionally, the use of high-resolution AFM on live *E. coli* has provided unexpected context to previous observations of island-like supramolecular arrangements.

# Chapter 5

## Phase Separation and Reorganisation in the Outer Membrane of Live and Dividing Cells

The asymmetry of the outer membrane bilayer is unusual and essential for its role in cellular protection. Phospholipids are kept to the inner leaflet to avoid compromising the barrier<sup>18</sup> and the lipid of the outer leaflet is lipopolysaccharide (LPS). Because of technical limitations in resolving molecular organisation of the outer membrane, little is understood about how LPS and phospholipids are arranged relative to OMPs. Here, the characterisation of smooth LPS-enriched patches within the near-static OMP network is described. The patches are shown to behave as liquid phases: growing during cell elongation and merging with other patches. In addition, when phospholipids are mislocalised to the outer leaflet, the membrane is found to be deformed by the presence of different patches, rather than an expansion of LPS patches. Finally, when cells divide, the outer membrane is found to show extensive surface ruffling at the division site.

### 5.1 Introduction

In the previous chapter, the *E. coli* outer membrane (OM) was revealed to be tightly packed with a heterogenous, near-static protein network. However, low copy number OMPs are often organised in islands and, while some proteins gradually move to cell poles as they age, others are localised at the poles, or flow in the opposite direction<sup>32</sup>. Further complicating this arrangement is the presence of LPS. With a similarly slow diffusion to OMPs, LPS potentially forms helically arranged islands<sup>40</sup> and is known to interact extensively with OMPs via unique binding patterns<sup>159,160</sup>, suggesting LPS is embedded in the protein network. On the other hand, LPS-LPS interactions are very strong and their existence in a liquid-crystalline

arrangement has been shown to be essential for antibiotic resistance<sup>156</sup>. How the LPS is arranged relative to OMPs remains a major question in OM architecture.

As well as binding LPS, some OMPs may pull specific lipids to their surface, as shown by computational modelling: for example, OmpF showed a preference for binding shorter tailed lipids<sup>161</sup>. Although phospholipids are kept to the inner leaflet under normal conditions, genetic or environmental factors can lead to their mislocation to the outer leaflet, leading to the sensitisation of cells to antibiotics that healthy *E. coli* would normally resist<sup>18</sup>. Similar to the case for LPS, it is not known how outer leaflet phospholipids are arranged in the OM.

A further question prompted by the ubiquitous OMP network is how the OM accommodates the molecular rearrangements that are required to facilitate cellular-scale growth and division. Indeed, how the OM is arranged and constricted at the division site is poorly understood. It is known that various peptidoglycan-anchoring OMPs and lipoproteins (e.g. Lpp and OmpA<sup>162</sup>) are important. More recently, the role of the Tol-Pal system for pulling the OM down with the constricting peptidoglycan and inner membrane has also been shown<sup>163</sup>. However, this still leaves the question of how the OM behaves – in particular given its molecular immobility (see Chapter 4) – as it is pulled inward.

In this chapter, the ability of AFM to gain nanometre to micrometre resolution is exploited to find large ruffles at the division site. But first, nanometre resolution images of live, dividing cells, over time are used to show that phase separation is a common feature in the OM, as demonstrated by the presence of patches enriched in LPS and, when inner-outer leaflet asymmetry is perturbed, separate patches of phospholipids.

## 5.2 Results

### 5.2.1 Smooth Patches Disrupt the Porin Network

Since membrane growth implies substantial supramolecular rearrangement and the ready formation of defects, flaws would be expected in the porin lattice. By imaging

the whole cell, sparse, pore-free, smooth patches were revealed, protruding by  $\sim 0.5$  nm above the trimeric network (Figure 5.1A-B). The patches were  $\sim 25$ - $225$  nm wide, with a mean diameter of  $55$  nm ( $\pm 30$ ,  $n=180$ ), and found on all cells. These observations are similar to early freeze-fracture electron microscopy images<sup>46,49,50,148</sup>, where occasional smooth patches were seen, particularly in the inner membrane. In the data presented here, patches were consistently observed on live and dividing bacteria (Figure 5.1C).

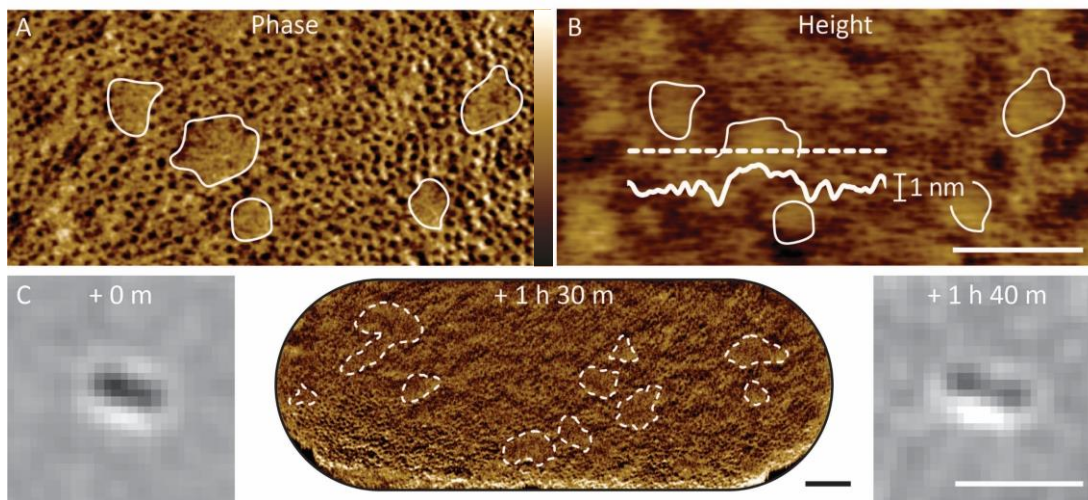


*Figure 5.1. Distinct pore-free patches can be seen within the trimeric porin network. (A) AFM phase image with patches highlighted by white lines. (B) Height image of the same area, showing that the patches protrude by  $\sim 0.5$  nm. These regions are also extremely smooth, with height variations of less than  $0.5$  nm. (C) Patches are features of dividing cells. Brightfield images are before and after acquisition of shown AFM phase image. Scale bars are (B)  $100$  nm and (C)  $100$  nm and  $5$   $\mu$ m. Colour bars are (A)  $1.5$  deg, (B)  $5$  nm and (C)  $0.7$  deg.*

### 5.2.2 Patches and Pore Networks Behave as Liquid Phases

A further observation from imaging patches over time, was that patches were seen behaving as liquid phases in the membrane: merging, growing and splitting apart over long time periods, but maintaining their approximate lateral positions at the bacterial surface (Figure 5.2). Combined with the distinct, separate appearance of the patches, this establishes the patches as liquid (presumably rather viscous) phases

that are separated from the trimeric porin network. To determine why these phases were occurring and their potential role in the OM, their composition was examined.

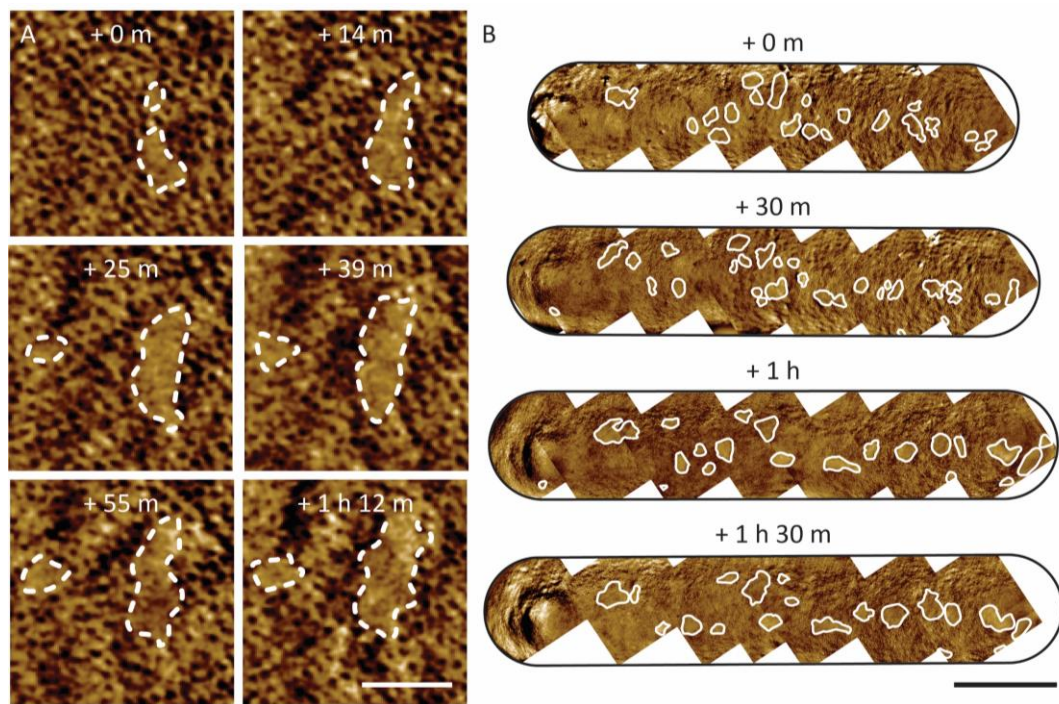


*Figure 5.2. Patches behave as phase separated regions of the membrane. (A) At time scales consistent with cell division, under these experimental conditions, patches merge, grow and split. (B) Although the patches are fluid, their relative locations on the cell change little. Scale bars are (A) 50 nm and (B) 500 nm. Colour bars are (A) 1.5 deg and (B) 2 deg.*

### 5.2.3 Patches are Depleted of Abundant OMPs

The lack of pore-like structures in smooth OM patches suggested they have a low protein content. So, to verify this, two abundant proteins were labelled: OmpF and OmpA. OmpF trimers were labelled by colicin N<sup>1-185</sup>mCherry<sup>116</sup> and OmpA by streptavidin<sup>114</sup> (see Chapter 4). Labels are distinguishable as local maxima in the AFM height images (see Chapter 2, section 2.3.3), but leave the patches harder to identify in the height images; by contrast, the patches are easily distinguished in the AFM phase images, but the labels not. This allowed the independent, unbiased detection of labels in the height channel, by a peak finding function, and of patches in the phase images, by manually marking (Figure 5.3A).

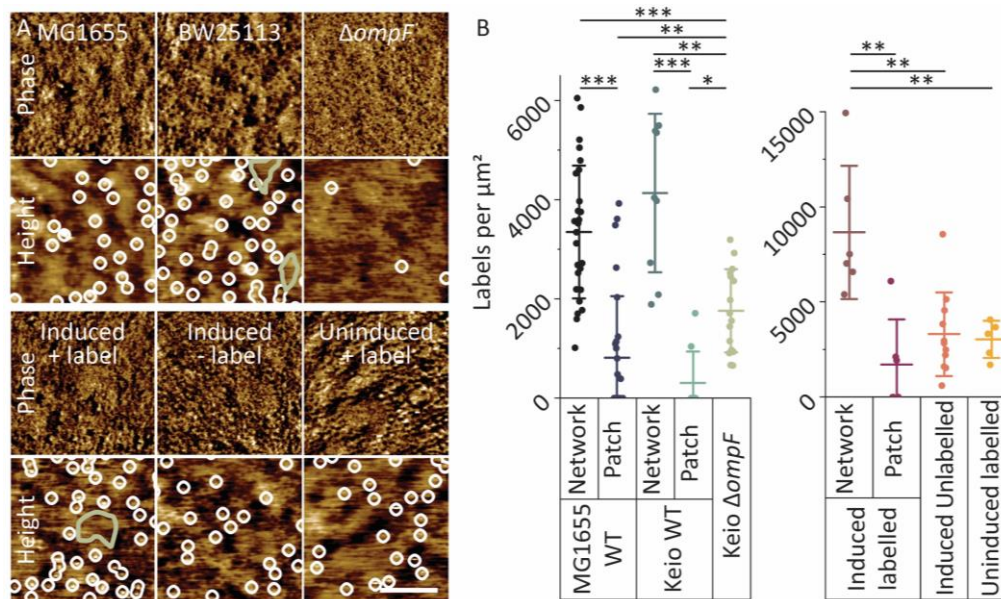


Figure 5.3. Colicin  $N^{1-185}mCherry$  and streptavidin labelling of OmpF and OmpA, respectively. (A) Phase and height images of MG1655 (WT), BW25113 (keio WT) and JW0912-1 ( $\Delta ompF$ ) cells with Colicin  $N^{1-185}mCherry$  labelling; and MG1655 pGV28 OmpA-SA1 induced by IPTG with and without streptavidin labelling, and non-induced with streptavidin labelling. Labelling is efficient in both WT strains and induced cells. No labels are seen in negative controls, although the detection technique picks up some false positives. Green shapes show marked patches and white circles show labels detected. (B) Left, OmpF labels per  $\mu m^2$  in the patch regions and pore networks of WT cells, and average of the whole surface of JW0912-1 cells. Right, OmpA labels per  $\mu m^2$  in the patch regions and pore networks of induced, labelled cells and the overall surface of induced unlabelled and uninduced cells. Each data point corresponds to a single image, in which images were recorded from three independent experiments with at least one cell per experiment. Scale bar is 100 nm. Colour bars are 3 nm. Vertical phase scales are 0.5 deg, 1.1 deg, 0.3 deg, 0.2 deg, 0.3 deg, and 0.75 deg. \* =  $p < 0.05$ , \*\* =  $p < 10^{-2}$  and \*\*\* =  $p < 10^{-4}$  from student's t-test.

With this method, both OmpF and OmpA were found to be excluded from patches. For OmpF, the two wild type strains inspected gave a mean of 3350 ( $\pm 1341$ ) and 4134 ( $\pm 1599$ ) labels per  $\mu m^2$  in the network regions. Compared to only 810 ( $\pm 1242$ ) and 307 ( $\pm 625$ ) labels per  $\mu m^2$  in the patches: lower than the noise floor due to false positives, shown by the detection of 1755 ( $\pm 839$ ) labels per  $\mu m^2$  in cells lacking OmpF

(Figure 5.3B). Similarly, streptavidin localised to the porin network of OmpA-SA1 cells with a density of 8654 ( $\pm$  3503) labels per  $\mu\text{m}^2$ , as opposed to 1695 ( $\pm$  2380) labels per  $\mu\text{m}^2$  in the patches, not significantly different to the detection of false positives on induced unlabelled cells (3025 ( $\pm$  985) labels per  $\mu\text{m}^2$ ) or uninduced labelled cells (3304 ( $\pm$  2200) labels per  $\mu\text{m}^2$ ; Figure 5.3B). The lack of abundant proteins in the patches suggests that patches are largely, if not totally, free of protein.

This conclusion is further supported by the observation of smoother, presumably protein-free patches against a rougher background in cells without OmpF and OmpC (Chapter 4), with the roughness of the background assumed to be due to other OMPs (Figure 5.4). Taken together, the data suggests the existence of distinct nanoscale, protein-poor domains that are phase-separated from densely packed proteinaceous areas in the OM, and gradually change over the cell cycle.

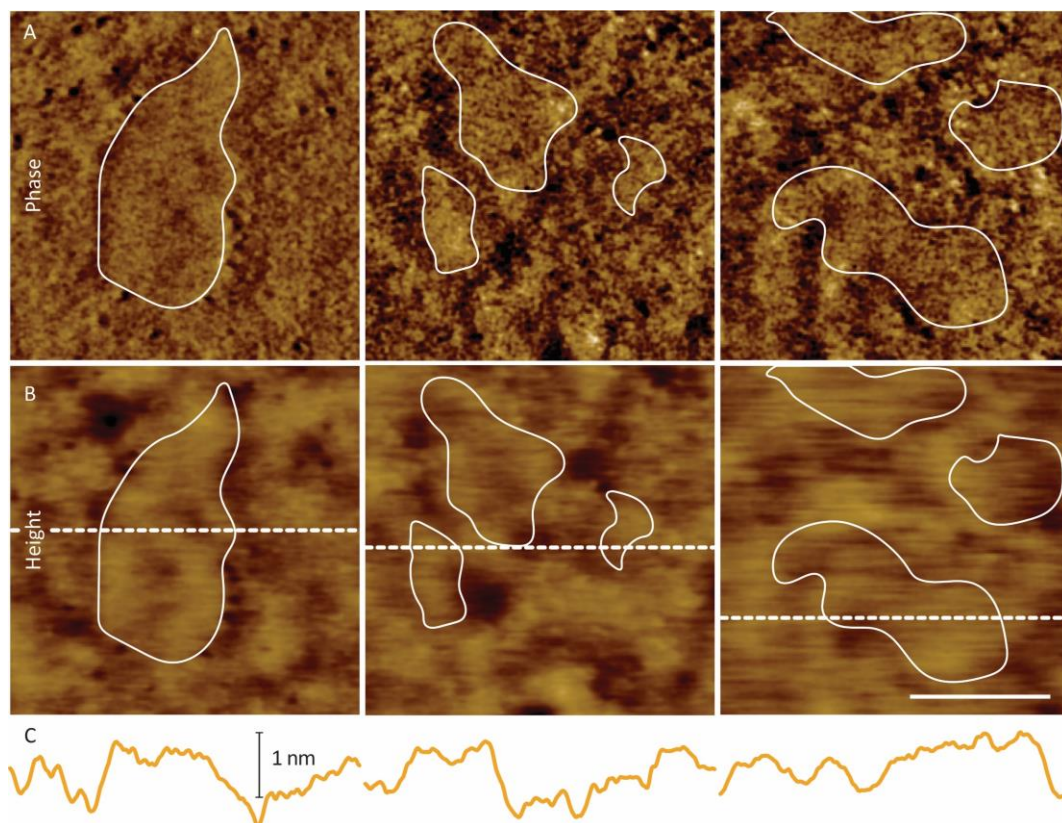


Figure 5.4. (A) Phase and (B) height images of cells lacking pore networks ( $\Delta\text{ompR}$  *pBAD18::ompR* 0.1% fucose) show patch-like, distinct, smooth regions within the rough OM. Potential patches are outlined in white. Dashed white lines in show location of height profiles in C. (C) Height profiles show the protrusions of  $\sim$ 0.5 nm that match WT-like patches. Scale bar is 100 nm. Colour bars are (A) 1.5, 0.5 and 1 deg and (B) 5 nm.

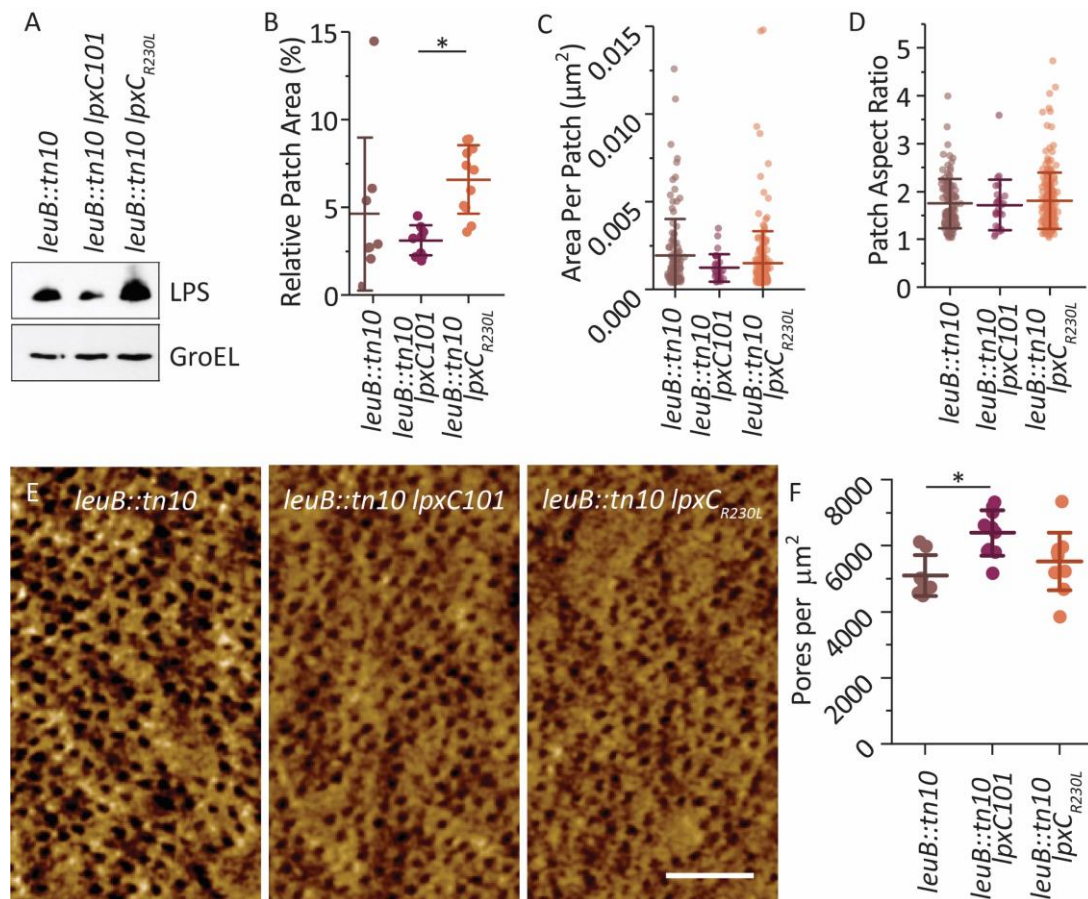


Figure 5.5. Patch size depends on LPS levels. (A) Western blot shows changes in LPS levels<sup>†††</sup>. (B) For low LPS levels (*lpxC101*), the cell area covered by patches is significantly smaller than for high LPS (*lpxC<sub>R230L</sub>*). Data were recorded in at least three independent experiments per condition; each data point represents one cell. (C) Lower LPS levels lead to slightly smaller patches. Each data point represents an individual patch from cells used in B. (D) Patch morphology (quantified by the aspect ratio) does not vary with LPS expression. Each data point represents an individual patch from cells used in B. (E) Typical phase images used to quantify B-D. (F) The number of pore-like structures per µm<sup>2</sup> are slightly higher when LPS is low, reflecting a drop in patch abundance. Data were recorded in at least three independent experiments per condition; each data point represents one cell. Scale bar is 50 nm. Colour bar is 1.5 deg. \* =  $p < 0.05$  and \*\* =  $p < 10^{-2}$ .

<sup>†††</sup> Provided by Dr Irina Mikheyeva-Bridges (Department of Molecular Biology, Princeton University, Princeton, New Jersey, USA).

## 5.2.4 Patches are LPS-Enriched Islands

Since the smooth patches contained no detectable protein, the impact of LPS was investigated. If the patches are LPS-enriched, higher levels of LPS in the outer leaflet would be expected to lead to a larger part of the bacterial surface being covered by them.

To test this, the levels of LPS were modulated by altering the efficiency of LpxC<sup>109</sup>, involved in the synthesis of lipid A<sup>†††</sup> (Figure 5.5A). Increasing LPS production led to a significantly increased fraction of the bacterial surface being covered by smooth patches (Figure 5.5B), whereas the overall morphology of the patches and packing of the pore network remained the same (Figure 5.5D-E). The decrease in patch area with low LPS levels also coincided with an increase in the overall number of observed pores per bacterial surface area (Figure 5.5F) and a slight decrease in mean patch size (Figure 5.5C). The fact that the patch area is dependent on LPS abundance provided evidence that these patches are phase separated, LPS-enriched domains.

If patches are indeed LPS-enriched phases, as their behaviour with different LPS levels suggested, their phase separation from the proteinaceous network should be increased by promoting LPS-LPS interactions (compared with LPS-protein interactions). MG1655 *E. coli* have no O-antigen, so LPS are primarily bound together by Mg<sup>2+</sup>, which strongly bridges the negatively charged LPS core<sup>2</sup>. By reintroducing *wbbL*, the O-antigen is restored and the long polysaccharide chains enhance LPS-LPS interactions<sup>22,24</sup>.

As predicted, this led to an increase in the mean relative patch area and a significant increase in typical patch size (area per patch) (Figure 5.6). Since the size of patches is dependent on LPS content and interaction strength, it was concluded that they are LPS-enriched phases.

---

††† Strains established by Dr Irina Mikheyeva-Bridges (Department of Molecular Biology, Princeton University, Princeton, New Jersey, USA).

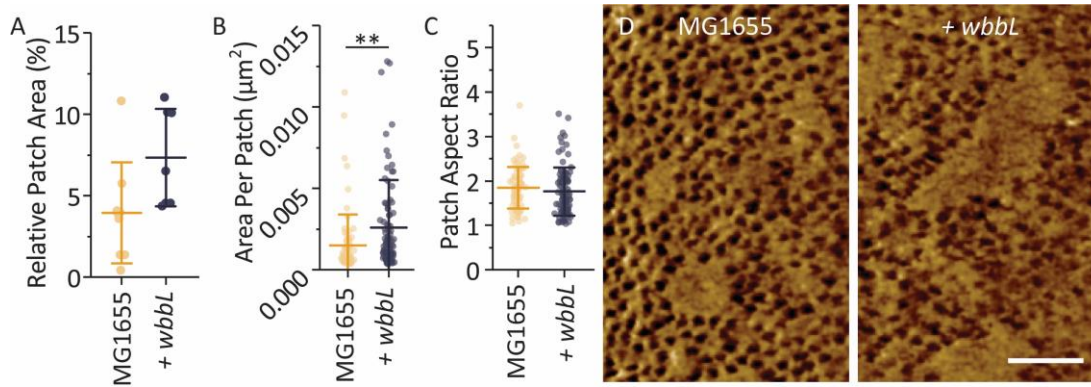


Figure 5.6. Patches are LPS-enriched domains. (A) Reintroduction of O-antigen and hence longer LPS (+ wbbL) results in twice as much area of the cell containing patches than for WT (MG1655). Data were recorded in at least three independent experiments per condition; each data point represents one cell. (B) Longer LPS chains result in larger patches. Each data point represents an individual patch from cells used in A. (C) Patch morphology does not change. Each data point represents an individual patch from cells used in A. (D) Typical phase images used to quantify A-C. Scale bar is 50 nm. Colour bar is 1.5 deg. \* =  $p < 0.05$  and \*\* =  $p < 10^{-2}$ .

### 5.2.5 Phospholipids Phase-Separate into New Structures

The observation of LPS patches and protein-rich networks raised the question of how these arrangements are disrupted by enhancement of phospholipid levels in the outer leaflet, as the third component of the OM. Phospholipids are usually restricted to the inner leaflet by the Mla pathway and the phospholipase PldA<sup>18</sup>. But, the combined deletion of *pldA* and disruption of the Mla pathway results in a ~25 fold

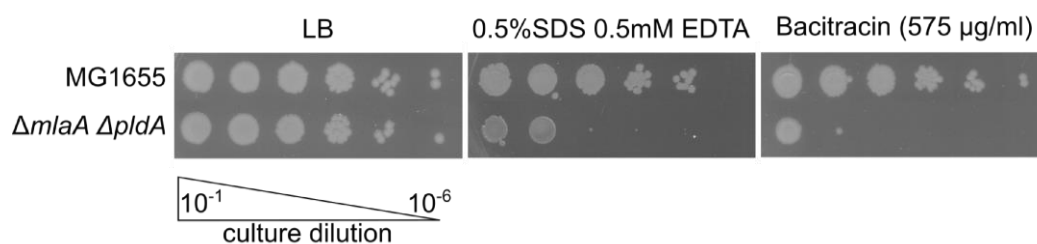


Figure 5.7. Efficiency of plating assays show sensitivity to SDS-EDTA and bacitracin is high in  $\Delta mlaA \Delta pldA$  cells, corresponding to high levels of phospholipids in the OM outer leaflet<sup>§§§</sup>.

§§§ Provided by Dr Irina Mikheyeva-Bridges (Department of Molecular Biology, Princeton University, Princeton, New Jersey, USA).

enhancement of phospholipids in the outer leaflet, compared with wild type<sup>18</sup>. This leads to sufficient disruption of the membrane to increase sensitivity to detergents and antibiotics<sup>18</sup> (Figure 5.7), but the mechanism of this disruption is not understood.

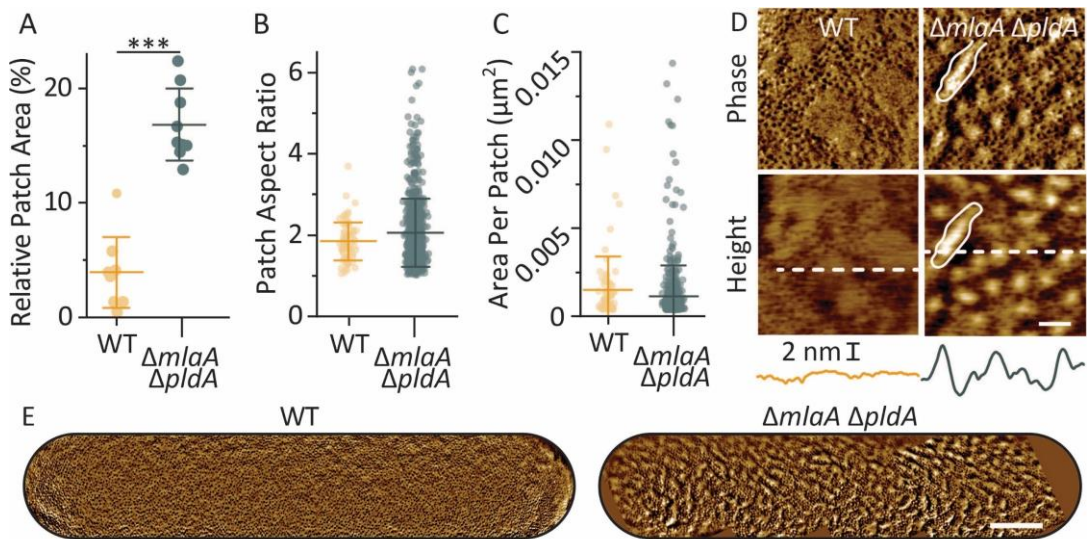
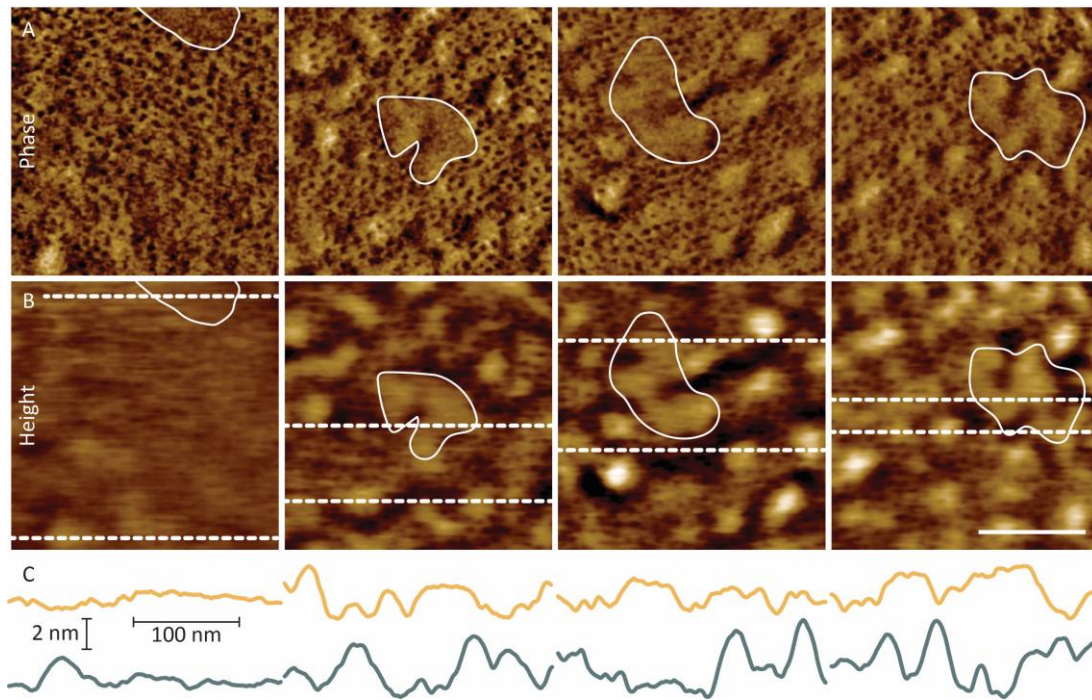


Figure 5.8. Effect of outer-leaflet phospholipids on domain formation. (A) For  $\Delta pIaA \Delta mIaA$  cells, a significantly larger fraction of the bacterial surface is covered by all pore-free patches, compared with WT (MG1655). Data were recorded in at least three independent experiments per condition; each data point represents one cell. (B) The aspect ratio of  $\Delta mIaA \Delta pIaA$  patches can be much higher than WT, an example of an elongated patch can be seen in D. Each data point represents an individual patch from cells used in A. (C) Although the mean area of each individual patch is not significantly different,  $\Delta pIaA \Delta mIaA$  cells have a greater spread of patch sizes. Each data point represents an individual patch from cells used in A. (D) AFM phase and height images of cells with mutations that disrupt lipid asymmetry in the OM. Height profiles are of dashed lines in the AFM images above. Solid white line highlights elongated patch. (E) Whole cell phase images of a MG1655 and a  $\Delta pIaA \Delta mIaA$  cell showing the extent of membrane reorganisation with abundant phospholipids. Scale bars are (D) 50 nm and (E) 200 nm. Colour bars are (D) 0.75 deg and 5 nm. \* =  $p < 0.05$  and \*\*\* =  $p < 10^{-4}$ .

As expected,  $\Delta mIaA \Delta pIaA$  cells showed substantial changes in their OM architecture. However, their OMs did not just show changes in pre-existing features. Instead, they gained an additional type of domain (Figure 5.7). Whole cell images show abundant, high (~2 nm), pore-free protrusions, here referred to as phospholipid-enriched

patches (Figure 5.8D), since they appear when the LPS-phospholipid asymmetry of the OM is disrupted. The phospholipid-enriched patches are distinct from LPS-enriched patches by this greater protrusion in height and by their shape: they are either small and round or very long (Figure 5.8C-D). In addition, LPS-enriched patches were observed alongside the abundant phospholipid-enriched patches on  $\Delta mlaA \Delta pldA$  cells (Figure 5.9).



*Figure 5.9. (A) Phase and (B) height images of  $\Delta mlaA \Delta pldA$  cells showing the presence of LPS-enriched and phospholipid-like patches on the same cell, providing further evidence that excess phospholipids form new structures in the outer leaflet. Both patches are pore-free but LPS-enriched patches are wide and flat (marked by white outline). Phospholipid-like patches are more abundant, narrow and tall. (C) Height profiles along dashed lines in B. Yellow profiles correspond to top lines that intersect the wide LPS-enriched patches protruding from the membrane by  $\sim 0.5$  nm. Green profiles correspond to bottom lines for profiles of the taller, phospholipid-like patches. Scale bar is 100 nm. Colour bars are (A) 1.5 deg and (B) 7 nm.*

The separation of LPS and phospholipids is plausible as the tight packing of LPS molecules by  $Mg^{2+}$  is very stable<sup>2</sup>. The reason for the larger height of phospholipid-enriched patches may be due to buckling of phospholipid-enriched patches to equilibrate lateral compression: a higher lateral compression is expected due to

excess phospholipids in the outer leaflet. Since the OM is tethered to the peptidoglycan<sup>2</sup>, it will have to release the compression without expanding away from the rest of the cell. Logically, this buckling would occur in the more fluid, softer phospholipid bilayer regions. However, the stiffnesses of either patch type or pore network, as measured by force curves in QI™ mode AFM, showed no difference (Figure 5.10).

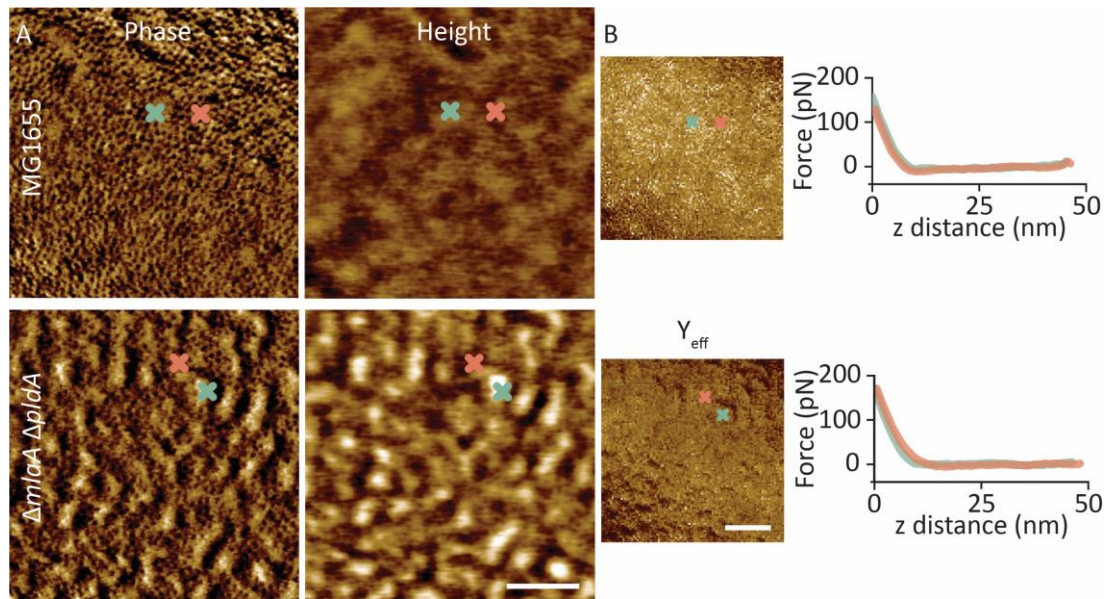


Figure 5.10. (A) Tapping mode phase and height images of WT MG1655 and  $\Delta mlaA \Delta pldA$  cells show the location of force curves shown in B. (B) Effective Young's modulus maps as determined by QI™ mode, showing no detectable difference in nanoscale stiffness of LPS-enriched and phospholipid-like patches (green) vs the pore network (pink). Typical force curves, corresponding to pixels marked by crosses, are also shown. Three images were recorded for each cell type. Colour bars are (A) 0.7 deg and 5 nm and (B) 7 MPa. Scale bar: 100 nm.

## 5.2.6 The Outer Membrane Ruffles at the Division Site

Another, more native cause of lateral compression and expansion on the OM occurs at cell division. *E. coli* cell division is initiated by the formation of the Z-ring on the inner membrane inner leaflet; once mature, the Z-ring contracts, pulling the inner membrane with it<sup>164</sup>. The peptidoglycan is simultaneously pulled and synthesised inwards, potentially also contributing to constriction by pushing<sup>164,165</sup>. The inner

membrane and peptidoglycan constriction is poorly understood. However, even less is known about how the OM constricts<sup>164</sup>.

Since the OM has no direct source of energy and, this chapter has shown, it contains a crowded network of OMPs and LPS, the mechanism of its constriction is not trivial<sup>163</sup>. Although some of the molecular components involved in OM constriction have recently been characterised<sup>163</sup>, the effect on OM architecture has not been investigated. The following data provide a preliminary perspective on OM architecture at the division site.

Although cells are dividing in the experimental set-up used in this chapter (Figure 5.1), the capture of cell division itself is challenging. Firstly, cell division is slow in these conditions ( $\sim 30$  °C, and adhered to a substrate), compared with the  $\sim 20$  min division time at 37 °C in rich media. This means that, to investigate the moment of cell division, high resolution imaging must be maintained for long time periods. Secondly, cells often detached from the surface as they divided (Figure 5.11A). Nevertheless, the division of some cells was recorded.

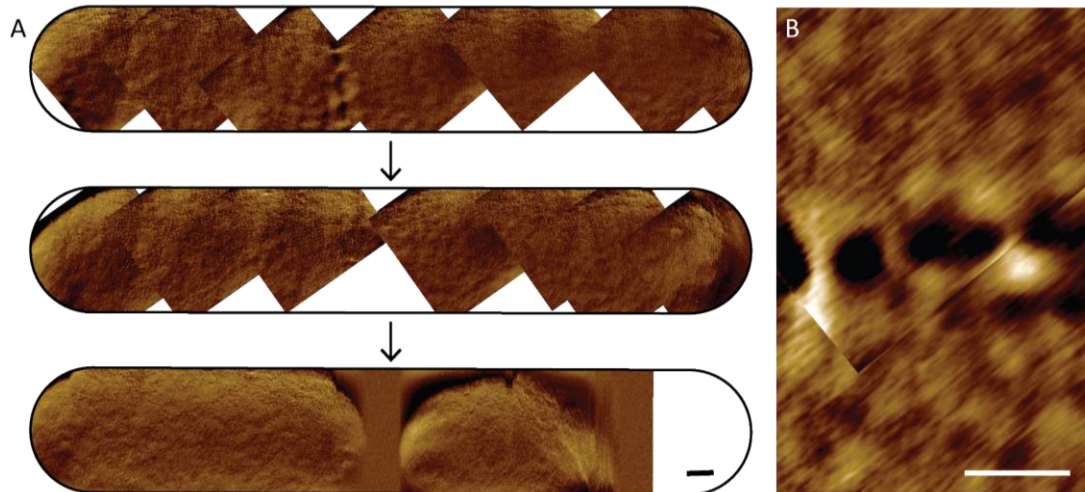


*Figure 5.11. Cells can be imaged for long time periods to track division. (A) Overlaid phase images taken at  $\sim 40$ -minute intervals. Once cells have divided, they often detached from the surface, as seen in the final image, where the bacterium seems to have disappeared at the far right. (B) Height image showing ruffling of the division site. The curvature of the cell has been removed by a 50-pixel low-pass filter. 2 scans are overlaid. Scale bars are 100 nm. Colour bars are (A) 2 deg and (B) 5 nm.*

A surprising OM feature was observed: the membrane appeared to ‘ruffle up’ at the division site (Figure 5.11B). This phenomenon was examined further by imaging division sites or new poles of many cells from MG1655 and BL21 *E. coli* (Figure 5.12A). Ruffling was seen on most cells, to varying degrees (Figure 5.12B), with entirely smooth division sites being relatively unusual.

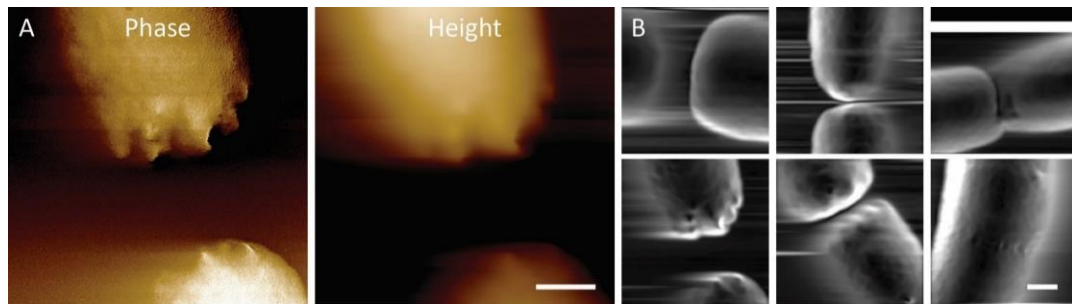


Figure 5.12. The division site often becomes very ruffled. (A) Phase and height images show ruffles on both new poles of a recently divided MG1655 cell. (B) Surface features in height images are highlighted by a Sobel edge detector. The degree of ruffling is varied, but cells rarely have no ruffling at constriction. Images are from MG1655. Scale bars are (A) 100 nm and (B) 200 nm. Colour bars are 4 deg and 300 nm.

## 5.3 Discussion

The data presented in this chapter demonstrate phase-separation of protein-rich networks and LPS-enriched domains as a prominent feature in the supramolecular architecture of the *E. coli* OM. In addition, when phospholipids are present in the outer leaflet, the resulting domain formation directly correlates with bacterial sensitivity to harsh environments, providing a first link between OM phase separation and functional behaviour of Gram-negative bacteria.

Like the ubiquitous protein lattice seen in Chapter 4, the here reported phase separation presents a different perspective from that of protein islands that are enriched in specific OMPs<sup>27,38,142</sup>, but is not necessarily incompatible. Instead, it suggests a way for different protein-rich domains (e.g., consisting of older and newer OMPs<sup>38</sup>) to exist by tight protein-protein interactions (PPIs), whereas phase-separated LPS-enriched domains can act as flexible separators to facilitate relative motion of protein islands without disrupting their internal organisation. The here

reported low mobility of LPS patches is also consistent with previously reported slow diffusion of LPS<sup>166,167</sup>.

LPS patches also provide a mechanism via which the OM may accommodate growth. The opening of LPS-enriched gaps in the protein network may facilitate insertion of new membrane while maintaining existing PPIs. That the patches may be a consequence of membrane growth seems likely, but evidence of this would require co-localisation of patches and components of OM assembly, primarily BamA and LptD.

In addition to LPS-enriched patches, a second patch-type was produced by phospholipids that were mislocated in the outer leaflet. Although there is no chemical identification that phospholipids are in these patches, it is likely they are enriched in the phospholipid-like patches for two reasons. Firstly, excess phospholipids in the OM of  $\Delta mlaA \Delta pldA$  cells must go somewhere and they are not disrupting the lattice as the packing of pores does not change<sup>107</sup>. Secondly, the new patches are not an extension of LPS-enriched patches as they behave in a different way, and the two are seen alongside each other. The appearance of phospholipid-like patches within the protein network, separate from LPS-enriched patches, may also explain why MlaA must interact with OmpC and OmpF in the OM<sup>168</sup>, as this would keep MlaA in the areas (i.e., not the LPS-enriched patches) where mislocalised phospholipids coalesce.

The mechanical properties of patches were expected to be different. However, AFM measurements showed similar Young's moduli for all pixels. This may have been due to limitations of the AFM measurement, since even when indenting locally, the AFM stiffness measurements may represent mechanical properties integrated over a larger area and depth. This could mean that differences in stiffness between patches remained undetected. Alternatively, the compression of phospholipids to their buckled appearance may have equilibrated any differences that might have been present without compression.

The properties of the OM may also be the cause of observed ruffling. The ruffles resemble the effect on fabric when a drawstring bag is tightened and this may be

similar to what is happening as the OM is constricted. Its viscosity and tethering to the peptidoglycan prevent components from flowing out of the division site and the membrane buckles. The reason for different levels of ruffling is not clear. A plausible explanation is that the OM keeps adapting to its new shape, such that the here reported ruffling may be dependent on the time at which the image is recorded: in some cases of imaging a cell by AFM with an initial low-resolution scan, the division site often appeared ruffled but, by the time a high-resolution scan was started (minutes later), the division site had smoothed out.

The perspective from AFM imaging of live bacteria allows a comparison of global and local OM properties. In this chapter, its organisation and phase separation have been studied at nanometre length scales, and the response of the OM to constriction has been explored. Using similar methodology, one can probe changes in the OM upon exposure to immune effectors and antimicrobials, as discussed in the following chapter.

# Chapter 6

## The MAC on Gram-Negative Bacteria

In the previous chapters, the architecture of the native outer membrane (OM) has been studied revealing the organisation of this complex barrier. In this chapter, the targeting of the OM by the membrane attack complex (MAC) is investigated. The MAC is the product of the terminal pathway of the complement system in serum and directly lyses cells. By imaging the entire accessible bacterial surface, it was found that MACs deposit randomly relative to each other and the cell. By combining AFM with fluorescence microscopy, cells are found to be surprisingly resilient even to large numbers of MACs inserted into their OM. Subsequent cell death is correlated with significant mechanical destabilisation of the bacterial cell envelope, as observed by a sudden drop in AFM resolution on the OM.

### 6.1 Introduction

The MAC is an important part of our immune system, with deficiencies in its constituents leading to recurrent infections of Gram-negative bacteria<sup>72</sup>. However, it has also been shown to accumulate on the surface of Gram-positive bacteria, with polar or septal localisation, depending on the species<sup>76</sup>. Distinct localisations of MAC have not been shown on Gram-negative cells, although, the instability of newly cleaved MAC components and covalent binding to the membrane suggests they could form clusters<sup>53,73</sup>. Furthermore, given the positive feedback loops in complement activation (notably for deposition of convertases)<sup>69</sup> and given that disruption of the membrane by one MAC could locally lower the energy required for subsequent MAC insertion<sup>72</sup>, one might predict MACs to cluster or to form branches.

As well as a lack of clear evidence of clustering and despite extensive knowledge of the complement pathway<sup>66</sup>, the structure of the MAC<sup>74</sup> and recent progress on the kinetics of formation<sup>53,77</sup>, the mechanism of lysis by MACs remains unclear<sup>79</sup>.

Instinctively, the formation of large holes in the highly selective OM suggests an influx of water or proteins will lead to cell lysis. However, there is no osmotic gradient across the OM due to the sieve-like nature of abundant porins, so it is unlikely that water would rush into the periplasm<sup>2</sup>. Furthermore, the MAC is still an effective antimicrobial when added in a semi-purified manner such that, once the MAC is fully formed, C9 is the only protein present<sup>53</sup> and it cannot permeate membranes alone<sup>77</sup>. This suggests that, while other serum proteins may enhance MAC killing, protein influx is not the only mechanism of lysis<sup>83</sup>.

Other than protein influx or osmotic disruption, a third theory of MAC lysis has been that insertion triggers association of the inner and outer membranes, leading to flow and lethal accumulation of phospholipids to the inner membrane<sup>169</sup>. Although this theory has been less studied, any association of MAC components to the inner membrane has never been seen<sup>169</sup>.

Finally, the MAC could also initiate a lethal stress response<sup>169</sup>. Cryo-EM structures suggest MAC formation affects the bending modulus of membranes which could lead to mechanical signalling in cells<sup>72</sup>. It is also established that the stress responses of *E. coli* that respond to disruption of the OM can be fatally over-activated in other circumstances<sup>170</sup>. However, this theory has not been investigated in detail.

While the aforesaid effect on membrane bending modulus could lead to mechanical signalling<sup>72</sup>, it could also lead to destabilisation of the membrane. Indeed, there are further hints that MACs impact the structural integrity of the OM by the observation that mutations that promote serum resistance often lead to increased OM integrity<sup>171</sup>. It has also been shown that the OM bears a significant portion of the intracellular pressure<sup>143</sup>, so weakening of the OM will promote cell lysis. However, OM destabilisation has not been considered as a mechanism of MAC lysis.

By combining AFM with brightfield and fluorescence microscopy, we investigate global deposition of MAC and lysis of bacteria at the single cell level. This novel perspective shows MAC insert randomly in the membrane and leads to a new hypothesis of how the MAC kills its primary target.

## 6.2 Results

### 6.2.1 The MAC Can Be Visualised by AFM

The MAC can form via three pathways: the classical, alternative and lectin pathways<sup>65</sup>. To investigate how MACs form on the OM using AFM, a semi-purified approach was used, mainly relying on the alternative pathway<sup>53</sup>. Briefly, human serum deficient in a key component of the terminal pathway, C5, was added; this allowed the alternative pathway to proceed almost to completion. The serum was then removed and purified MAC components (C5, C6, C7, C8 and C9) were added. This protocol ensured that, once MACs were assembled, only the other MAC components were present i.e., no serum components could have contributed to cell death.

AFM was performed on MAC-treated BL21 *E. coli* immobilised onto PLL coated coverslips in HEPES buffer and showed MACs that matched the split washer conformation and dimensions predicted by Cryo-EM<sup>74</sup> (Figure 6.1A-B) and seen previously on lipid bilayers and bacteria<sup>53,77</sup>. As seen for the native membrane, phase images showed greater contrast than height, this time due to large differences in mechanical properties<sup>123</sup> of the membrane and proteinaceous MAC ring (Figure 6.1C-D). For this reason, analysis was generally done using phase images. To investigate the entire surface of cells, small scans were taken across the surface and overlaid for nanometre resolution information over micron scales (Figure 6.1E). Once it was established that the MAC could be imaged by AFM, their deposition was investigated further.

### 6.2.2 The Pattern of MAC Insertion is Highly Varied

The density of MACs varied dramatically between samples (Figure 6.2A-C) and C9 concentrations above 100 nM had little effect on insertion as 100 nM was already excess under the conditions that applied here<sup>53</sup> (Figure 6.2C). Therefore, subsequent

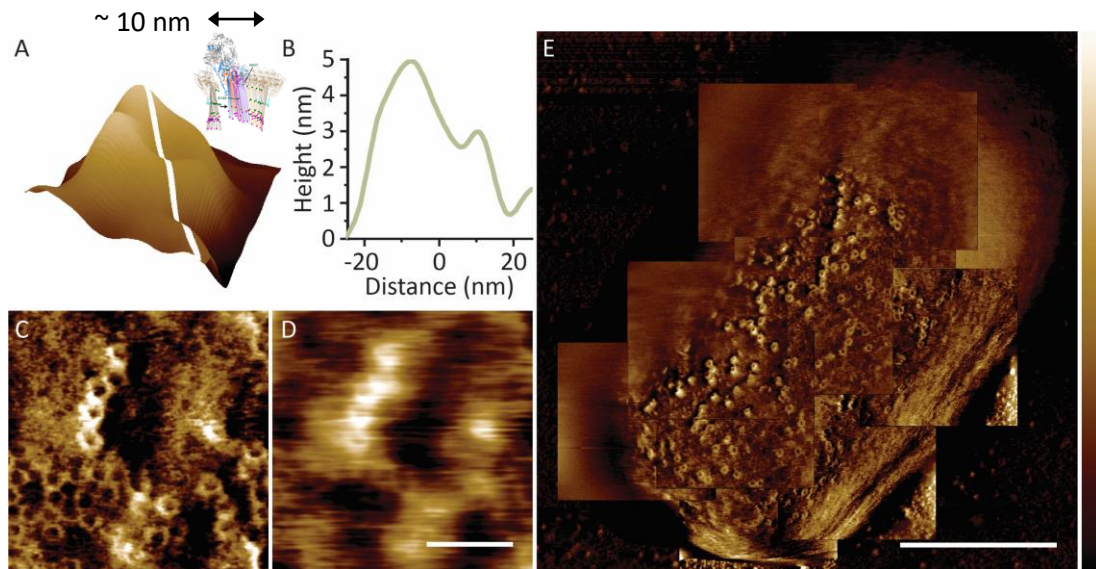


Figure 6.1. The MAC may be imaged by AFM on the surface of whole bacteria. (A) 3D height surface plot of a single MAC suggestive of the presence of the protruding C5b-8 stalk in the pore structure. (B) A height profile, across the white line in A, shows that lateral dimensions match those seen in the Cryo-EM structure<sup>74</sup>. The height of the MAC was lower than expected, most likely due to proteins and LPS coating the underlying membrane. (C) Phase images show MACs more clearly than (D) height images. (E) Small scans of the surface were overlaid to get high resolution images of the entire cell surface. Scale bars are (D) 100 nm, (E) 500 nm. Colour bars are (A) 10 nm, (C) 3 deg, (D) 8 nm and (E) 3 deg.

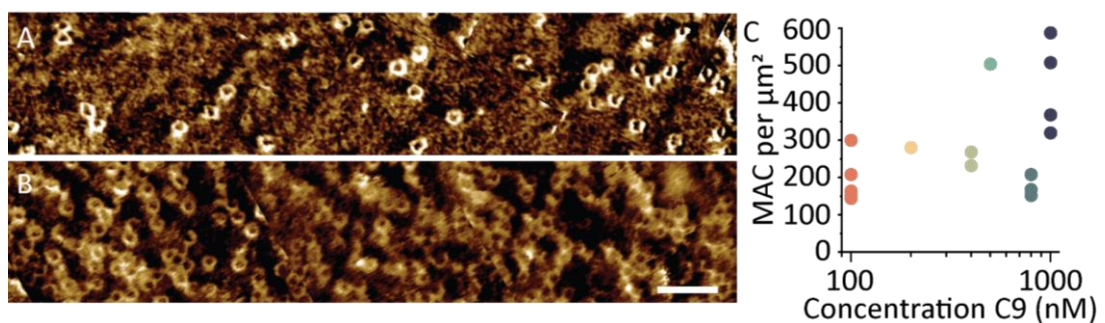


Figure 6.2. MAC distribution was highly variable on different cells. (A-B) Whole cell, phase images show the overall densities of MACs on the surface was highly varied. Some cells had (A) sparse MACs, whereas some had (B) dense packing of MACs. (C) The number of MAC in the surface was highly varied between samples, with no consistent increase from 100 to 1000 nM. Scale bars are 100 nm. Colour bars are (A) 2 deg, (B) 3.25 deg. Data is from MACs on 16 cells in independent experiments.

analysis on insertion patterns used all samples with C9 concentrations of 100 nM or more.

To investigate insertion patterns, MACs were identified manually and their relative (x,y) coordinates recorded on each cell. The cell-wide, high resolution AFM made it possible to study how MACs are distributed over the cell surface. Specifically, the cell was subdivided into 5 regions from midpoint to pole and MACs in each region were counted: no significant difference was seen in the probability of MACs occurring at any specific point along the long axis (Figure 6.3A-B). This suggests that, contrary to the case of Gram-positive bacteria<sup>76</sup>, MACs do not favour distinct localisations on *E. coli*.

Instead of clustering by cell location, the observed MAC locations suggested a different patterning depending on local MAC concentration. When the density was high, MACs fitted tightly together in clusters (Figure 6.3C), similar to multimers seen by Cryo-electron tomography of MAC in lipid bilayers<sup>70</sup>. However, when MACs were sparse, they appeared to favour branching lines (Figure 6.3D).

To quantify whether MACs favour chain and cluster formation, real coordinates were compared to randomly generated coordinates in the same area. The tendency for MACs to cluster on large scales or small scales, and to form chains, were all investigated. To avoid any artefacts (e.g., boundary effects) due to the finite sizes of the AFM scan areas, the results from experimental data were compared with results based on randomly allocated positions in areas that matched the experimental scan areas, in shape and size.

Comparing experimentally determined MAC locations with the computationally generated random locations, no significant differences were found for the nearest neighbour distances (Figure 6.4A) and overall nearest neighbour distributions also showed no significant difference, as assessed by a  $\chi^2$ -test (Figure 6.4B). These data suggest MACs are not attracted to one another to cluster on small scales. To investigate larger scale clustering, pair distributions were analysed too (i.e., the distribution of absolute distances between all MACs) and again this also showed no

difference between real and random coordinates (Figure 6.4C), also consistent with the absence of any preferential MAC positions over the entire cell surface.

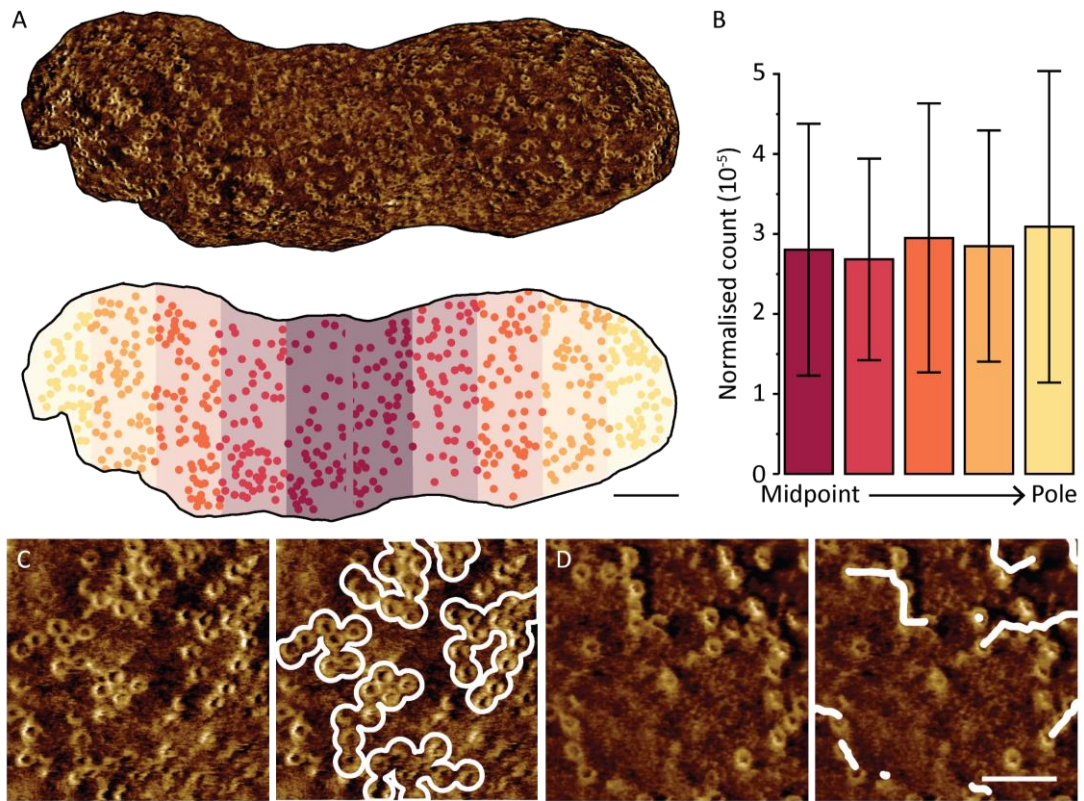


Figure 6.3. MAC are distributed evenly over the surface of a single cell. (A) Above, AFM phase images were used to identify MACs and the cell midpoint. Below, the surface was divided into 10 regions from midpoint to pole. The number of MAC in each region was counted and the count normalised to the imaged area in each region. (B) There was no difference in MAC insertion across the cell.  $N = 5$ . (C) MACs appeared to cluster in groups when density was high, leaving regions of bare membrane. Right, MAC clusters are marked in white. (D) When the density was lower, MACs appeared to form in lines. Right, branches of MACs are shown in white. Scale bars are (A) 200 nm and (C-D) 100 nm. Colour bar is (C-D) 3.5 deg.

Finally, chains of experimental MAC positions were found and compared to the random coordinates. By taking each MAC as a point, dilating them until neighbouring MACs touched and skeletonising the resulting shapes, chains of MACs could be quantified by the longest branch length (Figure 6.5A). This showed that MACs positioned into chains on the bacterial surface no more than would be expected based on an entirely random set of positions (Figure 6.5B-C).

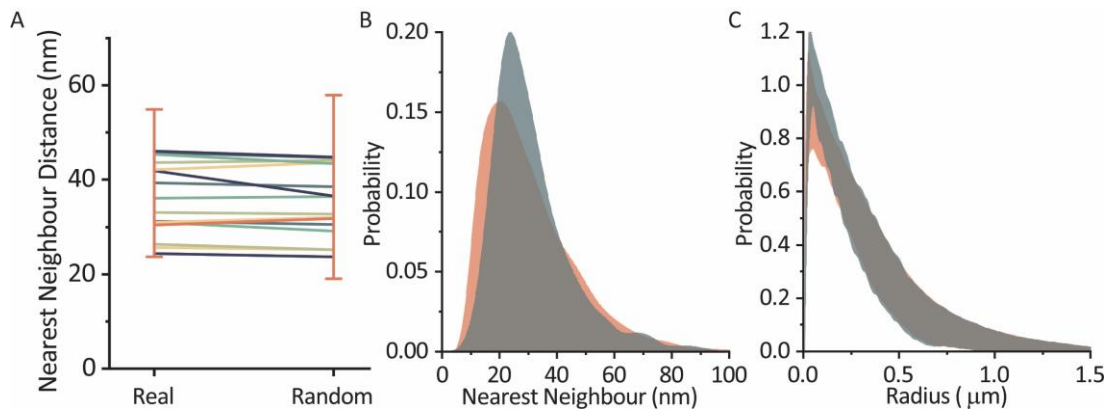


Figure 6.4. (A) A comparison of individual real and random nearest neighbour means shows real samples are no different to random (by largely horizontal lines). Error bars show typical standard deviations, only one sample standard deviation is shown for clarity. (B) Histogram of all nearest neighbours show similar distributions for real (green) and random (pink) data. (C) Radial distributions show no difference between long-distance clustering of MACs from random points. Bands corresponding to real (green) and random (pink) standard deviations are shown. Data is from MACs on 16 real cells.

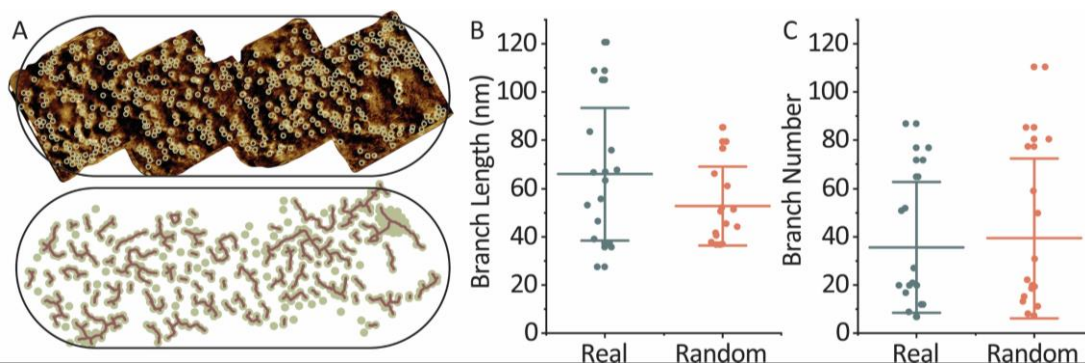
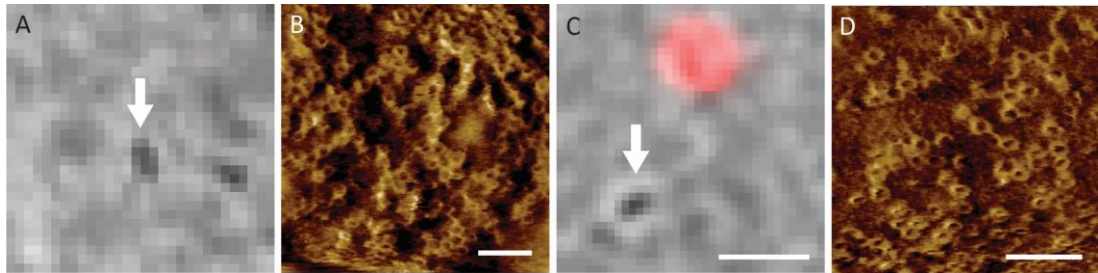


Figure 6.5. (A) Chains of MACs were investigated by picking MAC points, dilating them to circles that overlap when nearby, skeletonising the resulting shape and finding the longest branch. This showed that (B) real and random points led to branch lengths of approximately equal size. (C) The number of branches in real data was also not significantly different to random. Data is from MACs on 16 real cells.

### 6.2.3 The Mechanism of Lysis by MAC

When investigating the locations of MACs on the bacterial surface, it was observed that they can be present at very high densities. Using AFM in combination with

fluorescence microscopy, dead cells could be stained by SYTOX™. Surprisingly, extensive MAC pore formation at the bacterial surface did not immediately correlate with inner membrane permeation and cell death (Figure 6.6). The resilience of Gram-negative bacteria to many, wide pores in their OM is unexpected, particularly as early studies on erythrocytes show cells require only one MAC for lysis<sup>172</sup>.



*Figure 6.6. (A and C) Merges of brightfield (grey) and SYTOX™ (red) images. White arrows indicate bacteria imaged in B and D respectively. (B and D) Phase images show that live bacteria are covered by many MACs. Colour bars are 4.5 deg. Scale bars are (A and C) 5  $\mu\text{m}$  and (B and D) 100 nm.*

Another surprising observation of MAC-treated cells was that, once the inner membrane was permeabilised (as assessed by SYTOX™ staining), AFM imaging was erratic (Figure 6.7). Since AFM relies on a force between the tip and the sample, it requires a mechanically stable background to facilitate high-resolution imaging. Hence, the poor resolution and unstable OM imaging on dead cell OMs suggested that the cell envelopes were destabilised and the correlation between OM stability and inner membrane permeability suggested they may be linked to the mechanism of MAC lysis.

This correlation was further confirmed by experiments in which AFM and fluorescence microscopy images were required as a function of time. The loss of OM stability, as assessed by stability of AFM imaging, was found to correlate with cell death, as next assessed by SYTOX™ staining (Figure 6.8).

To further examine the correlation between cell death and OM integrity, simultaneous AFM-fluorescence microscopy was used to determine whether OM

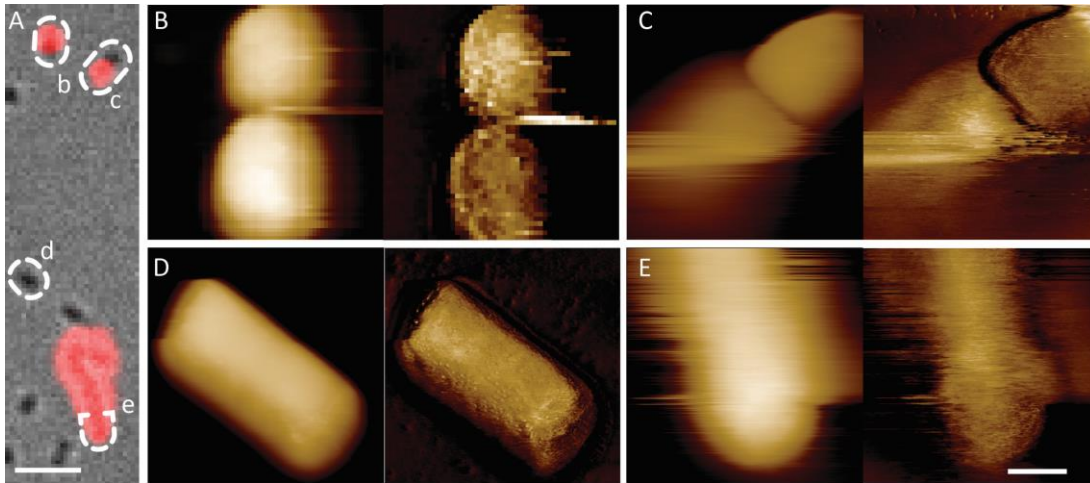


Figure 6.7. (A) Merge of brightfield (grey) and SYTOX™ (red) images with bacteria imaged in B-E indicated with corresponding letters. (B-E) Height (left) and phase (right) images show that, when cells are dead (both cells in B, the bottom cell in C and the cell in E), their OM becomes unstable and fluctuating. However, the membranes of live cells (top cell in C and cell in D) are stable and intact. Vertical height scale is 600 nm and phase scales are (B) 10 deg, (C) 20 deg, (D) 15 deg and (E) 15 deg. Scale bars are (A) 5  $\mu\text{m}$  and (B-E) 500 nm.

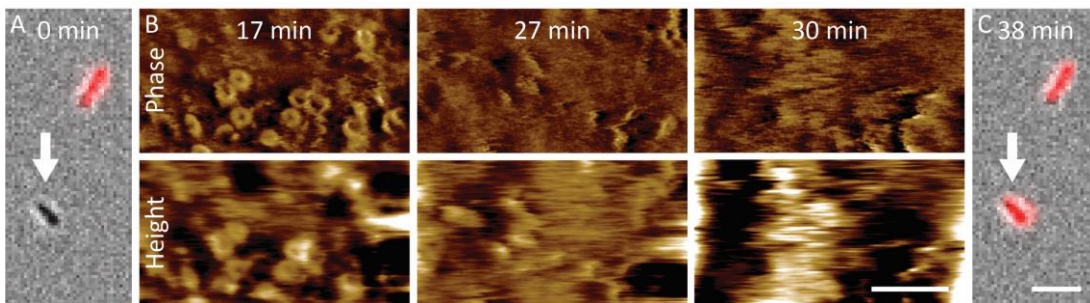


Figure 6.8. OM destabilisation appears temporally correlated with inner membrane permeabilization. Often, a cell with initially clearly resolved MACs became impossible to image, and stained positive for SYTOX™ in subsequent fluorescence microscopy, demonstrating inner membrane permeabilization. (A and C) Merge of brightfield (grey) and SYTOX™ (red) images show the bacterium imaged, indicated by the white arrow, is alive when imaging starts (defined as 0 minutes), but dead 38 minutes later. (B) When AFM imaging begins, MACs are clearly resolved. The resolution of the images rapidly deteriorates after 20 minutes, until the surface is completely unstable. Colour bars: (B) 2 deg and 10 nm. Scale bars: (A and C) 5  $\mu\text{m}$  and (B) 100 nm. Time points are relative to the initial image.

destabilisation preceded inner membrane permeabilization. The two events were found to be highly correlated, happening within 30 seconds of each other (Figure 6.9). MACs are generally highly stable in the membrane, moving very little. In Figure 6.9, the position of MACs rapidly changed after 54 seconds, suggesting the membrane itself had come loose. This was swiftly followed by a drop in resolution and slight increase in root mean square deviation (RMS), indicative of a now slack and fluctuating membrane. Inner membrane permeabilization then occurred and the resolution rapidly dropped further.

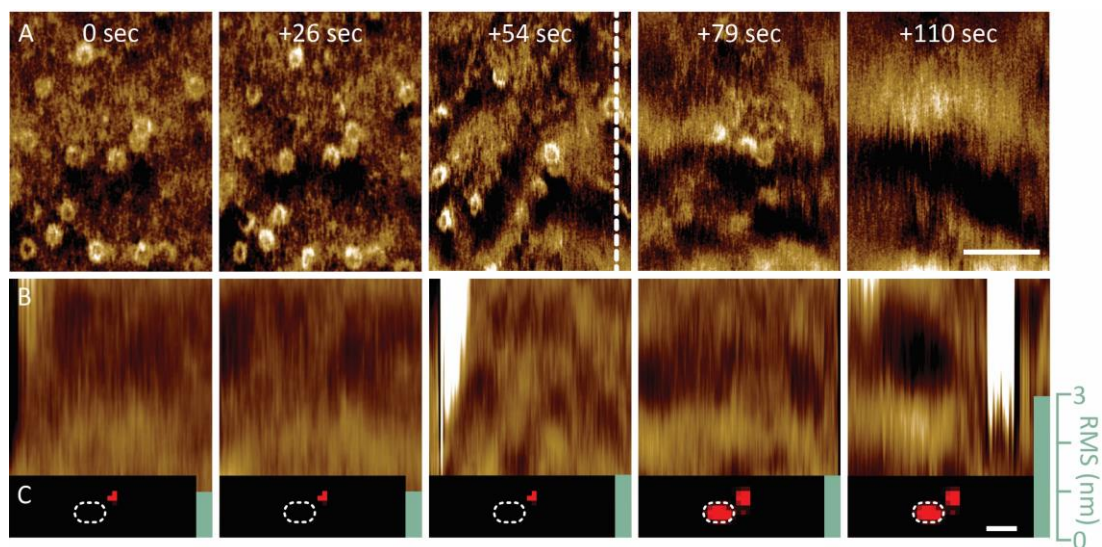
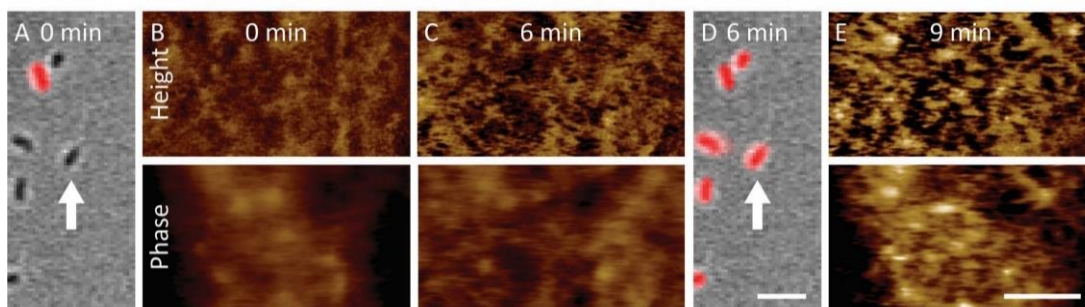


Figure 6.9. (A) Phase and (B) height images of the same area over time. (C) Fluorescence shows bacterial cell death and the green bar shows RMS roughness of height images. The start time of each scan is shown above. The AFM images are shown with the fast scan direction vertically. So, as time proceeds, subsequent scan lines are added to the image from left to right in this representation. MACs initially appear stable in phase images (0, +26 sec), but next appear to rearrange or disappear (+54 sec), whereas in the height images, the RMS corrugation increases, after which the bacteria appear SYTOX™ positive, indicating inner membrane permeabilization. The exact time of the first SYTOX™ flush is shown by the dashed white line. Finally, the OM completely destabilises in less than 1 minute, shown by a total loss of resolution and large increase in RMS. Colour bars: (A) 2 deg and (B) 10 nm. Scale bars: (A) 100 nm and (C) 500 nm. Time points are relative to the initial image.

For comparison, this rapid destabilisation is not observed for other antimicrobials that target the membrane. Melittin is an antimicrobial peptide known to cause lesions in the outer and inner membranes<sup>62</sup> and, by AFM, holes appeared in the OM and the surface roughened (Figure 6.10B-C), but imaging appeared to remain stable, even after the inner membrane had been permeabilised (Figure 6.10D-E). This suggests that the slackening of the OM produced by the MAC is not merely an effect of inner membrane permeabilization, but related to its mechanism of lysis.



*Figure 6.10. (A and D) Merges of brightfield (grey) and SYTOX™ (red) images show the imaged bacterium, indicated by the white arrow. (B, C and E) Phase and height images show that the OM remains intact throughout melittin killing as the high resolution and roughening surface features are still visible. The roughness is reflected by an increase in RMS from 4.79 nm in B to 13.18 nm in C and 40.41 nm in E. Colour bars are 2 deg and 10 nm. Scale bars are (A and D) 5 μm and (B, C and E) 100 nm. Time points are relative to the initial image.*

## 6.3 Discussion

The existence of a large pore deposited by the immune system into target membranes has been known since the early 1960s<sup>173</sup>. But the way this pore kills bacteria and the level of deposition remain unclear<sup>169</sup>. The deposition of MAC may have an impact on their function or provide insight into their mode of insertion. With local amplification of the terminal complement pathway by C5 convertases<sup>69</sup>, one might expect local bursts of C5b6 complexes at distinct points on the surface, and hence clusters of MACs to form if precursors bound directly to the adjacent

membrane. However, this chapter has shown that MACs insert randomly relative to each other and to the cell.

This random arrangement cannot be due to the random movement of the MACs themselves, after insertion, as they appear static in the AFM images, like native OM proteins<sup>32</sup>. More likely, the random positioning occurs as the more mobile precursors (e.g., C5b6) diffuse before binding to the membrane more strongly<sup>73</sup>. The lack of preference to insert in specific regions of the cell is also contrary to the behaviour of MAC observed on Gram-positive cells<sup>76</sup>, with the caveat that the very poles of the bacteria remain inaccessible for the AFM tip in the experiment reported here.

Additionally, AFM of MAC treated bacteria has suggested that MACs lyse cells by mechanically destabilising their cell envelope, including, or in particular, their OM. Destabilisation of the OM has previously been shown to increase cell death, particularly during osmotic fluctuations, which is likely important during MAC lysis<sup>169</sup>. Of note, it was shown in 2018 by Rojas et al. that the OM of Gram-negative bacteria is important for maintaining the mechanical integrity of the entire cell<sup>143</sup>.

It is now well established, based on recent cryo-EM structures<sup>72</sup>, that a single MAC is not sufficiently high to perforate across OM, periplasm and inner membrane. Moreover, inner membrane permeation appears independent of MAC precursors C5-8<sup>53</sup> and C9 alone does not bind to membranes<sup>77</sup>. Hence it appears that inner membrane permeabilization must be an indirect effect of MAC formation in the OM, and mechanical destabilisation could be a mechanism by which this occurs.

Assuming that the MAC does kill Gram-negative bacteria by destabilizing their OM, a stronger OM would lead to a greater resistance to complement lysis. It is known that LPS contributes towards MAC resistance by preventing access to the OM<sup>174</sup>, but the LPS also contributes toward the mechanical stability of the OM<sup>143</sup>. As such, the LPS may increase MAC resistance even after MAC have formed. This would also be the case with proteins that stabilise the OM, for example, OmpA and Lpp<sup>16,143</sup>. In fact, several mutations that confer resistance to serum killing increase the integrity of the OM including *lpp* and *bamB*<sup>171</sup>. Similarly, drugs that reduce the mechanical stability of membranes may increase susceptibility of MAC-targeted cells to lysis.

Although evidence for OM destabilisation is not complete, the ability to identify single MACs on single cells has led to a new view of MAC lysis. Further investigation of the effects on membrane disruption, what leads to a varied time from MAC insertion to lysis and the precise order of membrane events will all contribute towards this and are all interesting avenues for further study.

# Chapter 7

## Conclusions and Outlook

The outer membrane (OM) is an important barrier that protects Gram-negative bacterial cells<sup>2</sup>. It reduces the entry of antibiotics, can prevent antimicrobial peptide action and resist serum killing<sup>169</sup>. This makes it important to understand OM organisation and integrity. However, the composition of the OM is complex, with diverse and abundant proteins<sup>2</sup>, rendering the labelling of specific proteins for fluorescence microscopy challenging. The determination of OM architecture is further complicated by the scale on which it is arranged, an *E. coli* cell is  $\sim 2 \mu\text{m}$  long<sup>54</sup>, meaning nanometre resolution data is required for distinct localisation of components. Super-resolution fluorescence microscopy can reach  $\sim 50 \text{ nm}$  resolution, however, this is not trivial and at the limit of what is necessary for OM organisation. In this thesis, these labelling and resolution challenges are overcome by, instead, using atomic force microscopy (AFM).

Nevertheless, there are limitations and challenges in AFM. Firstly, while high compared to fluorescence microscopy, the resolution is relatively low compared to other biophysical techniques, for example, x-ray crystallography or cryo-EM can gain atomic resolution. AFM can, theoretically, go to atomic resolution, however, the need to image in liquid and the softness of biological samples makes this much harder to achieve. Any improvement would primarily require improvement in cantilever properties: softer, sharper and more reliable.

AFM still has advantages over traditional biophysical techniques because it can be done over time, on live cells. Yet, the temporal resolution of our AFM (10s of seconds per frame) is slow compared to fluorescence microscopy (fractions of a second per frame), meaning that very dynamic processes will be missed. Despite our own limitations, AFM has been done at sub-second frame rates on live cells, with single nanometre resolution<sup>37,52</sup>. But these results are gained on home-built AFMs, without

the ability to perform simultaneous fluorescence and brightfield imaging which, in this thesis, was a priority for experiments to track cell death and ensure cell division was occurring.

The ability to image dividing cells was facilitated by keeping cells in close-to-physiological conditions. However, cells are still immobilised onto glass which may affect membrane properties. A further caveat to AFM, related to physical interactions, is that the tip of the cantilever is interacting with the sample. Although the forces of this interaction are minimised, some interaction is essential to acquire an image. However, this can be monitored in the future by intentionally increasing the force of imaging and seeing if diffusions increase further.

The requirement to non-covalently immobilise bacterial cells onto glass has also remained a major hurdle in AFM. This has been systematically studied in only a few papers, often with conflicting results<sup>87,105,115,134,136,175</sup>. In this thesis, the initial establishment of robust sample preparation in Chapter 3 was essential for the nanoscale investigation of *E. coli* as reported here and should be useful for other microscopists in the field.

In future, these protocols could be explored further to immobilise different species, or stationary phase bacteria as there are multiple questions about the change in OM organisation as cells become dormant and in different species. For other Gram-negative bacteria there are many comparisons to make with *E. coli* since some, like *V. cholerae*, have a less asymmetric OM<sup>10</sup>, potentially changing the behaviour of domains reported in this thesis. It would also be interesting to see the impact of different OMP compositions on OM architecture; for example, *P. aeruginosa* does not use the highly abundant trimeric porins of *E. coli*<sup>10</sup>.

In Chapter 4, the ability to resolve structures only a few nanometres wide, on the surface of live bacteria was used to investigate the arrangement of proteins in the OM. It shows that the bacterial surface is filled by a network of the trimeric porins, predominantly OmpF and OmpC, which is remarkably static given that large OM rearrangements are required to facilitate cell growth and division. Further use of novel labelling techniques also revealed OmpA, an abundant and monomeric OMP,

distributed throughout this network. Preliminary data on the deletion of *ompA* was also of interest.

The disruption of the porin network in  $\Delta ompA$  cells was entirely unexpected and may be due to OmpA acting as a means to couple the porin networks with the underlying cell wall or having a role as a spacer in the network; its abundance would make it ideally suited to non-specific binding of neighbouring OMPs to control order.

The validation of OmpA-related effects on OM architecture is a priority for future experiments. The reintroduction of OmpA without the peptidoglycan-binding domain is also an important experiment: if this were to restore resolution of the network, it would support the hypothesis that poor imaging is not due to a looser membrane, but local coupling of the porin network to the peptidoglycan cell wall. The specificity of this lattice disrupting effect could also be tested by the overexpression of a similar monomeric OMP, like OmpX<sup>10</sup>.

The use of AFM to image all components of the OM, without labelling, was exploited in Chapter 5, leading to the discovery of distinct, protein free, LPS-enriched patches in the porin network, revealing phase separation in the OM for the first time. The relevance of this observation is that it reveals previously unknown levels of order in the OM architecture, different from previously postulated OMP islands. Furthermore, the reported data are technologically novel by the combination of high-resolution AFM imaging with nanoscale labelling, borrowing methods from fluorescence imaging<sup>38</sup>, and allowing the biochemical identification of features in the chemically non-specific AFM topography.

The functional role of the LPS patches remains uncertain; but they may help accommodate cell growth without disrupting the protein lattice. To prove this further, combination of labelling experiments and long-term imaging of dividing cells would be required. For example, by labelling OmpF and letting cells grow, the location of unlabelled regions would show where new OMPs are, relative to patches, and provide high resolution data on OMP insertion. The development of labelling of OMPs involved in OM synthesis like BamA and LptD<sup>2</sup> would also provide information on how OMPs and LPS are inserted relative to patches; for example, is LPS inserted

in the patches or do the molecules gradually separate from the protein network, i.e., could the LPS patches be hotspots for synthesis or insertion of OM components?

We also showed that modulating LPS levels leads to changes in the patch size. By contrast, the introduction of phospholipid in the outer leaflet led to the appearance of a second patch type. The appearance of these cells was striking, almost 20% of the surface was made up of patches which seem to have buckled, probably due to membrane crowding from ~25 times more phospholipid in the outer leaflet. Given that the appearance of phospholipid-related patches correlates with enhanced bacterial sensitivity to SDS-EDTA, we may consider them as defects, locally disrupting the OM barrier function.

Another, more preliminary, OM feature was the unexpected observation of ruffles at the division site. Although this result provides many avenues for exploration, the first must be to determine whether this ruffling is an artefact of immobilisation, since this must lead to some reduced ability to reorganise the membrane. Crudely, this could be done by fixing cells and imaging to see if ruffles remain, however fixation can extensively damage membranes so may not be appropriate. Alternatively, cells could be imaged rapidly after immobilisation to find those that were already undergoing division before adhesion. The rapidity and effect of gene deletions, for example *ToIA*<sup>163</sup>, on ruffle formation are also open questions.

Finally, in Chapter 6, the combination of AFM with fluorescence microscopy has shown it can provide fresh insight into biological problems: finding the clustering behaviour of MACs and an unusual destabilisation effect on the OM. The sudden destabilisation of the OM by MAC was a surprising effect that is not universal in membrane targeting compounds, shown by the maintained integrity of cells killed by the antimicrobial peptide, melittin.

In the future, correlating MAC induced cell death with overall cell stiffness would provide more evidence that the MAC leads to OM destabilisation, providing a potential mechanism by which MAC permeates the entire, multilayer bacterial cell envelope. It would also be informative to see if cell stiffness decreases gradually or suddenly before cell death.

An important unsolved problem regarding the MAC is the difference in time to MAC lysis between cells. Particularly, as shown here, some cells survive with many MACs in their surface for long time periods. Potentially, in some parts of the membrane the MAC has a greater effect and to test this, cells could be imaged to find MAC locations which could then be correlated with time to lysis. The varying severity of MAC insertion could also be due heterologous membrane stability in the cell population, and this could be tested by measuring cell stiffness of untreated cells. It is also worth noting that this is not exclusive to the MAC, since AFM of other antimicrobials has also shown varied lysis times within a population<sup>95</sup>.

What is unusual about the MAC is that it exclusively targets the OM, with no formation on the inner membrane. While many AMPs target the OM, they also affect the inner membrane. The only examples of other antimicrobials that act this way are the recently developed BamA-targeting small molecule antibiotics and antibodies<sup>6,58,59,176</sup> and it would be interesting to see if this destabilisation effect is also seen there.

In summary, by the application of high-end and high-resolution AFM methods to live *E. coli*, this thesis has revealed several new features of the OM, and provides a wide perspective for a wide range of other research directions to be pursued.

# Bibliography

1. Tacconelli E. and Margrini N. *Global priority list of antibiotic-resistant bacteria to guide research, discovery, and development of new antibiotics*. WHO (2017). doi:10.1590/S0100-15742013000100018
2. Silhavy, T. J., Kahne, D. & Walker, S. The bacterial cell envelope. *Cold Spring Harb Perspect Biol* (2010). doi:10.1101/cshperspect.a000414
3. Plackett, B. Why big pharma has abandoned antibiotics. *Nature* **586**, S50–S52 (2020).
4. Surette, M. D. & Wright, G. D. Lessons from the Environmental Antibiotic Resistome. *Annu. Rev. Microbiol.* **71**, 309–329 (2017).
5. Savage, N. How researchers are revamping antimicrobial drugs. *Nature* **586**, S55–S56 (2020).
6. Luther, A., Urfer, M., Zahn, M., Müller, M., Wang, S.-Y. Y., Mondal, M., Vitale, A., Hartmann, J.-B. B., Sharpe, T., Monte, F. Lo, Kocherla, H., Cline, E., Pessi, G., Rath, P., Modaresi, S. M., Chiquet, P., Stiegeler, S., Verbree, C., Remus, T., Schmitt, M., Kolopp, C., Westwood, M.-A. A., Desjonquères, N., Brabet, E., Hell, S., LePoupon, K., Vermeulen, A., Jaisson, R., Rithié, V., Upert, G., Lederer, A., Zbinden, P., Wach, A., Moehle, K., Zerbe, K., Locher, H. H., Bernardini, F., Dale, G. E., Eberl, L., Wollscheid, B., Hiller, S., Robinson, J. A. & Obrecht, D. Chimeric peptidomimetic antibiotics against Gram-negative bacteria. *Nature* **576**, 452–458 (2019).
7. Tommasi, R., Brown, D. G., Walkup, G. K., Manchester, J. I. & Miller, A. A. *ESKAPeIng the labyrinth of antibacterial discovery*. *Nat. Rev. Drug Discov.* **14**, (2015).
8. Beveridge, T. J. Structure of gram-negative cell walls and their derived membrane vesicles. *J. Bacteriol.* **181**, 4725–4733 (1999).
9. Rosenbusch, J. P. Characterization of the Major Envelope Protein from *Escherichia coli*. *J. Biol. Chem.* **249**, 8010–8029 (1974).

10. Nikaido, H. Molecular basis of bacterial outer membrane permeability revisited. *Microbiol. Mol. Biol. Rev.* **67**, 593–656 (2003).
11. Kamio, Y. & Nikaido, H. Outer Membrane of Salmonella Typhimurium: Accessibility of Phospholipid Head Groups to Phospholipase C and Cyanogen Bromide Activated Dextran in the External Medium. *Biochemistry* **15**, 2561–2570 (1976).
12. Jones, N. C. & Osborn, M. J. Translocation of phospholipids between the outer and inner membranes of Salmonella typhimurium. *J. Biol. Chem.* **252**, 7405–7412 (1977).
13. Sutterlin, H. A., Shi, H., May, K. L., Miguel, A., Khare, S., Huang, K. C. & Silhavy, T. J. Disruption of lipid homeostasis in the Gram-negative cell envelope activates a novel cell death pathway. *Proc. Natl. Acad. Sci. U. S. A.* **113**, E1565–E1574 (2016).
14. Ekiert, D. C., Bhabha, G., Isom, G. L., Greenan, G., Ovchinnikov, S., Henderson, I. R., Cox, J. S. & Vale, R. D. Architectures of Lipid Transport Systems for the Bacterial Outer Membrane. *Cell* **169**, 273-285.e17 (2017).
15. Konovalova, A. & Silhavy, T. J. Outer membrane lipoprotein biogenesis: Lol is not the end. *Philos. Trans. R. Soc. B Biol. Sci.* **370**, (2015).
16. Mathelié-Guinlet, M., Asmar, A. T., Collet, J.-F. & Dufrêne, Y. F. Lipoprotein Lpp regulates the mechanical properties of the E. coli cell envelope. *Nat. Commun.* **11**, 1789 (2020).
17. Grimm, J., Shi, H., Wang, W., Mitchell, A. M., Wingreen, N. S., Huang, K. C. & Silhavy, T. J. The inner membrane protein YhdP modulates the rate of anterograde phospholipid flow in Escherichia coli. *Proc. Natl. Acad. Sci. U. S. A.* **117**, 26907–26914 (2020).
18. Malinverni, J. C. & Silhavy, T. J. An ABC transport system that maintains lipid asymmetry in the Gram-negative outer membrane. *Proc. Natl. Acad. Sci. U. S. A.* **106**, 8009–8014 (2009).

19. Abellón-Ruiz, J., Kaptan, S. S., Baslé, A., Claudi, B., Bumann, D., Kleinekathöfer, U. & Van Den Berg, B. Structural basis for maintenance of bacterial outer membrane lipid asymmetry. *Nat. Microbiol.* **2**, 1616–1623 (2017).
20. May, K. L. & Silhavy, T. J. The Escherichia coli Phospholipase PldA Regulates Outer Membrane Homeostasis via Lipid Signaling. *MBio* **9**, (2018).
21. Guest, R. L., Rutherford, S. T. & Silhavy, T. J. Border Control: Regulating LPS Biogenesis. *Trends Microbiol.* 1–12 (2020). doi:10.1016/j.tim.2020.09.008
22. Reeves, P. R. & Cunneen, M. M. in *Microb. Glycobiol.* 319–335 (Elsevier, 2009). at <<http://dx.doi.org/10.1016/B978-0-1237-4546-0.00018-3>>
23. Okuda, S., Sherman, D. J., Silhavy, T. J., Ruiz, N. & Kahne, D. Lipopolysaccharide transport and assembly at the outer membrane: The PEZ model. *Nat. Rev. Microbiol.* **14**, 337–345 (2016).
24. Jefferies, D., Shearer, J. & Khalid, S. Role of O-Antigen in Response to Mechanical Stress of the E. coli Outer Membrane: Insights from Coarse-Grained MD Simulations. *J. Phys. Chem. B* **123**, 3567–3575 (2019).
25. Rassam, P., Long, K. R., Kaminska, R., Williams, D. J., Papadakos, G., Baumann, C. G. & Kleanthous, C. Intermembrane crosstalk drives inner-membrane protein organization in Escherichia coli. *Nat. Commun.* **9**, (2018).
26. Ortiz-Suarez, M. L., Samsudin, F., Piggot, T. J., Bond, P. J. & Khalid, S. Full-Length OmpA: Structure, Function, and Membrane Interactions Predicted by Molecular Dynamics Simulations. *Biophys. J.* **111**, 1692–1702 (2016).
27. Gunasinghe, S. D., Shiota, T., Stubenrauch, C. J., Schulze, K. E., Webb, C. T., Fulcher, A. J., Dunstan, R. A., Hay, I. D., Naderer, T., Whelan, D. R., Bell, T. D. M., Elgass, K. D., Strugnell, R. A. & Lithgow, T. The WD40 Protein BamB Mediates Coupling of BAM Complexes into Assembly Precincts in the Bacterial Outer Membrane. *Cell Rep.* **23**, 2782–2794 (2018).
28. Rollauer, S. E., Soorshjani, M. A., Noinaj, N. & Buchanan, S. K. Outer membrane protein biogenesis in Gram-negative bacteria. *Philos. Trans. R. Soc.*

- B Biol. Sci.* **370**, (2015).
29. Mitchell, A. M. & Silhavy, T. J. Envelope stress responses: balancing damage repair and toxicity. *Nat. Rev. Microbiol.* **17**, 417–428 (2019).
  30. Horne, J. E., Brockwell, D. J. & Radford, S. E. Role of the lipid bilayer in outer membrane protein folding in Gram-negative bacteria. *J. Biol. Chem.* **295**, 10340–10367 (2020).
  31. Ricci, D. P. & Silhavy, T. J. in *Protein Secret. Bact.* (ed. Maria Sandkvist, Eric Cascales, P. J. C.) 91–101 (American Society for Microbiology, 2019). doi:10.1128/ecosalplus.esp-0035-2018
  32. Kleanthous, C., Rassam, P. & Baumann, C. G. Protein-protein interactions and the spatiotemporal dynamics of bacterial outer membrane proteins. *Curr. Opin. Struct. Biol.* **35**, 109–115 (2015).
  33. Ritchie, K., Lill, Y., Sood, C., Lee, H. & Zhang, S. Single-molecule imaging in live bacteria cells. *Philos. Trans. R. Soc. B Biol. Sci.* **368**, (2013).
  34. Spector, J., Zakharov, S., Lill, Y., Sharma, O., Cramer, W. A. & Ritchie, K. Mobility of BtuB and OmpF in the Escherichia coli outer membrane: Implications for dynamic formation of a translocon complex. *Biophys. J.* **99**, 3880–3886 (2010).
  35. Mika, J. T. & Poolman, B. Macromolecule diffusion and confinement in prokaryotic cells. *Curr. Opin. Biotechnol.* **22**, 117–126 (2011).
  36. Chavent, M., Duncan, A. L., Rassam, P., Birkholz, O., Hélie, J., Reddy, T., Beliaev, D., Hambly, B., Piehler, J., Kleanthous, C. & Sansom, M. S. P. How nanoscale protein interactions determine the mesoscale dynamic organisation of bacterial outer membrane proteins. *Nat. Commun.* **9**, (2018).
  37. Yamashita, H., Taoka, A., Uchihashi, T., Asano, T., Ando, T. & Fukumori, Y. Single-molecule imaging on living bacterial cell surface by high-speed AFM. *J. Mol. Biol.* **422**, 300–309 (2012).
  38. Rassam, P., Copeland, N. A., Birkholz, O., Tóth, C., Chavent, M., Duncan, A. L., Cross, S. J., Housden, N. G., Kaminska, R., Seger, U., Quinn, D. M., Garrod, T. J.,

- Sansom, M. S. P., Piehler, J., Baumann, C. G. & Kleanthous, C. Supramolecular assemblies underpin turnover of outer membrane proteins in bacteria. *Nature* **523**, 333–336 (2015).
39. Casuso, I., Khao, J., Chami, M., Paul-Gilloteaux, P., Husain, M., Duneau, J. P., Stahlberg, H., Sturgis, J. N. & Scheuring, S. Characterization of the motion of membrane proteins using high-speed atomic force microscopy. *Nat. Nanotechnol.* **7**, 525–529 (2012).
  40. Ghosh, A. S. & Young, K. D. Helical disposition of proteins and lipopolysaccharide in the outer membrane of Escherichia coli. *J. Bacteriol.* **187**, 1913–1922 (2005).
  41. Rothenberg, E., Sepúlveda, L. A., Skinner, S. O., Zeng, L., Selvin, P. R. & Golding, I. Single-virus tracking reveals a spatial receptor-dependent search mechanism. *Biophys. J.* **100**, 2875–2882 (2011).
  42. De Pedro, M. A., Grünfelder, C. G. & Schwarz, H. Restricted Mobility of Cell Surface Proteins in the Polar Regions of Escherichia coli. *J. Bacteriol.* **186**, 2594–2602 (2004).
  43. Gibbs, K. A., Isaac, D. D., Xu, J., Hendrix, R. W., Silhavy, T. J. & Theriot, J. A. Complex spatial distribution and dynamics of an abundant Escherichia coli outer membrane protein, LamB. *Mol. Microbiol.* **53**, 1771–1783 (2004).
  44. Ursell, T. S., Trepagnier, E. H., Huang, K. C. & Theriot, J. A. Analysis of Surface Protein Expression Reveals the Growth Pattern of the Gram-Negative Outer Membrane. *PLoS Comput. Biol.* **8**, 1002680 (2012).
  45. Mamou, G., Inns, P. G., Sun, D., Kaminska, R., Housden, N. G., Cohen-Khait, R., Miller, H., Storek, K. M., Rutherford, S. T., Payandeh, J. & Kleanthous, C. Spatiotemporal organization of BamA governs the pattern of outer membrane protein distribution in growing Escherichia coli cells. *bioRxiv* 2021.01.27.428258 (2021). at <<https://doi.org/10.1101/2021.01.27.428258>>
  46. Bayer, M. E. & Leive, L. Effect of ethylenediaminetetraacetate upon the surface of Escherichia coli. *J. Bacteriol.* **130**, 1364–1381 (1977).

47. Jarosławski, S., Duquesne, K., Sturgis, J. N. & Scheuring, S. High-resolution architecture of the outer membrane of the Gram-negative bacteria *Roseobacter denitrificans*. *Mol. Microbiol.* **74**, 1211–1222 (2009).
48. Chandler, D. E. & Sharp, W. P. in *Electron Microsc. Methods Protoc.* (ed. Kuo, J.) **1117**, 95–132 (Humana Press, 2014).
49. Bayer, M. E. & Remsen, C. Structure of *Escherichia coli* after freeze-etching. *J. Bacteriol.* **101**, 304–313 (1970).
50. Van Alphen, L., Verkleij, A., Leunissen Bijvelt, J. & Lugtenberg, B. Architecture of the outer membrane of *Escherichia coli*. III. Protein-lipopolysaccharide complexes in intramembraneous particles. *J. Bacteriol.* **134**, 1089–1098 (1978).
51. Lugtenberg, B. & Alphen, L. V. Molecular Architecture and Functioning of the Outer Membrane of *Escherichia coli* and other Gram-negative Bacteria. *Biochim. Biophys. Acta* **737**, 51–115 (1983).
52. Oestreicher, Z., Taoka, A. & Fukumori, Y. A comparison of the surface nanostructure from two different types of gram-negative cells: *Escherichia coli* and *Rhodobacter sphaeroides*. *Micron* **72**, 8–14 (2015).
53. Heesterbeek, D. A., Bardoel, B. W., Parsons, E. S., Bennett, I., Ruyken, M., Doorduyn, D. J., Gorham, R. D., Berends, E. T., Pyne, A. L., Hoogenboom, B. W. & Rooijackers, S. H. M. Bacterial killing by complement requires membrane attack complex formation via surface-bound C5 convertases. *EMBO J.* e99852 (2019). doi:10.15252/embj.201899852
54. Benn, G., Pyne, A. L., Ryadnov, M. G. & Hoogenboom, B. W. Imaging live bacteria at the nanoscale: comparison of immobilisation strategies. *Analyst* 1–15 (2019). doi:10.1039/c9an01185d
55. Brown, D. G. Drug discovery strategies to outer membrane targets in Gram-negative pathogens. *Bioorganic Med. Chem.* **24**, 6320–6331 (2016).
56. MacNair, C. R., Tsai, C. N. & Brown, E. D. Creative targeting of the Gram-

- negative outer membrane in antibiotic discovery. *Ann. N. Y. Acad. Sci.* **1459**, 69–85 (2020).
57. Martin-Loeches, I., Dale, G. E. & Torres, A. Murepavadin: a new antibiotic class in the pipeline. *Expert Rev. Anti. Infect. Ther.* **16**, 259–268 (2018).
  58. Imai, Y., Meyer, K. J., Iinishi, A., Favre-Godal, Q., Green, R., Manuse, S., Caboni, M., Mori, M., Niles, S., Ghiglieri, M., Honrao, C., Ma, X., Guo, J. J., Makriyannis, A., Linares-Otoya, L., Böhringer, N., Wuisan, Z. G., Kaur, H., Wu, R., Mateus, A., Typas, A., Savitski, M. M., Espinoza, J. L., O'Rourke, A., Nelson, K. E., Hiller, S., Noinaj, N., Schäberle, T. F., D'Onofrio, A. & Lewis, K. A new antibiotic selectively kills Gram-negative pathogens. *Nature* **576**, 459–464 (2019).
  59. Hart, E. M., Mitchell, A. M., Konovalova, A., Grabowicz, M., Sheng, J., Han, X., Rodriguez-Rivera, F. P., Schwaid, A. G., Malinverni, J. C., Balibar, C. J., Bodea, S., Si, Q., Wang, H., Homsher, M. F., Painter, R. E., Ogawa, A. K., Sutterlin, H., Roemer, T., Black, T. A., Rothman, D. M., Walker, S. S. & Silhavy, T. J. A small-molecule inhibitor of BamA impervious to efflux and the outer membrane permeability barrier. *Proc. Natl. Acad. Sci. U. S. A.* **116**, 21748–21757 (2019).
  60. Nguyen, L. T., Haney, E. F. & Vogel, H. J. The expanding scope of antimicrobial peptide structures and their modes of action. *Trends Biotechnol.* **29**, 464–472 (2011).
  61. Hurdle, J. G., O'Neill, A. J., Chopra, I. & Lee, R. E. Targeting bacterial membrane function: An underexploited mechanism for treating persistent infections. *Nat. Rev. Microbiol.* **9**, 62–75 (2011).
  62. Yang, Z., Choi, H. & Weisshaar, J. C. Melittin-Induced Permeabilization, Re-sealing, and Re-permeabilization of E. coli Membranes. *Biophysj* **114**, 368–379 (2018).
  63. Hammond, K., Ryadnov, M. G. & Hoogenboom, B. W. Atomic force microscopy to elucidate how peptides disrupt membranes. *Biochim. Biophys. Acta - Biomembr.* **1863**, 183447 (2021).
  64. Wimley, W. C. Describing the Mechanism of Antimicrobial Peptide Action with

- the Interfacial Activity Model. *ACS Chem Biol.* **5**, 905–917 (2010).
65. Murphy, K. *Janeway's Immunobiology.* (Garland Science, 2011). doi:10.1007/s13398-014-0173-7.2
  66. Jennings, C., Kusler, B. & Jones, P. P. in *Mol. Biol. Cell* (Garland Science, 2002). doi:10.1177/1753425908100928
  67. Wills-Karp, M. Complement Activation Pathways: A Bridge between Innate and Adaptive Immune Responses in Asthma. *Proc Am Thorac Soc* **4**, 247–251 (2007).
  68. Schaller, J., Gerber, S., Kmpfer, U., Lejon, S. & Trachsel, C. *Human Blood Plasma Proteins.* (John Wiley & Sons Ltd, 2008). doi:10.1002/9780470724378
  69. Hajishengallis, G., Reis, E. S., Mastellos, D. C., Ricklin, D. & Lambris, J. D. Novel mechanisms and functions of complement. *Nat. Immunol.* **18**, 1288–1298 (2017).
  70. Sharp, T. H., Koster, A. J. & Gros, P. Heterogeneous MAC Initiator and Pore Structures in a Lipid Bilayer by Phase-Plate Cryo-electron Tomography. *Cell Rep.* **15**, 1–8 (2016).
  71. Aleshin, A. E., DiScipio, R. G., Stec, B. & Liddington, R. C. Crystal structure of C5b-6 suggests structural basis for priming assembly of the membrane attack complex. *J. Biol. Chem.* **287**, 19642–19652 (2012).
  72. Menny, A., Serna, M., Boyd, C. M., Gardner, S., Praveen Joseph, A., Paul Morgan, B., Topf, M., Brooks, N. J. & Bubeck, D. CryoEM reveals how the complement membrane attack complex ruptures lipid bilayers. *Nat. Commun.* **9**, 5316 (2018).
  73. Doorduijn, D. J., Bardoel, B. W., Heesterbeek, D. A. C., Ruyken, M., Benn, G., Parsons, E. S., Hoogenboom, B. W. & Suzan, S. H. Bacterial killing by complement requires direct anchoring of membrane attack complex precursor C5b-7. *PLoS Pathog.* **16**, (2020).
  74. Serna, M., Giles, J. L., Morgan, B. P. & Bubeck, D. Structural basis of

- complement membrane attack complex formation. *Nat. Commun.* **7**, 10587 (2016).
75. Bubeck, D. The making of a macromolecular machine: Assembly of the membrane attack complex. *Biochemistry* **53**, 1908–1915 (2014).
  76. Berends, E. T., Dekkers, J. F., Nijland, R., Kuipers, A., Soppe, J. A., van Strijp, J. A. & Rooijackers, S. H. Distinct localization of the complement C5b-9 complex on Gram-positive bacteria. *Cell. Microbiol.* **15**, 1955–1968 (2013).
  77. Parsons, E. S., Stanley, G. J., Pyne, A. L., Hodel, A. W., Nievergelt, A. P., Menny, A., Yon, A. R., Rowley, A., Richter, R. P., Fantner, G. E., Bubeck, D. & Hoogenboom, B. W. Single-molecule kinetics of pore assembly by the membrane attack complex. *Nat. Commun.* **10**, 2066 (2019).
  78. Dudkina, N. V, Spicer, B. A., Reboul, C. F., Conroy, P. J., Lukoyanova, N., Elmlund, H., Law, R. H. P., Ekkel, S. M., Kondos, S. C., Goode, R. J. A., Ramm, G., Whisstock, J. C., Saibil, H. R. & Dunstone, M. A. Structure of the poly-C9 component of the complement membrane attack complex. *Nat. Commun.* **7**, 10588 (2016).
  79. Bayly-Jones, C., Bubeck, D. & Dunstone, M. A. The mystery behind membrane insertion: A review of the complement membrane attack complex. *Philos. Trans. R. Soc. B Biol. Sci.* **372**, (2017).
  80. Delisi, C., Boyle, M. & Borsos, T. Analysis of the colloid osmotic step of complement-mediated immune hemolysis. *J. Immunol.* **125**, 2055–2062 (1980).
  81. Turner, R. D., Hurd, A. F., Cadby, A., Hobbs, J. K. & Foster, S. J. Cell wall elongation mode in Gram-negative bacteria is determined by peptidoglycan architecture. *Nat. Commun.* **4**, (2013).
  82. Glynn, A. A. & Milne, C. M. Lysozyme and immune bacteriolysis. *Nature* **207**, 1309–1310 (1965).
  83. Heesterbeek, D. A. C., Muts, R. M., van Hensbergen, V. P., de Saint Aulaire, P.,

- Wennekes, T., Bardoel, B. W., van Sorge, N. M. & Rooijackers, S. H. M. Outer membrane permeabilization by the membrane attack complex sensitizes Gram-negative bacteria to antimicrobial proteins in serum and phagocytes. *PLoS Pathog.* **17**, (2021).
84. Binnig, G., Quate, C. F. & Gerber, C. Atomic force microscope. *Phys. Rev. Lett.* **56**, 930–933 (1986).
  85. Parot, P., Dufrene, Y. F., Hinterdorfer, P., Grimellec, C. Le, Navajas, D., Pellequer, J.-L. & Scheuring, S. Past, present and future of atomic force microscopy in life sciences and medicine. *J. Mol. Recognit.* **20**, 418–431 (2007).
  86. Dupres, V., Alsteens, D., Pauwels, K. & Dufrêne, Y. F. In vivo imaging of S-layer nanoarrays on *Corynebacterium glutamicum*. *Langmuir* **25**, 9653–9655 (2009).
  87. Kailas, L., Ratcliffe, E. C., Hayhurst, E. J., Walker, M. G., Foster, S. J. & Hobbs, J. K. Immobilizing live bacteria for AFM imaging of cellular processes. *Ultramicroscopy* **109**, 775–780 (2009).
  88. Touhami, A., Jericho, M. H. & Beveridge, T. J. Atomic force microscopy of cell growth and division in *Staphylococcus aureus*. *J. Bacteriol.* **186**, 3286–3295 (2004).
  89. Bailey, R. G., Turner, R. D., Mullin, N., Clarke, N., Foster, S. J. & Hobbs, J. K. The interplay between cell wall mechanical properties and the cell cycle in *staphylococcus aureus*. *Biophys. J.* **107**, 2538–2545 (2014).
  90. Andre, G., Kulakauskas, S., Chapot-Chartier, M. P., Navet, B., Deghorain, M., Bernard, E., Hols, P. & Dufrêne, Y. F. Imaging the nanoscale organization of peptidoglycan in living *Lactococcus lactis* cells. *Nat. Commun.* **1**, (2010).
  91. Saar Dover, R., Bitler, A., Shimoni, E., Trieu-Cuot, P. & Shai, Y. Multiparametric AFM reveals turgor-responsive net-like peptidoglycan architecture in live streptococci. *Nat. Commun.* **6**, 1–10 (2015).
  92. Pasquina-Lemonche, L., Burns, J., Turner, R. D., Kumar, S., Tank, R., Mullin, N.,

- Wilson, J. S., Chakrabarti, B., Bullough, P. A., Foster, S. J. & Hobbs, J. K. The architecture of the Gram-positive bacterial cell wall. *Nature* **582**, 294–297 (2020).
93. Plomp, M., Leighton, T. J., Wheeler, K. E., Hill, H. D. & Malkin, A. J. In vitro high-resolution structural dynamics of single germinating bacterial spores. *Proc. Natl. Acad. Sci. U. S. A.* **104**, 9644–9649 (2007).
94. Hannebelle, M. T. M., Ven, J. X. Y., Toniolo, C., Eskandarian, H. A., Vuaridel-Thurre, G., McKinney, J. D. & Fantner, G. E. A biphasic growth model for cell pole elongation in mycobacteria. *Nat. Commun.* **11**, (2020).
95. Fantner, G. E., Barbero, R. J., Gray, D. S. & Belcher, A. M. Kinetics of antimicrobial peptide activity measured on individual bacterial cells using high-speed atomic force microscopy. *Nat. Nanotechnol.* **5**, 280–285 (2010).
96. Lyubchenko, Y. L. *Nanoscale Imaging Methods and Protocols Methods in Molecular Biology*. (2012). doi:<https://doi.org/10.1007/978-1-4939-8591-3>
97. Eskandarian, H. A., Odermatt, P. D., Ven, J. X., Hannebelle, M. T., Nievergelt, A. P., Dhar, N., McKinney, J. D. & Fantner, G. E. Division site selection linked to inherited cell surface wave troughs in mycobacteria. *Nat. Microbiol.* **2**, 17094 (2017).
98. Odermatt, P. D., Hannebelle, M. T. M., Eskandarian, H. A., Nievergelt, A. P., McKinney, J. D. & Fantner, G. E. Overlapping and essential roles for molecular and mechanical mechanisms in mycobacterial cell division. *Nat. Phys.* **16**, 57–62 (2020).
99. Lin, Y. C., Huang, C. & Lai, H. C. Revealing the ultrastructure of the membrane pores of intact *Serratia marcescens* cells by atomic force microscopy. *Heliyon* **5**, (2019).
100. Amro, N. A., Kotra, L. P., Wadu-Mesthrige, K., Bulychev, A., Mobashery, S. & Liu, G. Y. High-resolution atomic force microscopy studies of the *Escherichia coli* outer membrane: structural basis for permeability. *Langmuir* **16**, 2789–2796 (2000).

101. Li, A., Lee, P. Y., Ho, B., Ding, J. L. & Lim, C. T. Atomic force microscopy study of the antimicrobial action of Sushi peptides on Gram negative bacteria. *Biochim. Biophys. Acta* **1768**, 411–418 (2007).
102. Quilès, F., Barth, D., Peric, O., Fantner, G. E. & Francius, G. Parietal Structures of Escherichia coli Can Impact the D-Cateslytin Antibacterial Activity. *ACS Chem. Biol.* **15**, 2801–2814 (2020).
103. Overton, K., Greer, H. M., Ferguson, M. A., Spain, E. M., Elmore, D. E., Núñez, M. E. & Volle, C. B. Qualitative and Quantitative Changes to Escherichia coli during Treatment with Magainin 2 Observed in Native Conditions by Atomic Force Microscopy. *Langmuir* **36**, 650–659 (2020).
104. Maggi, S., Yabre, K., Ferrari, A., Lazzi, C., Kawano, M., Rivetti, C. & Folli, C. Functional characterization of the type I toxin Lpt from Lactobacillus rhamnosus by fluorescence and atomic force microscopy. *Sci. Rep.* **9**, (2019).
105. Peric, O., Hannebelle, M., Adams, J. D. & Fantner, G. E. Microfluidic bacterial traps for simultaneous fluorescence and atomic force microscopy. *Nano Res.* **1**, 1–13 (2017).
106. Guyer, M. S., Reed, R. R., Steitz, J. A. & Low, K. B. Identification of a sex-factor-affinity site in E. coli as gamma delta. *Cold Spring Harb. Symp. Quant. Biol.* **45**, 135–140 (1981).
107. Benn, G., Mikheyeva, I. V., Inns, P. G., Forster, J. C., Ojkic, N., Bortolini, C., Ryadnov, M. G., Kleanthous, C., Silhavy, T. J. & Hoogenboom, B. W. Phase separation in the outer membrane of Escherichia coli. *Proc. Natl. Acad. Sci.* **118**, e2112237118 (2021).
108. Beall, B. & Lutkenhaus, J. Sequence analysis, transcriptional organization, and insertional mutagenesis of the envA gene of Escherichia coli. *J. Bacteriol.* **169**, 5408–5415 (1987).
109. Guest, R. L., Guerra, D. S., Wissler, M., Grimm, J. & Silhavy, T. J. YejM modulates activity of the YciM/FtsH protease complex to prevent lethal accumulation of lipopolysaccharide. *MBio* **11**, 1–13 (2020).

110. Baba, T., Ara, T., Hasegawa, M., Takai, Y., Okumura, Y., Baba, M., Datsenko, K. A., Tomita, M., Wanner, B. L. & Mori, H. Construction of Escherichia coli K-12 in-frame, single-gene knockout mutants: The Keio collection. *Mol. Syst. Biol.* **2**, (2006).
111. Ghosh, R., Steiert, M., Hardmeyer, A., Wang, Y. F. & Rosenbusch, J. P. Overexpression of outer membrane porins in E. coli using pBluescript- derived vectors. *Gene Expr.* **7**, 149–161 (1998).
112. Cherepanov, P. P. & Wackernagel, W. Gene disruption in Escherichia coli: TcR and KmR cassettes with the option of Flp-catalyzed excision of the antibiotic-resistance determinant. *Gene* **158**, 9–14 (1995).
113. Guzman, L. M., Belin, D., Carson, M. J. & Beckwith, J. Tight regulation, modulation, and high-level expression by vectors containing the arabinose P(BAD) promoter. *J. Bacteriol.* **177**, 4121–4130 (1995).
114. Verhoeven, G. S., Alexeeva, S., Dogterom, M. & den Blaauwen, T. Differential bacterial surface display of peptides by the transmembrane domain of OmpA. *PLoS One* **4**, 6739 (2009).
115. Allison, D. P., Sullivan, C. J., Mortensen, N. P., Retterer, S. T. & Doktycz, M. Bacterial Immobilization for Imaging by Atomic Force Microscopy. *J. Vis. Exp.* **54**, (2011).
116. Jansen, K. B., Inns, P. G., Housden, N. G., Hopper, J. T. S., Kaminska, R., Lee, S., Robinson, C. V, Bayley, H. & Kleanthous, C. Bifurcated binding of the OmpF receptor underpins import of the bacteriocin colicin N into Escherichia coli. *J. Biol. Chem.* **295**, 9147–9156 (2020).
117. *JPK DP Data Processing Software Manual Version 6.0.* (2017).
118. Smolyakov, G., Formosa-Dague, C., Severac, C., Duval, R. & Dague, E. High speed indentation measures by FV, QI and QNM introduce a new understanding of bionanomechanical experiments. *Micron* **85**, 8–14 (2016).
119. Pyne, A. L., Thompson, R., Leung, C., Roy, D. & Hoogenboom, B. W. Single-

- molecule reconstruction of oligonucleotide secondary structure by atomic force microscopy. *Small* **10**, 3257–3261 (2014).
120. Morris, V. J., Kirby, A. R. & Gunning, A. P. *Atomic Force Microscopy for Biologists*. (IMPERIAL COLLEGE PRESS, 2009). doi:10.1142/p674
  121. Astrom, K. J. & Murray, R. M. in *Feed. Syst. An Introd. Sci. Eng.* 293–314 (2019). at <<http://www.cds.caltech.edu/~murray/amwiki>>
  122. García, R. & Pérez, R. Dynamic atomic force microscopy methods. *Surf. Sci. Rep.* **47**, 197–301 (2002).
  123. Pyne, A. L. High Resolution Atomic Force Microscopy of Functional Biological Molecules. (2015).
  124. JPK. NanoWizard® AFM User Manual Version 4.2. (2012).
  125. Hutter, J. L. & Bechhoefer, J. Calibration of atomic-force microscope tips. *Rev. Sci. Instrum.* **64**, 1868–1873 (1993).
  126. Schindelin, J., Arganda-Carreras, I., Frise, E., Kaynig, V., Longair, M., Pietzsch, T., Preibisch, S., Rueden, C., Saalfeld, S., Schmid, B., Tinevez, J. Y., White, D. J., Hartenstein, V., Eliceiri, K., Tomancak, P. & Cardona, A. Fiji: An open-source platform for biological-image analysis. *Nat. Methods* **9**, 676–682 (2012).
  127. Nečas, D. & Klapetek, P. Gwyddion: An open-source software for SPM data analysis. *Cent. Eur. J. Phys.* **10**, 181–188 (2012).
  128. Beton, J. G., Moorehead, R., Helfmann, L., Gray, R., Hoogenboom, B. W., Joseph, A. P., Topf, M. & Pyne, A. L. B. TopoStats – A program for automated tracing of biomolecules from AFM images. *Methods* (2021). doi:10.1016/j.ymeth.2021.01.008
  129. Chopinet, L., Formosa, C., Rols, M. P., Duval, R. E. & Dague, E. Imaging living cells surface and quantifying its properties at high resolution using AFM in QI™ mode. *Micron* **48**, 26–33 (2013).
  130. Shibata, M., Watanabe, H., Uchihashi, T., Ando, T. & Yasuda, R. High-speed atomic force microscopy imaging of live mammalian cells. *Biophys.*

- Physicobiology* **14**, 127–135 (2017).
131. Shi, H., Liu, Z., Li, A., Yin, J., Chong, A. G. L., Tan, K. S. W., Zhang, Y. & Lim, C. T. Life Cycle-Dependent Cytoskeletal Modifications in *Plasmodium falciparum* Infected Erythrocytes. *PLoS One* **8**, 1–10 (2013).
  132. Nowakowski, R., Luckham, P. & Winlove, P. Imaging erythrocytes under physiological conditions by atomic force microscopy. *Biochim. Biophys. Acta - Biomembr.* **1514**, 170–176 (2001).
  133. Ando, T., Kodera, N., Takai, E., Maruyama, D., Saito, K. & Toda, A. A High-speed Atomic Force Microscope for Studying Biological Macromolecules. *Proc. Natl. Acad. Sci. U. S. A.* **98**, 12468–12472 (2001).
  134. Louise Meyer, R., Zhou, X., Tang, L., Arpanaei, A., Kingshott, P. & Besenbacher, F. Immobilisation of living bacteria for AFM imaging under physiological conditions. *Ultramicroscopy* **110**, 1349–1357 (2010).
  135. Li, M., Dang, D., Xi, N., Wang, Y. & Liu, L. Nanoscale imaging and force probing of biomolecular systems using atomic force microscopy: from single molecules to living cells. *Nanoscale* **9**, 17643–17666 (2017).
  136. Lonergan, N. E., Britt, L. D. & Sullivan, C. J. Immobilizing live *Escherichia coli* for AFM studies of surface dynamics. *Ultramicroscopy* **137**, 30–39 (2014).
  137. *Bd Cell-Tak™ Cell and Tissue Adhesive.* at [https://search.cosmobio.co.jp/cosmo\\_search\\_p/search\\_gate2/docs/CR\\_/354240.20070910.pdf](https://search.cosmobio.co.jp/cosmo_search_p/search_gate2/docs/CR_/354240.20070910.pdf)
  138. *VECTABOND™ Reagent Safety Data Sheet.* at [https://vectorlabs.com/amfile/file/download/file\\_id/3296/product\\_id/514/](https://vectorlabs.com/amfile/file/download/file_id/3296/product_id/514/)
  139. Sharma, S. & Conrad, J. C. Attachment from flow of *Escherichia coli* bacteria onto silanized glass substrates. *Langmuir* **30**, 11147–11155 (2014).
  140. Jeong, H., Barbe, V., Lee, C. H., Vallenet, D., Yu, D. S., Choi, S.-H., Couloux, A., Lee, S.-W., Yoon, S. H., Cattolico, L., Hur, C.-G., Park, H.-S., Ségurens, B., Kim,

- S. C., Oh, T. K., Lenski, R. E., Studier, F. W., Daegelen, P. & Kim, J. F. Genome Sequences of Escherichia coli B strains REL606 and BL21(DE3). *J. Mol. Biol.* **394**, 644–652 (2009).
141. Studier, F. W., Daegelen, P., Lenski, R. E., Maslov, S. & Kim, J. F. Understanding the Differences between Genome Sequences of Escherichia coli B Strains REL606 and BL21(DE3) and Comparison of the E. coli B and K-12 Genomes. *J. Mol. Biol.* **394**, 653–680 (2009).
142. Nyenhuis, D. A., Nilaweera, T. D., Niblo, J. K., Nguyen, N. Q., DuBay, K. H. & Cafiso, D. S. Evidence for the Supramolecular Organization of a Bacterial Outer-Membrane Protein from In Vivo Pulse Electron Paramagnetic Resonance Spectroscopy. *J. Am. Chem. Soc* (2020). doi:10.1021/jacs.0c01754
143. Rojas, E. R., Billings, G., Odermatt, P. D., Auer, G. K., Zhu, L., Miguel, A., Chang, F., Weibel, D. B., Theriot, J. A. & Huang, K. C. The outer membrane is an essential load-bearing element in Gram-negative bacteria. *Nature* **559**, 617–621 (2018).
144. Smith, S. G. J., Mahon, V., Lambert, M. A. & Fagan, R. P. A molecular Swiss army knife: OmpA structure, function and expression. *FEMS Microbiol. Lett.* **273**, 1–11 (2007).
145. Nikaido, H. & Vaara, M. Molecular basis of bacterial outer membrane permeability. *Microbiol. Rev.* **49**, 1–32 (1985).
146. Wang, Y. The function of OmpA in Escherichia coli. *Biochem. Biophys. Res. Commun.* **292**, 396–401 (2002).
147. S.W.Cowan, Cowan, S. W., Schirmer, T., Rummel, G., Steiert, M., Ghosh, R., Pauptit, R. A., Jansonius, J. N. & Rosenbusch, J. P. Crystal structures explain functional properties of two E. coli porins. *Nature* **358**, 727–733 (1992).
148. Sleytr, U., Thornley, M. J. & Glauert, A. M. Location of the fracture faces within the cell envelope of Acinetobacter species strain MJT/F5/5. *J. Bacteriol.* **118**, 693–707 (1974).

149. Dorset, D. L., Engel, A., Häner, M., Massalski, A. & Rosenbusch, J. P. Two-dimensional crystal packing of matrix porin. *J. Mol. Biol.* **165**, 701–710 (1983).
150. Sass, H. J., Büldt, G., Beckmann, E., Zemlin, F., van Heel, M., Zeitler, E., Rosenbusch, J. P., Dorset, D. L. & Massalski, A. Densely packed  $\beta$ -structure at the protein-lipid interface of porin is revealed by high-resolution cryo-electron microscopy. *J. Mol. Biol.* **209**, 171–175 (1989).
151. Simón, M., Mathes, A., Blanch, A. & Engelhardt, H. Characterization of a porin from the outer membrane of *Vibrio anguillarum*. *J. Bacteriol.* **178**, 4182–4188 (1996).
152. Schabert, F. A. & Engel, A. Reproducible acquisition of *Escherichia coli* porin surface topographs by atomic force microscopy. *Biophys. J.* **67**, 2394–2403 (1994).
153. Schabert, F. A., Henn, C. & Engel, A. Native *Escherichia coli* OmpF porin surfaces probed by atomic force microscopy. *Science (80-. )*. **268**, 92–94 (1995).
154. Cowan, S. W., Garavito, R. M., Jansonius, J. N., Jenkins, J. A., Karlsson, R., König, N., Pai, E. F., Pauptit, R. A., Rizkallah, P. J., Rosenbusch, J. P., Rummel, G. & Schirmer, T. The structure of OmpF porin in a tetragonal crystal form. *Structure* **3**, 1041–1050 (1995).
155. Taylor, R. K., Hall, M. N., Enquist, L. & Silhavy, T. J. Identification of OmpR: A positive regulatory protein controlling expression of the major outer membrane matrix porin proteins of *Escherichia coli* K-12. *J. Bacteriol.* **147**, 255–258 (1981).
156. Paracini, N., Clifton, L. A., Skoda, M. W. A. & Lakey, J. H. Liquid crystalline bacterial outer membranes are critical for antibiotic susceptibility. *Proc. Natl. Acad. Sci. U. S. A.* **115**, E7587–E7594 (2018).
157. Ando, T., Uchihashi, T. & Kodera, N. High-Speed AFM and Applications to Biomolecular. *Annu. Rev. Biophys* **42**, 393–414 (2013).

158. Shu, X., Shaner, N. C., Yarbrough, C. A., Tsien, R. Y. & Remington, S. J. Novel chromophores and buried charges control color in mFruits. *Biochemistry* **45**, 9639–9647 (2006).
159. Shearer, J., Jefferies, D. & Khalid, S. Outer Membrane Proteins OmpA, FhuA, OmpF, EstA, BtuB, and OmpX Have Unique Lipopolysaccharide Fingerprints. *J. Chem. Theory Comput.* **15**, 2608–2619 (2019).
160. Arunmanee, W., Pathania, M., Solovyova, A. S., Le Brun, A. P., Ridley, H., Baslé, A., Van Den Berg, B. & Lakey, J. H. Gram-negative trimeric porins have specific LPS binding sites that are essential for porin biogenesis. *Proc. Natl. Acad. Sci. U. S. A.* **113**, E5034–E5043 (2016).
161. Holdbrook, D. A., Huber, R. G., Piggot, T. J., Bond, P. J. & Khalid, S. Dynamics of crowded vesicles: Local and global responses to membrane composition. *PLoS One* **11**, (2016).
162. Egan, A. J. F. Bacterial outer membrane constriction. *Mol. Microbiol.* **107**, 676–687 (2018).
163. Szczepaniak, J., Holmes, P., Rajasekar, K., Kaminska, R., Samsudin, F., Inns, P. G., Rassam, P., Khalid, S., Murray, S. M., Redfield, C. & Kleanthous, C. The lipoprotein Pal stabilises the bacterial outer membrane during constriction by a mobilisation-and-capture mechanism. *Nat. Commun.* **11**, 112–114 (2020).
164. de Boer, P. A. J. Advances in understanding E. coli cell fission. *Curr. Opin. Microbiol.* **13**, 730–737 (2010).
165. Gerding, M. A., Ogata, Y., Pecora, N. D., Niki, H. & De Boer, P. A. J. The trans-envelope Tol-Pal complex is part of the cell division machinery and required for proper outer-membrane invagination during cell constriction in E. coli. *Mol. Microbiol.* **63**, 1008–1025 (2007).
166. Gunasinghe, S. D., Webb, C. T., Elgass, K. D., Hay, I. D. & Lithgow, T. Super-resolution imaging of protein secretion systems and the cell surface of Gram-negative bacteria. *Front. Cell. Infect. Microbiol.* **7**, 220 (2017).

167. Schindler, M., Osborn, M. J. & Koppel, D. E. Lateral diffusion of lipopolysaccharide in the outer membrane of *Salmonella typhimurium*. *Nature* **285**, 261–263 (1980).
168. Chong, Z. S., Woo, W. F. & Chng, S. S. Osmoporin OmpC forms a complex with MlaA to maintain outer membrane lipid asymmetry in *Escherichia coli*. *Mol. Microbiol.* **98**, 1133–1146 (2015).
169. Doorduyn, D. J., Rooijackers, S. H. M. & Heesterbeek, D. A. C. How the Membrane Attack Complex Damages the Bacterial Cell Envelope and Kills Gram-Negative Bacteria. *BioEssays* **1900074**, 1900074 (2019).
170. Grabowicz, M. & Silhavy, T. J. Envelope Stress Responses: An Interconnected Safety Net. *Trends Biochem. Sci.* **42**, 232–242 (2017).
171. Miajlovic, H. & Smith, S. G. Bacterial self-defence: How *Escherichia coli* evades serum killing. *FEMS Microbiol. Lett.* **354**, 1–9 (2014).
172. Mayer, M. M. Mechanism of Cytolysis by Complement (erythrocytes/leaky-patch model/doughnut model). *Proc. Natl. Acad. Sci.* **69**, 2954–2958 (1972).
173. Borsos, T., Dourmashkin, R. R. & Humphrey, J. H. Lesions in erythrocyte membranes caused by immune hæmolysis. *Nature* **202**, 251–252 (1964).
174. Berends, E. T., Kuipers, A., Ravesloot, M. M., Urbanus, R. T. & Rooijackers, S. H. Bacteria under stress by complement and coagulation. *FEMS Microbiol. Rev.* **38**, 1146–1171 (2014).
175. Doktycz, M., Sullivan, C. J., Hoyt, P. R., Pelletier, D. A., Wu, S. & Allison, D. P. AFM imaging of bacteria in liquid media immobilized on gelatin coated mica surfaces. *Ultramicroscopy* **97**, 209–216 (2003).
176. Storek, K. M., Auerbach, M. R., Shi, H., Garcia, N. K., Sun, D., Nickerson, N. N., Vij, R., Lin, Z., Chiang, N., Schneider, K., Wecksler, A. T., Skippington, E., Nakamura, G., Seshasayee, D., Koerber, J. T., Payandeh, J., Smith, P. A. & Rutherford, S. T. Monoclonal antibody targeting the  $\beta$ -barrel assembly machine of *Escherichia coli* is bactericidal. *Proc. Natl. Acad. Sci. U. S. A.* **115**,

3692–3697 (2018).